Doctoral Dissertation
Doctoral Program in Energy Engineering (32.nd cycle)

# Development of a Comprehensive 0-1D Powertrain and Vehicle Model for the Analysis of an Innovative 48 V Mild-Hybrid Diesel Passenger Car

**Alessandro Zanelli**
* * * * * *

**Supervisor**
Prof. Federico Millo

**Doctoral Examination Committee:**
Prof. Lucio Postrioti, Referee, Università degli Studi di Perugia
Prof. Giorgio Rizzoni, Referee, Ohio State University
Prof. Nicola Cavina, Università di Bologna
Prof. Agostino Gambarotta, Università degli Studi di Parma

Politecnico di Torino
July 13, 2020

This thesis is licensed under a Creative Commons License, Attribution - Noncommercial-NoDerivative Works 4.0 International: see www.creativecommons.org. The text may be reproduced for non-commercial purposes, provided that credit is given to the original author.

I hereby declare that, the contents and organisation of this dissertation constitute my own original work and does not compromise in any way the rights of third parties, including those relating to the security of personal data.

. . . . . .

Alessandro Zanelli
Turin, July 13, 2020

# Summary

The demanding $CO_2$ targets are pushing the development of cost effective solutions for the improvement of the efficiency of the powertrains. The electrification of the powertrain increases the complexity of the vehicle and the calibration effort that is required for the optimization of vehicle performance as fuel consumption and pollutant emissions. To manage this complexity, numerical simulation can play a fundamental role in evaluating innovative technologies, seeking the trade-off among conflicting objectives, scaling the number of tests at a minimal cost with respect to the experimental activity.

The aim of this work is to develop a methodology that integrates the detailed modelling of each powertrain subsystem in a high level framework, that is a comprehensive powertrain and vehicle model of a 48 V Mild Hybrid Vehicle. This comprehensive vehicle model, bringing together a 1D-CFD fast running model engine, a 1D-CFD aftertreatment model, a 1D-CFD cooling circuit model, a 0D electric motor and battery model as well as a virtual electronic control unit, aims to be a virtual test rig for the investigation of the impact of the electrification in terms of vehicle transient performance, fuel consumption and tailpipe pollutant emissions.

More in detail, in Ch.2, the case study is presented: a EURO 6 passenger car equipped with a 1.6 L 4-cylinder diesel engine is chosen for the analysis. The electrification is provided by the adoption of a 48 V Belt Starter Generator (BSG) and a Li-Ion battery pack. A 48 V electric catalyst placed upstream the Diesel Oxidation Catalyst and a 48 V electric supercharger downstream the main turbocharger, integrate the equipment of the investigated Mild Hybrid Vehicle.

In Ch.3 the development and the validation of the comprehensive vehicle model is presented. Using a commercially available software, GT-SUITE, a predictive combustion model was calibrated and validated on different combustion modes to test the model accuracy with different injection strategies. A Fast Running Model (FRM) engine was validated in steady state and transient time to boost operations showing a satisfactory agreement with the experimental data coming from General Motors - Global Propulsion System (GM-GPS). The comprehensive vehicle model, featuring the FRM engine with predictive combustion, the cooling circuit and the aftertreatment system, when driven along a WLTC driving cycle, performed closely to the vehicle tested on the roller bench in terms of fuel consumption, engine-out and tailpipe emissions. After the introduction of the 48 V electric system, the impact of electrification on the engine thermal state and

on the 48 V battery state of charge was compared with the experimental data showing a noteworthy correspondence of the results.

Using the comprehensive powertrain and vehicle model as virtual test rig, in Ch.4, the calibration of the Energy Management Strategy that showed a reduction, on the Worldwide harmonized Light vehicles Test Cycles (WLTC), by 6.1 % of carbon dioxide emissions, by 16.1 % of engine out nitrogen oxides emissions and tailpipe nitrogen oxides emissions below the conventional vehicle by 12.5 %, was chosen. The analysis of the introduction of an electric catalyst demonstrated the advantages of this technologies in terms of tailpipe nitrogen oxides emissions reduction (up to −54 %), with lower fuel consumption on the WLTC with respect to the conventional vehicle (−0.6 %) and similar results were obtained in other type approval and real driving emissions driving cycles. Moreover, the 48 V hybridization with BSG and the adoption of the electric supercharger, showed that the electrification remarkably reduces the elasticity time of the vehicle on different elasticity test in fixed gear (an improvement by more than 63 % was obtained on the 60 to 80 km/h).

Finally, in order to take advantage of the detailed modelling of the powertrain, a virtual calibration methodology, with the aim to investigate in depth the effects of innovative technologies on engine combustion and on vehicle fuel consumption and nitrogen oxides emissions, is proposed. The control parameters of the engine featuring, separately, Injection Rate Shaping, a theoretical injector with no hydraulic delay, the electric supercharger as auxiliary boosting system and Variable Valve Actuation were optimized on several Key Points. After the update of the calibration maps, driving cycle simulations of the innovative powertrains were performed showing benefits in fuel consumption (up to −0.9 %) and nitrogen oxides tailpipe emissions (up to −10.1 %).

# Acknowledgements

I would like to acknowledge General Motors – Global Propulsion Systems for sponsoring my PhD scholarship. I would also like to convey my gratitude to Dr. Rocco Fuso and Mr. Paolo Ferreri for their precious and constant support as well as for their invaluable suggestions during the simulation activities.

# Contents

**List of Tables** IX

**List of Figures** XI

**1 Introduction** 1

**2 Case Study** 5
2.1 Vehicle . . . 5
2.2 Powertrain . . . 6
2.2.1 Engine . . . 6
2.2.2 Coolant circuit . . . 7
2.2.3 Aftertreatment system . . . 8
2.2.4 12 V Electric Network . . . 8
2.2.5 48 V Electric Network . . . 8
2.3 Driving cycles . . . 10

**3 Methodology** 13
3.1 Predictive combustion . . . 13
3.2 Fast Running Model (FRM) Engine . . . 29
3.2.1 FRM Engine Control Unit . . . 30
3.2.2 FRM Engine Steady-state Validation . . . 31
3.2.3 FRM Engine Time To Boost Validation . . . 35
3.3 Vehicle . . . 36
3.3.1 Coolant circuit model . . . 39
3.3.2 Aftertreatment system model . . . 40
3.3.3 In-vehicle engine integration . . . 42
3.3.4 Conventional vehicle validation . . . 44
3.3.5 48 V vehicle validation . . . 50

**4 Results** 57
4.1 Energy and Emission Management Strategy (EEMS) . . . 58
4.2 Electrically Heated Catalyst (EHC) . . . 60

4.2.1 EHC Rule Based Controller . . . . . 62
4.3 48 V Mild Hybrid Vehicle results . . . . . 62
4.3.1 EEMS Calibration summary . . . . . 68
4.3.2 Phlegmatization . . . . . 73
4.3.3 Additional results on type approval and RDE driving cycles . . 74
4.4 Electric Supercharger (eSC) . . . . . 77
4.4.1 eSC Rule Based Controller . . . . . 78
4.4.2 Engine full load . . . . . 79
4.4.3 Transient results . . . . . 80
4.4.4 Driving cycle results . . . . . 86
4.5 Virtual Calibration . . . . . 88
4.5.1 Key Points Selection . . . . . 89
4.5.2 Optimization . . . . . 90
4.5.3 Updated calibration maps . . . . . 92
4.5.4 Driving cycle results . . . . . 93

**5 Conclusions** **97**

**A Additional Data** **101**

**Nomenclature** **121**

**Bibliography** **126**

# List of Tables


2.1 Vehicle Road Loads for Type-Approval and RDE driving cycles . . . . . 6
2.2 Manual Transmission (MT) gear ratios . . . . . 6
2.3 Engine Specifications . . . . . 7
2.4 BSG specifications . . . . . 9
2.5 Cell and battery pack specifications . . . . . 9
2.6 eSC specifications . . . . . 10
2.7 EHC specifications . . . . . 10
2.8 Driving cycle data . . . . . 11
3.1 Linear regression of experimental and simulated CPOA results for some notable engine parameters for the three combustion modes; R2 below 0.75 is highlighted in red . . . . . 26
3.2 Linear regression of experimental and simulated engine FRM results for some notable engine parameters for the three combustion modes - H hot, C cold condition; R2 below 0.75 is highlighted in red . . . . . 35
3.3 Summary of the end of driving cycle carbon dioxide, engine-out and tailpipe nitrogen oxides emissions of the simulated results with respect to the experimental data - Test A . . . . . 50
4.1 Summary of the end of driving cycle carbon dioxide, engine-out and tailpipe nitrogen oxides emissions with respect to the experimental data when the Extended Start & Stop is individually evaluated . . . . . 58
4.2 Impact of hybridization and introduction of an Electrically Heated Catalyst on the WLTC driving cycle . . . . . 73
4.3 Comparison among different driving cycles of the emissions of the conventional vehicle . . . . . 76
4.4 Comparison among different driving cycles of the specific BSG energy usage of the Mild Hybrid Vehicle . . . . . 77
4.5 Impact of hybridization and introduction of an Electrically Heated Catalyst on the RTS-95 driving cycle . . . . . 77
4.6 Impact of hybridization and introduction of an Electrically Heated Catalyst on the FTP-75 driving cycle . . . . . 78
4.7 Impact of hybridization and introduction of an Electrically Heated Catalyst on the US06 driving cycle . . . . . 78

4.8 Engine limitations . . . 80
4.9 Transient manoeuvers time summary. OT: overtorque . . . 85
4.10 BSG Mechanical Energy along the transient manoeuvers . . . 86
4.11 eSC Electric Energy along the transient manouevers . . . 86
4.12 Carbon dioxide, engine-out and tailpipe nitrogen oxides emissions along type approval and RDE driving cycles with and without the eSC (normalized on the basis of the conventional vehicle) . . . 87
4.13 Specific energy of hybrid functionalities and eSC specific electric energy along type approval and RDE driving cycles . . . 88
4.14 Energy breakdown of the electric energy utilization of the eSC along type approval and RDE driving cycles . . . 88
4.15 Test matrix and technologies investigated . . . 91
4.16 Virtual calibration: emission results . . . 95
4.17 Virtual calibration: emission results with eSC . . . 95
4.18 Specific energy of hybrid functionalities and eSC specific electric energy along the WLTC . . . 96
A.1 First five key points along the WLTC driving cycle splitted by combustion mode and ordered in terms of energy impact in each combustion mode . . . 107
A.2 Virtual calibration key points: ordered on the basis of the relative energy weight (first 17 points) and frequency (last 2 points) . . . 119

# List of Figures


2.1 Engine BSFC for each Combustion Mode . . . 7
2.2 Engine BSNOx for each Combustion Modes . . . 8
2.3 Driving cycles . . . 11
3.1 Injection rate estimation . . . 16
3.2 DIPULSE calibration points (red star) and validation points (circle) - Normal Mode calibration . . . 17
3.3 Measured and predicted Burn Rate at 1250 rpm and 50 Nm . . . 19
3.4 Measured and predicted Burn Rate at 2250 rpm and 127 Nm . . . 20
3.5 Measured and predicted Burn Rate at 2500 rpm and 50 Nm . . . 21
3.6 Measured and predicted Burn Rate at 3000 rpm and 200 Nm . . . 22
3.7 Experimental and Simulated MFB50% . . . 23
3.8 Experimental and Simulated maximum cylinder pressure . . . 24
3.9 Experimental and Simulated maximum cylinder temperature . . . 25
3.10 Experimental and Simulated NOx emissions . . . 27
3.11 Experimental and Simulated CO emissions . . . 28
3.12 Experimental and Simulated BSFC . . . 32
3.13 Experimental and Simulated BSNOx . . . 33
3.14 BSFC numerical experimental percentage difference across the engine map . . . 34
3.15 BSNOx numerical experimental percentage difference across the engine map . . . 34
3.16 TTB at 1500 rpm in Normal combustion mode - Engine parameters . . . 37
3.17 TTB at different engine speeds in Normal combustion mode - Brake Torque . . . 38
3.18 $NH_3$ storage capacity on the SCRF . . . 41
3.19 Impact of CO reactions . . . 43
3.20 12 V Vehicle results - Test A - Fragment of WLTC . . . 46
3.21 12 V Vehicle results - Test A . . . 47
3.22 12 V Vehicle cumulated emissions - Test A . . . 49
3.23 48 V Vehicle validation - Test B . . . 53
3.24 48 V Vehicle validation - Test C . . . 54
4.1 48 V Vehicle EMS comparision . . . 61

4.2 MHV with and without EHC along the WLTC driving cycle - EEMS calibrated for minimum $CO_2$ emissions . . . 65
4.3 MHV with and without EHC along the WLTC driving cycle - EEMS calibrated for minimum $CO_2$ emissions - Focus on light-off . . . 66
4.4 MHV with and without EHC along the WLTC driving cycle - EEMS calibrated for minimum $CO_2$ emissions - Emissions . . . 67
4.5 MHV with and without EHC along the WLTC driving cycle - EEMS calibrated for minimum NOx emissions . . . 69
4.6 MHV with and without EHC along the WLTC driving cycle - EEMS calibrated for minimum NOx emissions - Focus on light-off . . . 70
4.7 MHV with and without EHC along the WLTC driving cycle - EEMS calibrated for minimum NOx emissions - Emissions . . . 71
4.8 48 V Mild Hybrid Vehicle EEMS calibration . . . 74
4.9 Phlegmatization effect of the EEMS on a snippet of the WLTC . . . 75
4.10 Engine full load curve: base and with eSC . . . 81
4.11 Elasticity manoeuver 80-120 km/h in V gear . . . 83
4.12 Elasticity manoeuver 60-80 km/h in VI gear: impact of the engine with Overtorque feature . . . 84
4.13 Virtual calibration key points (red star) and reference calibration map points (circle) . . . 90
4.14 Virtual calibration: Pareto front BSFC - Noise for Case A, B, C and D at 1500 rpm and 179 Nm . . . 92
4.15 Map Interpolation . . . 93
4.16 Virtual calibration: comparison of calibration maps . . . 94
A.1 Brake Torque, Air Mass Flow Rate and Manifold Volumetric Efficiency - Normal Mode . . . 102
A.2 Experimental and Simulated BSFC . . . 103
A.3 Experimental and Simulated BSNOx . . . 104
A.4 Time to boost at 1500 rpm in Normal combustion mode - Engine parameters . . . 105
A.5 Time to boost at different engine speeds in Normal combustion mode - Torque . . . 106
A.6 Powetrain and vehicle integration: physical quantities and information flow . . . 108
A.7 Experimental speed compliance . . . 109
A.8 BSFC numerical experimental percentage difference with WLTC key-points for each combustion mode (green star) . . . 110
A.9 BSNOx numerical experimental percentage difference with WLTC key-points for each combustion mode (green star) . . . 111
A.10 eSC Rule Based Controller . . . 112
A.11 Elasticity manoeuver 80-120 km/h in V gear - Vehicle speed and acceleration, eSC speed . . . 113

A.12 Elasticity manoeuver 80-120 km/h in VI gear - Engine Brake Torque and Boost Pressure, BSG Mechanical Power . . . . . 114
A.13 Elasticity manoeuver 80-120 km/h in VI gear - Vehicle speed and acceleration, eSC speed . . . . . 115
A.14 Elasticity manoeuver 60-80 km/h in VI gear - Engine Brake Torque and Boost Pressure, BSG Mechanical Power . . . . . 116
A.15 Elasticity manoeuver 60-80 km/h in VI gear - Vehicle speed and acceleration, eSC speed . . . . . 117
A.16 Injection Rate, Burn Rate and In-Cylinder Pressure - Operating point: 1500 rpm 179 Nm . . . . . 120

# Chapter 1

# Introduction

The Dieselgate, which bursted in 2015 with the Violation Notice of the US Environment Protection Agency to Volkswagen about light duty vehicles equipped with "defeat devices in the form of computer software designed to cheat on federal emissions tests [...] the major excess pollutant at issue in this case is nitrogen oxides (NOx), and is a serious health concern." [1], overwhelmed the public opinion. The Audi A3 TDI Clean Diesel elected as Green Car of The Year in 2010 [2] (rescinded after the scandal) and the Superbowl ad about the green diesel [3] were promptly archived. A new wave of distrust of the diesel engine [4], severely endangered the research and development of future diesel powertrains [5–7]. Against the mismatch between homologation procedure and real world operation, the European Union, where diesel engines have been benefiting of favourable emission limits with respect to gasoline engines, responded with the approval of the Worldwide Light-Duty Harmonized Procedure (WLTP) [8]. This new homologation procedure adopted a driving cycle more representative of vehicle speeds and acceleration with respect to the old-fashioned New European Driving Cycle (NEDC). In addition to that, Real Driving Emissions (RDE) tests, where the vehicle is driven in real traffic, climate and altitude conditions, were proposed and proclaimed.

Five years later from the Violation Notice, car manufacturers and suppliers have dealt with this shock introducing technologies to effectively reduce pollutant emissions in any condition. The new V8 TDI engine of Volkswagen, the same manufacturer which received allegation for the defeat devices, tested by Emissions Analytics, is characterised by extremely low nitrogen oxides emissions, far below the Euro 6 limit (−75 % and evaluated in RDE conditions) [9]. An Italian car magazine, which compared diesel and gasoline engines in urban driving conditions, claims that diesel engines emits now comparably or less nitrogen oxides and particulate matter than gasoline engines [10], even before the introduction of a possible fuel-neutral EURO 7 legislation which is expected to be issued in the following years [11, 12].

Nevertheless, the dirty reputation of the diesel engine and the claims from the European capitals mayors to ban diesel engines [13, 14], reduced the diesel powered passenger car sales share from 51.5 % in 2015 to 35.9 % in 2018 to the advantage of an increase of

gasoline powered passenger cars [15]. On the other hand, after years of carbon dioxide emissions reduction, in 2017 and 2018 the average $CO_2$ emissions from new passenger cars in the EU increased by, respectively, 0.3 % and 1.8 % correlating with the increase of gasoline vehicle share.

This trend conflicts with the EU targets, recently set by European Parliament and the Council which adopted EU Regulation 2019/631 [16]. This regulation prescribes to reduce by 15 % the carbon dioxide emissions in 2025 over the 2021 baseline, according to the WLTP procedure, and by 37.5 % in 2030. For this reason, the higher efficiency of diesel engine is expected to contribute substantially in reaching this demanding targets: a share of diesel engine of about 40 % is expected by 2030 [17]. In the same year, about the 90 % of powertrains will be electrified, since the hybridization will be the key in reducing the carbon footprint of vehicles and allow the passenger cars to achieve the EU carbon dioxide targets.

In this framework, 48 V electrification of diesel powertrains represents the most cost effective solution to reduce the carbon footprint of passenger cars. Improvements up to 20 % can be expected from the introduction of 48 V Mild Hybrid systems which can leverage the functionalities of a full hybrid vehicle (e.g. recuperation and torque assist capabilities) [18] at a lower cost [19, 20]. For this reason, Mild Hybrid Vehicles are expected to achieve the 20 % of global car sales in 2020 [21]. The positive outlook of this technology is also promoted by technological development such as the concept, conceived by the manufacturer A123 [22], of a battery pack with a power approaching 25 kW to extend the electric power available and improve the system benefits.

The higher level of electric power achievable thanks to the 48 V hybridization with respect to the conventional 12 V network, enables the deep integration of electric auxiliary devices in the powertrain. Hence, functions which were historically distinctive features of the engine can be shared to electric and specialized devices with benefits in terms of engine performance and efficiency. For example, catalyst light-off has always been a critical operating point for the trade-off between engine efficiency and pollutant emissions. The engine is in this phase operated at its lowest efficiency to route the fuel power towards the exhaust line and to heat the catalyst. A specialized electric catalyst, made by an electric resistance and placed upstream of the Diesel Oxidation Catalyst and the Selective Catalytic Reduction system, can contribute to achieve lower emission targets shortening the light-off time. This system can be a key technology for future EURO 7 emissions targets [23]. Additionally, the quest for vehicle fun to drive gives rise to the introduction of boost-on-demand systems which can dramatically enhance the vehicle performance at a reduced or no detrimental effect on fuel consumption. Among these, electric superchargers have shown, for their advantages in terms of packaging and performance, to fit in an electrified powertrain. Indeed, exploiting the thermodynamic lever, small boosting power can be multiplied by the lower heating value of the fuel to increase dramatically the powertrain performance, positively affecting the vehicle drivability from low engine speeds [24, 25].

In this multifaceted context, where innovative technologies should be introduced

in a synergistic way to comply with emissions regulations and to continuously reduce the carbon footprint, numerical simulation can play a fundamental role. Vehicle and powertrain models are the medium where the complexity can be handled and different scenarios can be investigated. What is more, virtual tests are not (or very low) limited by test bench maintenance services, by failures, by physical time and space and they can be performed at minimal cost with respect to experimental tests. Simulation can be adopted at any stage of the V-cycle, the development process for the design and validation of complex systems.

However, several simulation methodologies can be adopted to represent powertrains and vehicle systems, ranging from 0D models to simulate different types of hybrid and full electric architectures, as proposed by Di Pierro et al. [26] to detailed subsystem modelling. On the one hand, powertrain map-based model, which are computationally efficient, are adopted for driving cycle simulation since they only require experimental maps of fuel consumption and engine-out pollutant emissions. They are usually employed to evaluate the benefit of the electrification on fuel consumption and engine-out emissions when the powertrain is fully warmed up, as done by Morra et al. [27], by Nüesch et al. [28] and by Lujan et al. [29], where fuel consumption and engine out nitrogen oxides emissions of a diesel hybrid architecture are assessed. Additionally, steady state maps can be corrected to properly evaluate the engine thermal state and the emissions from a cold start, as proposed by Gao et al. [30], but this requires estimates for both thermal and emissions parameters for each engine. Moreover, the use of map-based model neglects fluid-dynamics transients [31], with inaccuracies in the fuel consumption estimation especially on dynamic driving cycles (e.g. Real Driving Emissions cycles), which are introduced in the current legislation.

On the other hand, detailed models of components are adopted for the assessment of engine technologies, thermal management or tailpipe emissions analysis. Usually, 1D engine models are employed to properly assess combustion models and different calibration strategies along vehicle transient operations, as done by Dorsch et al. [32] or to evaluate the performance of different boosting systems (allowing to capture the turbolag effect). To this regard, in the work carried out by Griefnow et al. [33], a Fast Running Model (FRM) engine is used, in a vehicle simulation, with the aim to develop a Model Predictive Control for an electric supercharger. Concerning the thermal management, detailed engine and cooling circuit models are used to analyse cooling circuit hardware modifications as done by Caputo et al. [34] and Liu et al. [35]. Finally, high accuracy aftertreatment models are employed to evaluate tailpipe emissions using engine speed and torque traces according to a predefined mission scenario, engine-out traces for species concentrations, exhaust gas flow-rate and temperature generated beforehand by a vehicle model, as done for example by Karamitros et al. [36], where different aftertreatment systems for electrified powertrains are assessed.

So far, very little attention has been paid to a detailed modelling approach for the optimization of the entire powertrains. As a matter of fact, every vehicle subsystems has specific objectives which, due to the strong interactions among these functions,

may conflicts and lead to non-predictable overcompensations of component improvements at vehicle level. As an example, the optimization of the engine for lowest fuel consumption may lead to longer light-off time with unacceptable tailpipe emissions.

Therefore, this work aims to propose a comprehensive powertrain and vehicle modelling approach, for the evaluation of future electrified powertrains, embedding detailed engine, aftertreatment system, cooling circuit and Energy Management Strategy (EMS). This integrated model is developed to bridge the gap between high fidelity models commonly used for the development of components and coarser system level approaches for the evaluation of vehicle technologies and architectures. It is targeted to be predictive, since it is based on a phenomenological (e.g. the combustion model) or physical (e.g. the 1D-CFD engine model) foundation; deterministic, since no external disturbances are present in the simulation environment; flexible, because components and technologies can be swapped in a click. After the development of the virtual test rig in terms of combustion, engine performance and emissions along a driving cycle, the 48 V electrification on a Large Multi Purpose Vehicle featuring a 1.6 L engine will be investigated in terms of vehicle transient performance, fuel consumption, engine-out and tailpipe out nitrogen oxides emissions. An Energy and Emissions Management Strategy (EEMS) for the concurrent minimization of fuel consumption and tailpipe nitrogen oxides emissions will be presented and discussed. After the choice of the optimal EEMS calibration, the impact of different electric auxiliaries will be investigated: an electric catalyst and an electric supercharger. The impact of the electric catalyst on tailpipe nitrogen oxide emissions and fuel consumption will be analysed, while the electric supercharger will be assessed in terms of vehicle transient performance and fuel consumption along different driving cycles. Finally, a novel methodology for the virtual calibration of powertrains featuring breakthrough technologies will be proposed with the aim to assess, using the developed comprehensive powertrain and vehicle virtual test rig, vehicle fuel consumption and tailpipe emissions of any innovative powertrain concept from the idea to the (virtual) road.

# Chapter 2

# Case Study

In this chapter the case study considered for the development of this work is reported. The technical data presented here are provided by General Motors Global Propulsion System (GM-GPS) Torino, where not otherwise declared.

## 2.1 Vehicle

The vehicle is a Large Multi Purpose (LMPV) vehicle which main characteristics are shown in Tab.2.1.

Usually, vehicle resistance is described by a three term force versus speed relationship characteristic of tire rolling resistance, driveline losses and aerodynamic drag. The vehicle resistance equation may be expressed as $R = F0 + F1 \cdot V + F2 \cdot V^2$, where $F$ is the vehicle resistance in N, $V$ is the vehicle speed in km/h, $F0$ is the constant term in N, $F1$ is the linear term in Nh/km and $F2$ the quadratic term in $Nh^2/km^2$. Depending on the driving cycle, different vehicle mass and road load coefficients are used due to variation in the homologation regulation. According to WLTP regulation [37], the definition of a low and a high vehicle power requirement to properly define a vehicle family with the base vehicle (Test Mass Low - TML) or with the optional equipment and its impact on mass, rolling resistance and aerodynamic drag (Test Mass High - TMH), is required. In this work, the road load defined as WLTC TMH is representative of the vehicle tested on the roller bench, while RTS-95, FTP75 and US06 are provided by GM-GPS to be descriptive of the power request of the vehicle along different driving cycles. Moreover, the road load coefficient defined as WLTC TMH refers to the vehicle featuring the 48 V electrification, accounting for the additional mass coming from the 48 V battery and the 48 V BSG. Since the experimental data of the reference vehicle (representative of the vehicle with 12 V electric network) have been obtained turning the 48 V electric network off, in order to compare consistently simulation results and experimental data, the same road load coefficients will be used for the reference vehicle and the 48 V Mild Hybrid Vehicle (MHV). What is more, the weight increment due to 48 V electrification

is considered to be negligible: the 48 V battery has a weight below 10 kg, thanks to the passive cooling, and the 48 V Belt Starter Generator (BSG) substitutes, but is not added to, the 12 V alternator. The same consideration applies for the introduction of auxiliary components: the weight of Electrically Heated Catalyst (EHC) and of the electric Supercharger (eSC) (which is below 4 kg) are taken into account in the road load coefficient of the reference vehicle even if they are disabled. In Tab.2.1, the vehicle power resistance at wheel at a vehicle speed of 80 km/h and 100 km/h is reported.

Table 2.1: Vehicle Road Loads for Type-Approval and RDE driving cycles

| **Parameter** | **unit** | **WLTC TMH** | **RTS-95** | **FTP75** | **US06** |
|---|---|---|---|---|---|
| Mass | kg | 1945 | 1821 | 1821 | 1700 |
| F0 | N | 191.6 | 164.4 | 164.4 | 112.2 |
| F1 | Nh/km | 0.849 | 0.3893 | 0.3893 | -0.503 |
| F2 | $Nh^2/km^2$ | 0.03482 | 0.03825 | 0.03825 | 0.04207 |
| Rolling Radius | mm | 325 | 325 | 325 | 319 |
| P @80 km/h | kW | 10.72 | 9.79 | 9.79 | 7.58 |
| P @100 km/h | kW | 17.35 | 16.27 | 16.27 | 13.41 |

The vehicle features a Manual Transmission (MT) with 6 gears which gear ratios are reported in Tab.2.2. A Dual Mass Flywheel (DMF) is placed between engine and transmission to dampen the vibrations coming from the engine.

Table 2.2: Manual Transmission (MT) gear ratios

| Final Drive (FD) | 1st | 2nd | 3rd | 4th | 5th | 6th |
|---|---|---|---|---|---|---|
| 3.545 | 4.167 | 2.13 | 1.321 | 0.954 | 0.755 | 0.623 |

## 2.2 Powertrain

The powertrain is based on a EU6 diesel engine. Its main components are a state-of-the art diesel engine, a EU6 compliant aftertreatment system, a cooling circuit and the electric network. The electrification of the powertrain is achieved through 48 V electrification.

### 2.2.1 Engine

The engine main specifications are reported in Tab.2.3. It features a Common Rail diesel injection system, a Variable Geometry Turbine (VGT) turbocharger and a cooled high pressure Exhaust Gas Recirculation (EGR) system for the in-cylinder control of

the pollutant emissions. The Fuel Injection System (FIS) is provided by Denso with a maximum injection pressure of 2000 bar. Additionally, this engine features a swirl flap for the control of the in-cylinder turbulence.

Table 2.3: Engine Specifications

| | | |
|---|---|---|
| Bore | mm | 79.7 |
| Stroke | mm | 80.1 |
| Compression Ratio | - | 16 |
| Displacement | $cm^3$ | 1598 |
| Rated Power | kW | 100 |
| Speed @ Rated Power | rpm | 4000 |
| Rated Torque | Nm | 320 |
| Speed @ Rated Torque | rpm | 2000 |
| Idle speed | rpm | 800 |
| BSFC @ 2000 rpm x 2 bar BMEP | g/kWh | 307 |
| Fuel | - | B10 diesel |

The engine adopts different combustion modes depending on its thermal state. Indeed, the engine Electronic Control Unit (ECU) switches from a Warm-Up combustion mode designed for a fast aftertreatment light-off, when the engine is cold, to a Blended Mode, and finally to a Normal combustion mode when the engine is fully warmed up, for the highest combustion efficiency. The qualitative impact of the calibration on BSFC is shown in Fig.2.1, while on BSNOX is shown in Fig.2.2.

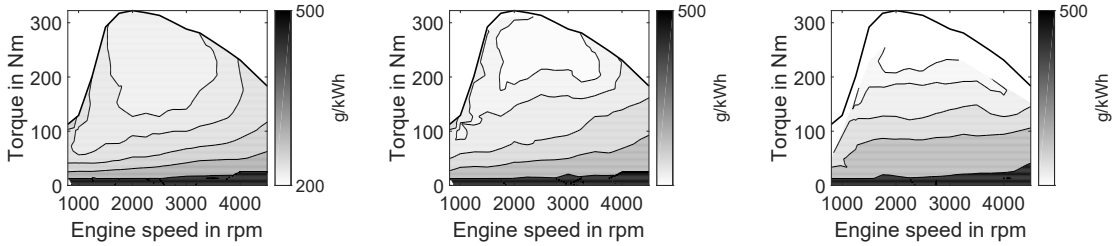


(a) Normal Mode (b) Blended Mode (c) Warm-up Mode

Figure 2.1: Engine BSFC for each Combustion Mode

## 2.2.2 Coolant circuit

The coolant circuit features an electronically controlled thermostat, a Switchable Water Pump (SWP) actuated by means of an electromagnetic clutch and a variable-speed radiator fan.

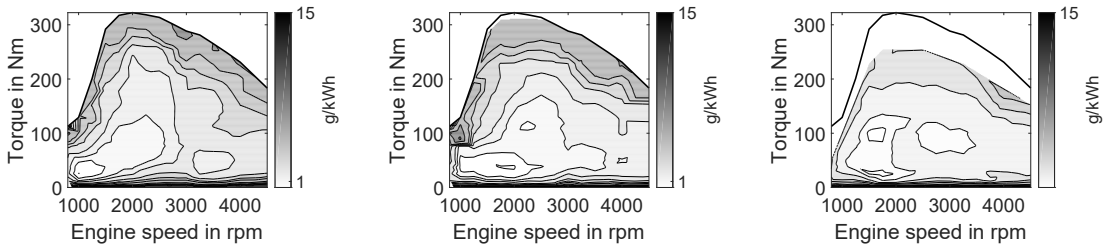


(a) Normal Mode (b) Blended Mode (c) Warm-up Mode

Figure 2.2: Engine BSNOx for each Combustion Modes

### 2.2.3 Aftertreatment system

The aftertreatment system includes a Diesel Oxidation Catalyst (DOC) for the oxidation of carbon monoxide (CO) and unburned hydrocarbons (HC), a Selective Catalytic Reduction (SCR) system for the reduction of the nitrogen oxides (NOx) which integrates a Diesel Particulate Filter (DPF) for the filtration and retention of the Particulate Matter (PM) produced by the engine. The DOC and SCR on filter are in close-coupled position. This aftertreatment system allows the vehicle to achieve the EU6 homologation requirements.

### 2.2.4 12 V Electric Network

The 12 V electric network, pertaining to the reference vehicle (i.e. with the conventional 12 V powertrain), is composed by a starter motor and a 12 V alternator. The starter motor has a peak power of 1.8 kW and a peak efficiency of 0.6. It is actuated by means of an electromagnetic clutch and the gear ratio between it and the engine is 13. The 12 V alternator guarantees a supply of 140 A to the electric network and it is geared to the engine with a gear ratio of 2.935.

### 2.2.5 48 V Electric Network

The 48 V electric network is the proper system of the 48 V Mild-Hybrid powertrain. This system differs to the 12 V electric network since a 48 V Belt Starter Generator (BSG) (or Motor Generator Unit, MGU) takes the place of the 12 V alternator (P0 layout).

**BSG** The 48 V BSG main specifications are reported in Tab.2.4. The BSG is liquid cooled to guarantee good performance during long transient operation.

**Li-ion Battery** The Li-Ion battery cells and the battery pack specifications are highlighted in Tab.2.5. The battery pack specifications have been shared by GM-GPS. However, the battery cells specification, used in the following modelling activity in terms of

Table 2.4: BSG specifications

| | | |
|---|---|---|
| Nominal Voltage | V | 48 |
| Rated Motor Torque | Nm | 58 |
| Rated Motor Power | kW | 13 |
| Rated Generator Torque | Nm | - 14 |
| Rated Generator Power | kW | - 7.8 |
| Rated Generator (Braking) Torque | Nm | - 58 |
| Rated Generator (Braking) Power | kW | - 22.6 |
| Peak Efficiency | - | 0.85 |

Open Circuit Voltage (OCV) and resistance, here reported at 50 % of the battery State Of Charge (SOC) comes from a previous experimental activity done at Politecnico di Torino.

Table 2.5: Cell and battery pack specifications

| **Battery Cell Specifications** | **unit** | **value** |
|---|---|---|
| Cell OCV @ 50 % SOC | V | 3.7 |
| Cell Resistance @ 50 % SOC | mΩ | 1.4 |
| **Battery Pack Specifications** | **unit** | **value** |
| Number of Series Cells | - | 13 |
| Number of Parallel Cells | - | 1 |
| Cell capacity | Ah | 10 |
| Nominal Voltage | V | 48 |
| Minimum Rated Voltage | V | 32.5 |
| Maximum Rated Voltage | V | 54 |
| Maximum Rated Current | A | 250 |
| Minimum Rated Current | A | - 250 |
| Battery weight | kg | < 10 |

**eSC** The electric SuperCharger (eSC) considered for this case study is powered by a 48 V electric motor and its main specifications are reported in Tab.2.6. The eSC is placed in series with the main turbocharger in downstream location.

**EHC** The Electrically Heated Catalyst (EHC) is powered by the 48 V electric network. It is placed before the main DOC and it is aimed to reduce the catalyst light-off time. The EHC main specifications are reported in Tab.2.7.

Table 2.6: eSC specifications

| electric Supercharger weight | kg | < 4 |
|---|---|---|
| **Compressor Specifications** | **unit** | **value** |
| Compressor Max Speed | rpm | 75000 |
| Compressor Max Pressure Ratio 1.5 | - | 1.5 |
| Compressor Max Corrected Mass Flow | kg/s | 0.10 |
| Compressor Peak Efficiency | - | 0.82 |
| **Electric Motor Specifications** | **unit** | **value** |
| Electric Motor Nominal Voltage | V | 48 |
| Electric Motor Max Torque | Nm | 0.6 |
| Electric Motor Max Power | kW | 5.3 |

Table 2.7: EHC specifications

| **EHC specifications** | **unit** | **value** |
|---|---|---|
| Nominal Voltage | V | 48 |
| Max Power | kW | 4 |

## 2.3 Driving cycles

In this section the test cycles are reported. Driving cycles may be divided in type-approval or RDE (Real Driving Emissions) cycles. On the one hand, type-approval driving cycles are imposed by the homologation regulation, for example the WLTC is prescribed by EU legislation. In the US, the FTP75 and the US06, among the others, are the reference cycle for vehicle emission certification. On the other hand, the recent adoption of RDE conformity for the emission certification resulted in the spread of several cycles. Among these, the Standardized Random Test For An Aggressive Driving Style (RTS-95) is worth of note since it is characteristic of an aggressive driving style. The speed profile of these driving cycles is depicted in Fig.2.3.

In Tab.2.8 the main data for the driving cycle of interest for this work are reported. The data are computed from [38].

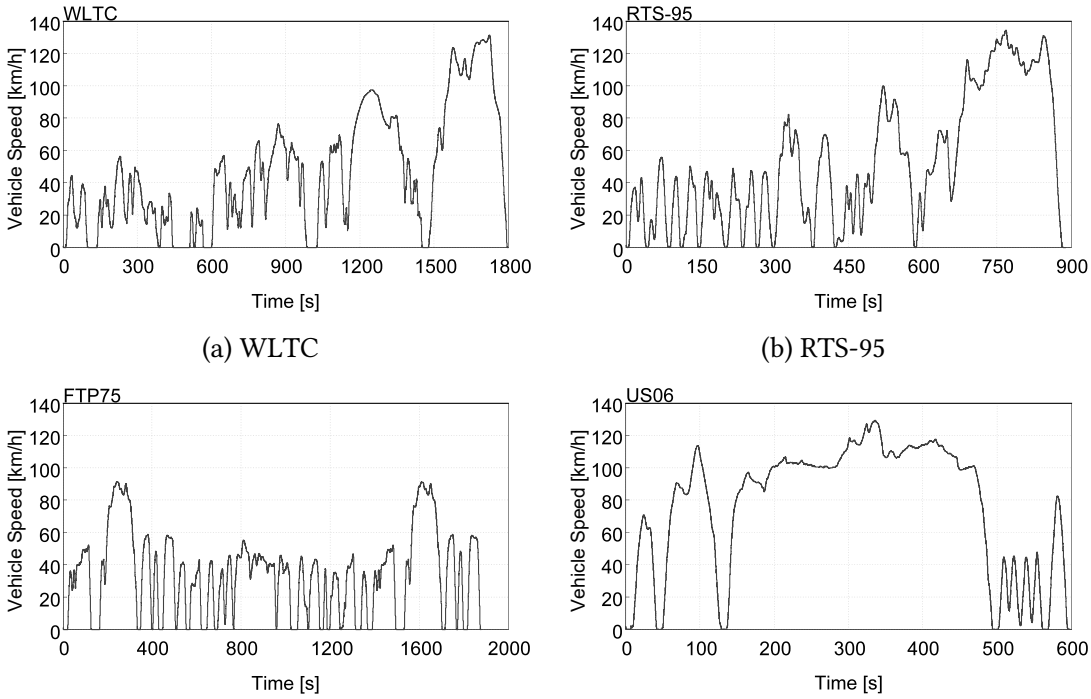


(a) WLTC

(b) RTS-95

(c) FTP75

(d) US06

Figure 2.3: Driving cycles

Table 2.8: Driving cycle data

| **Parameter** | **unit** | **WLTC** | **RTS-95** | **FTP-75** | **US06** |
|---|---|---|---|---|---|
| Duration | s | 1800 | 886 | 1877 | 596 |
| Distance | km | 23.27 | 12.93 | 17.77 | 12.8 |
| Mean Velocity | $km\,h^{-1}$ | 46.5 | 52.5 | 34.12 | 77.9 |
| Max Velocity | $km\,h^{-1}$ | 131.3 | 134.5 | 91.25 | 129.2 |
| Max Acceleration | $m\,s^{-2}$ | 1.67 | 3.21 | 1.48 | 3.76 |
| Min Acceleration | $m\,s^{-2}$ | -1.50 | -2.71 | -1.48 | -3.09 |
| Mean Pos. Acc. | $m\,s^{-2}$ | 0.41 | 0.76 | 0.51 | 0.67 |
| Mean Neg. Acc. | $m\,s^{-2}$ | -0.45 | -0.77 | -0.58 | -0.72 |

# Chapter 3

# Methodology

In this work, the engine and the main subsystems have been represented by 1D-CFD models. This approach guarantees that the flow and heat transfer in the piping and other flow components of the powertrain can be accurately traced and considered in the simulation. In a powertrain and vehicle study intended to assess the impact of the electrification on vehicle thermal management, aftertreatment conversion efficiency and engine and vehicle performance, this 1D-CFD modelling approach for the entire powertrain (i.e. engine, cooling circuit and aftertreatment system) is the preferred choice.

In this chapter, the methodology followed during the integration of the subsystems in the comprehensive vehicle model and its validation, using a commercially available software GT-SUITE, is reported. The development of this work begins with the validation of the predictive combustion with the aim to have a predictive burn rate for the efficiency and fuel consumption evaluation and for the estimation of the pollutant emissions (CO, HC and NOx). The predictive combustion model is able to reproduce the impact of engine parameters (i.e. the Exhaust Gas Recirculation, EGR) on the exhaust emissions. Afterwards, the validation of the 1D-CFD Fast Running Model (FRM) engine, to reproduce different calibration maps and quantify the difference between model and experimental data, is done. Finally, the comprehensive vehicle model is validated with respect to experimental data.

## 3.1 Predictive combustion

In this section the calibration of the predictive combustion model is presented. A predictive combustion model has several advantages over a non-predictive combustion model. Indeed, a non predictive combustion model

> simply imposes a burn rate as a function of crank angle. This prescribed burn rate will be followed regardless of the conditions in the cylinder, assuming that there is sufficient fuel available in the cylinder to support the

> burn rate. Therefore, the burn rate will not be affected by factors such as residual fraction or injection timing. [39]

On the contrary, the predictive combustion model used for this work is the DIPULSE developed by GT-SUITE. This model predicts the combustion rate and the emissions and was developed for direct-injection diesel engines with multiple injection events.

> The basic approach of this model is to track the fuel as it is injected, evaporates, mixes with surrounding gas, and burns. As such an accurate injection profile is absolutely required to achieve meaningful results. The DIPULSE model should be calibrated to match the combustion event as calculated from cylinder pressure analysis. [...] The cylinder contents are discretized into three thermodynamic zones, each with their own temperature and composition. The main unburned zone contains all cylinder mass at IVC, the spray unburned zone contains injected fuel and entrained gas, and the spray burned zone contains combustion products. The DIPULSE model also includes several submodels which simulate the relevant physical processes taking place during injection and combustion. [...] Fuel Injection – Each contiguous injection event is defined as an injection pulse and is tracked separately from all other pulses. Any number of pulses may be injected, and there is no inherent distinction made between pilot, main, or post injection pulses. The injected fuel is added to the spray unburned zone. Entrainment – As the spray penetrates, it slows down as the surrounding unburned and burned gases are entrained into the pulse. The intermixing of pulses occurs through entrainment. [...] Evaporation – Droplet evaporation is modeled with a coupled solution of heat and mass transfer which appropriately accounts for both diffusion-limited and boiling-limited evaporation. [...] Ignition – The mixture in each pulse undergoes an ignition delay modeled with an Arrhenius expression. [...] Premixed Combustion – When a pulse ignites, the mixture present at that time is set aside for premixed combustion. The rate of this combustion is assumed to be kinetically-limited [...] Diffusion Combustion – After a pulse ignites, the remaining unmixed fuel and entrained gas in the pulse continue to mix and burn in a primarily diffusion-limited phase. [39]

The calibration of a predictive combustion model requires the in-cylinder pressure data and injection data. For this work the three different calibration maps, which were already shown in Ch.2, are used as calibration maps for the engine operating parameters and experimental in-cylinder pressure data are available for each engine operating point.

The predictive combustion model is sensitive to the injection rate profiles and experimental test are needed to build up a library of injection profiles (hereafter referred to as Injection Rates Map). The procedure followed in this work for the creation of the

injection rate map follows the one already presented in [40]. The first data needed for the creation of the injection rate map are the data from EVI (Einspritzverlaufsindikator - injection rate indicator) and EMI (Einspritzmengenindikator - injection quantity indicator) analysis. The EVI curves available are done at different rail pressure and for different energizing time. They are used to have the proper injection rate profile that is function of injection pressure and Energizing Time (ET). On the other side, EMI curves are used to quantify the injection quantity that depends on injection time and injection pressure.

For this work EVI curves with two different set of ET and six different injection rail pressure (for a total of 12 injection rates) were available (up to the maximum injection pressure of 2000 bar).

The injection rate map was build up by means of interpolation and extrapolation assuming that [40]

- The hydraulic delay is constant (depends only on rail pressure).
- The rising slope of the mass flow rate is constant (depends only on rail pressure).
- Once the injector is at full lift (maximum mass flow rate), the mass flow rate is constant since the controlling part is the nozzle.
- The descent phase of the mass flow rate is constant (depends only on rail pressure).

In contrast with the first quote, for this injector the analysis of the experimental data showed that a constant hydraulic delay of 0.4 ms was representative of the injector behaviour regardless of the injection pressure.

In Fig.3.1 an example of the injection rate map creation at 400 bar and 2000 bar of injection pressure is shown. The injection rate map developed is composed by 8 levels of injection pressure and 17 level of ET to guarantee a smooth interpolation across the injector operating range. It is worth to underline that, the use of an injection rate map neglects the impact of pulse to pulse interaction, which may be considered negligible for the scope of this work. Moreover, in the FRM engine, transients in the rail pressure will be neglected and the rail pressure set-point, taken from the calibration maps as a function of engine speed and injected quantity, will be directly used to interpolate the injection rate profile on the injection rate map.

The methodology followed for the calibration and validation of the predictive combustion model begins with the choice of the calibration points. In order to acquire a predictive capability across the engine operating range, 29 points of the Normal Mode calibration representative of the whole engine operating conditions in terms of load, speed, EGR rate, injection pressure, and injection pattern were chosen. The validation of the combustion model was performed over 219 (excluding the 29 points for calibration) engine points of the Normal Mode calibration, over 248 points of the Blended

Mode calibration and over 182 points of the Warm-up Mode calibration. In Fig.3.2 the calibration and validation points of the Normal Mode calibration are shown.

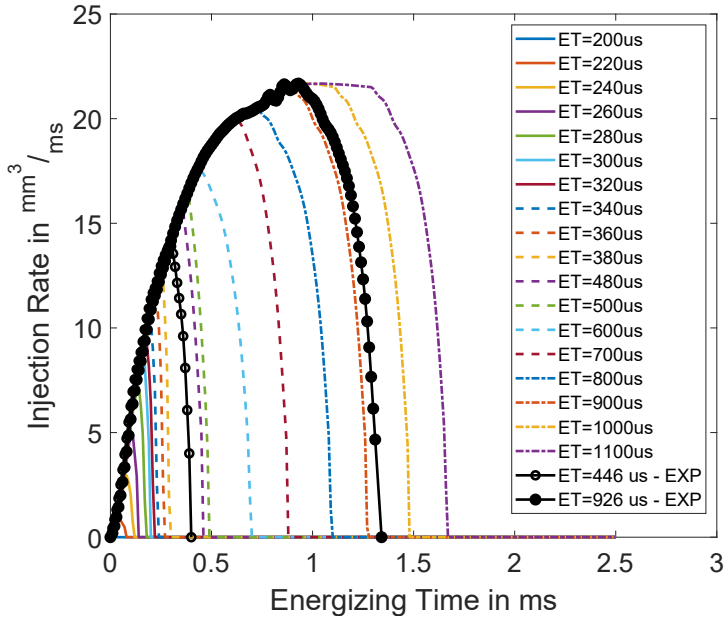


(a) Rail pressure: 400 bar

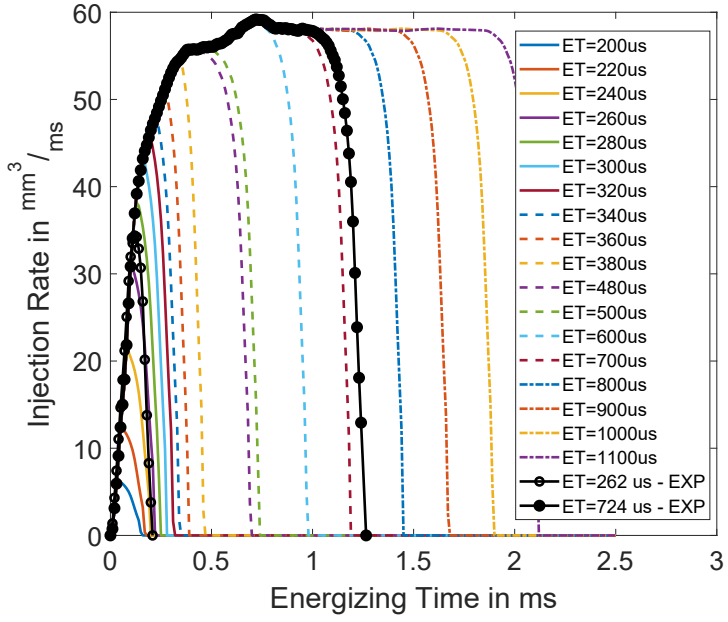


(b) Rail pressure: 2000 bar

Figure 3.1: Injection rate estimation

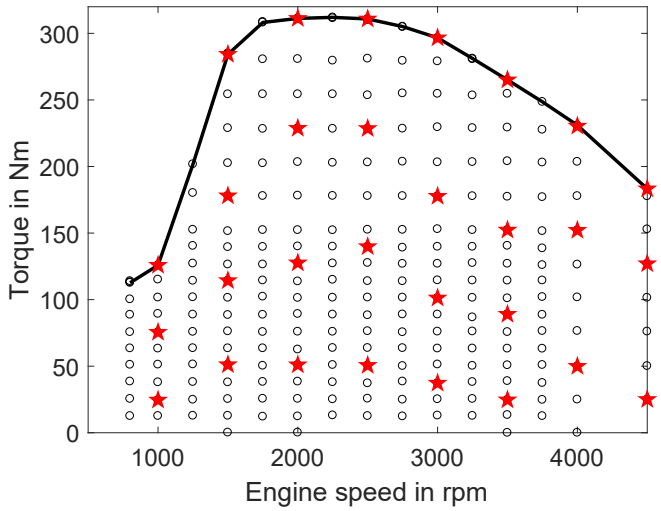


Figure 3.2: DIPULSE calibration points (red star) and validation points (circle) - Normal Mode calibration

A single cylinder model approach, the so called Cylinder Pressure Only Analysis (CPOA), which requires the measured pressure traces and the quantity of fuel, air and residual burned gas, was used for the burn rate analysis and for the calibration of the predictive combustion model. Since the DIPULSE is a phenomenological approach based on the stages of the diesel combustion process from the spray penetration to the diffusion combustion that includes some assumptions and simplifications, it requires some calibration of the relations describing the underlying phenomena. For this reason, to accurately describe each stage of the combustion process seven parameters can be tuned to reduce to a minimum the deviation between computed Burn rate from the pressure trace and the burn rate estimated by the combustion model (i.e. the Burn Rate Error - BRE). These parameters are Entrainment Rate multiplier, Ignition Delay multiplier, Premixed Combustion Rate multiplier and four parameters for the diffusive combustion: Diffusion Combustion Rate multiplier, Diffusion Multiplier Transition Timing, Diffusion Multiplier Final Value and Diffusion Multiplier Transition Rate [39]. As done in [40], a Genetic Algorithm (GA) optimization was performed, with a population size of 10 elements and a number of generations equal to 50, to find the value of the parameters which minimizes the BRE.

In Fig.3.3, 3.4, 3.5 and 3.6, the predicted and measured burn rate is shown for four different operating points, respectively 1250 rpm x 50 Nm, 2250 rpm x 127 Nm, 2500 rpm x 50 Nm (this is a calibration point for the Normal combustion mode) and 3000 rpm x 200 Nm. The agreement between predicted and measured burn rate is satisfactory. There are small deviation as far as the burn rate promoted by the pilot injection is concerned. The main rise in burn rate, following the main injection, is well reproduced as well

as the consequent combustion slow-down. However, the burn rate predicted from the introduction of a late injection after the main injection is, especially at low load (i.e. 50 Nm, equivalent to 4 bar of Brake Mean Effective Pressure - BMEP), not correctly phased with the measured burn rate. The predicted burn rate which is predicted from 30° after Top Dead Center firing (aTDCF) onward, is delayed and more impulsive with respect to the measured one.

In Fig.3.7, 3.8 and 3.9, the comparison between, respectively, experimental and simulated 50% of Mass Fraction Burned (MFB50%), maximum in-cylinder pressure and maximum temperature are shown. In Normal and Blended Mode the majority of engine operating points is in the range ±2 Crank Angle Degree. A good agreement is apparent also in the Warm-up combustion mode for operating points with a MFB50% below 30° aTDCF. Above this threshold, the model is not able to satisfactory predict the combustion phasing. As far as the maximum in-cylinder pressure is concerned, the agreement between simulation and experimental data is more than satisfactory for the three combustion modes, with the majority of the engine operating points placed in the range ±5 bar. Finally, the simulated in-cylinder temperatures match by a great extent the experimental in-cylinder temperatures with a deviation above 100 K at low (below 1000 K) and high (above 2000 K) temperature. The Warm-up combustion mode shows a more scattered behaviour across the y = x line (see Fig.3.9) due to a combustion phasing incorrect prediction. From a combustion point of view the DIPULSE is able to correctly predict combustion phasing, which is the key of the thermodynamic efficiency, to predict the maximum pressure which affects the engine friction and to predict the in-cylinder temperature which affects the NOx formation.

The predictive combustion model DIPULSE can be additionally used to estimate the production of the nitrogen oxides (NOx) on the basis of the extended Zeldovich mechanism [41] showing good prediction capabilities [40]. Ten parameters are provided by the DIPULSE model for the calibration of NO and $NO_2$ formation in order to take into account, among the other reactions, the oxidation of $N_2$ and the reduction of $NO_2$. On top of that a NOx calibration multiplier may be used to act on the net rate of NO and $NO_2$ production. For the calibration of the NOx parameters, a GA optimization, similarly as the optimization used for the burn rate calibration, has been pursued. In this case the error to be minimized was the difference between measured and computed NO and $NO_2$ concentrations. As far as other pollutant emissions are concerned, the software computes equilibrium products concentrations along the combustion process. The predictive combustion model allows to fine tune, besides the NOx emissions, also CO and soot emissions. The CO computed by the DIPULSE may be calibrated acting on two parameters. The first one, the so called Overmixing Rate Multiplier takes into account the amount of fuel that is "overmixed beyond the lean limit" [39] and does not take part into the combustion. The second one, the Partial Oxidation Rate Multiplier, controls the rate at which the unburned fuel is partially oxidised. In an analogous matter as for NOx formation, in this case a GA optimization with the aim to minimize the error between measured and computed CO concentration has been done. The calibration

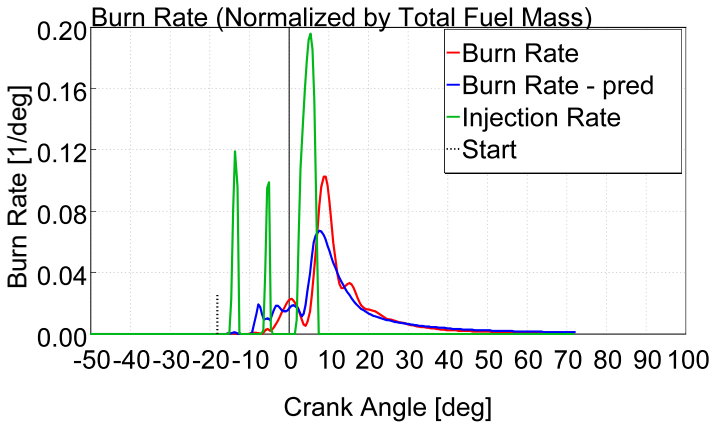


(a) Normal Mode

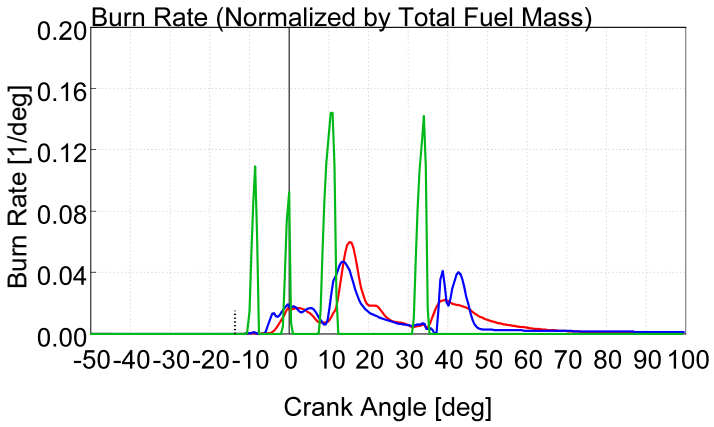


(b) Blended Mode

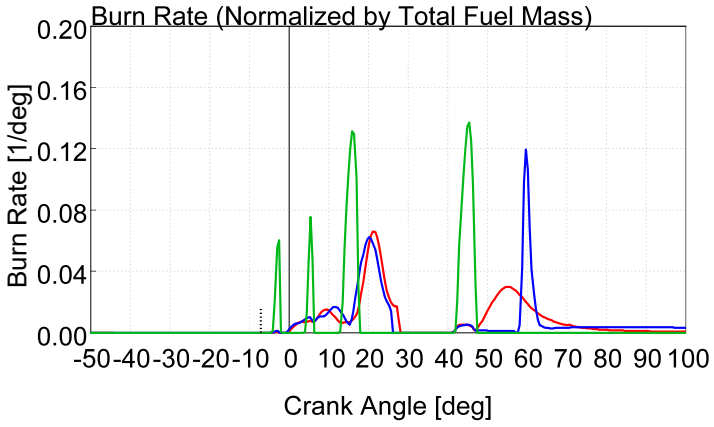


(c) Warm-up Mode

Figure 3.3: Measured and predicted Burn Rate at 1250 rpm and 50 Nm

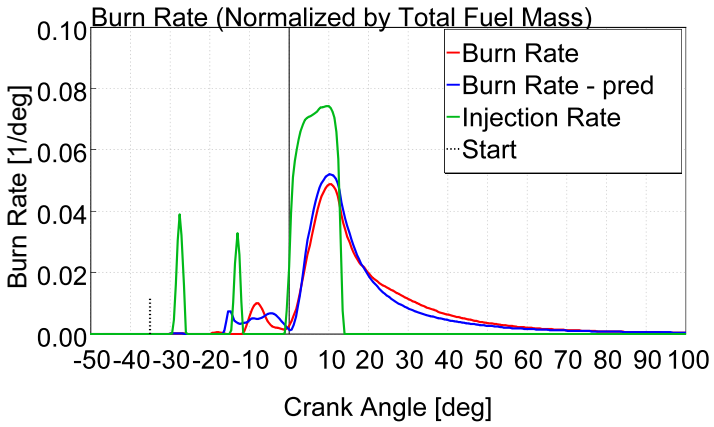


(a) Normal Mode

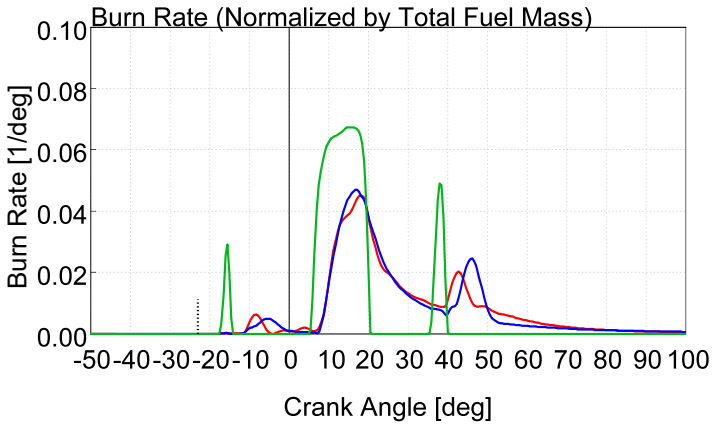


(b) Blended Mode

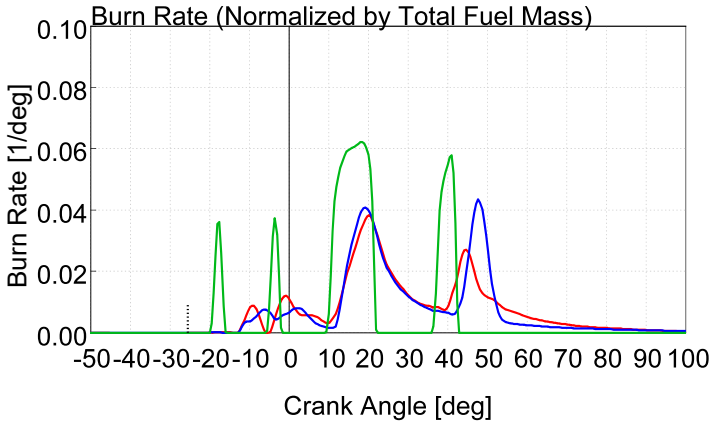


(c) Warm-up Mode

Figure 3.4: Measured and predicted Burn Rate at 2250 rpm and 127 Nm

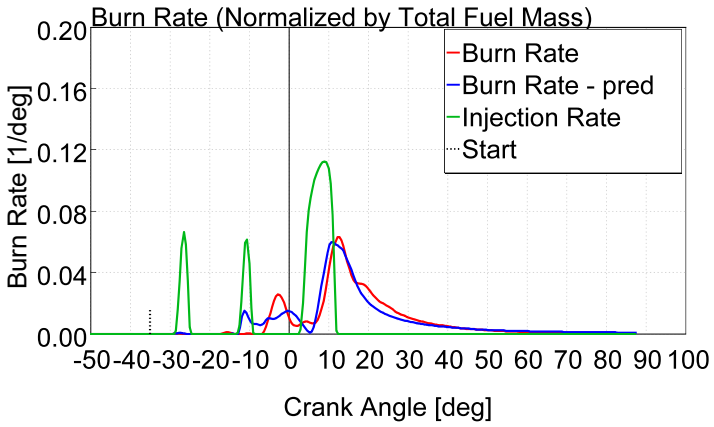


(a) Normal Mode

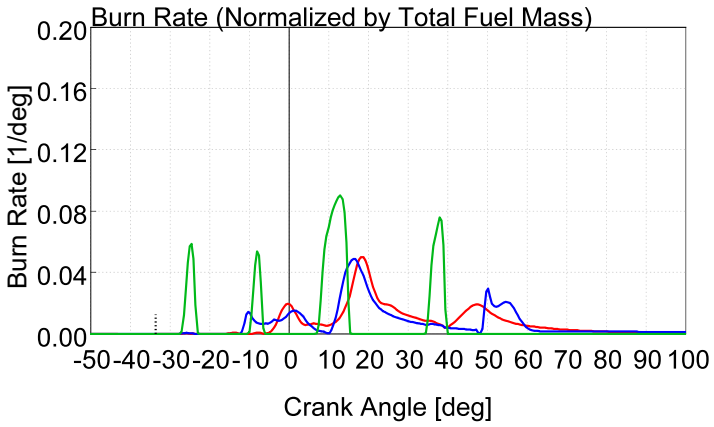


(b) Blended Mode

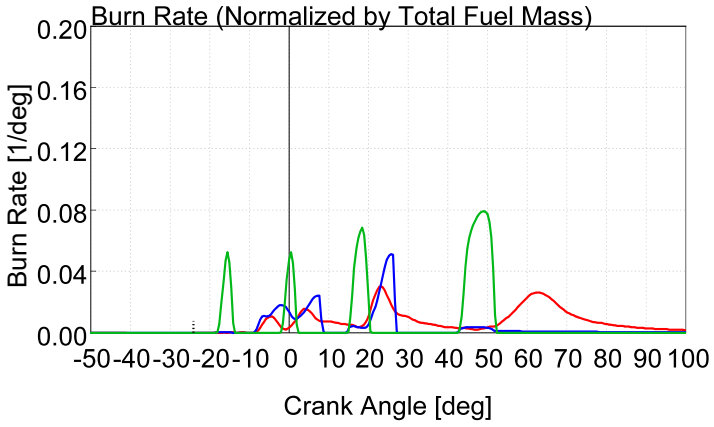


(c) Warm-up Mode

Figure 3.5: Measured and predicted Burn Rate at 2500 rpm and 50 Nm

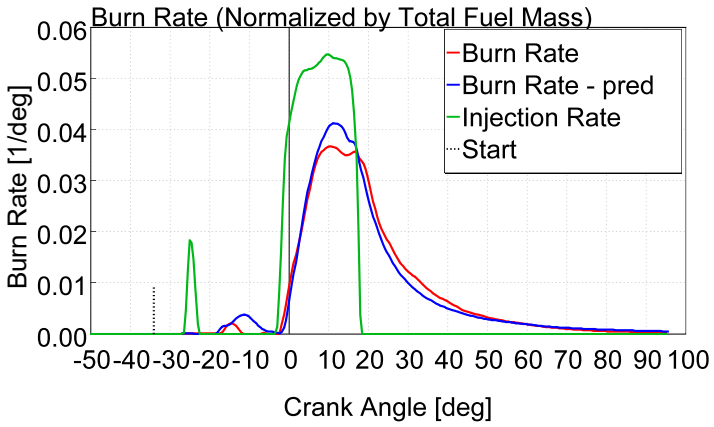


(a) Normal Mode

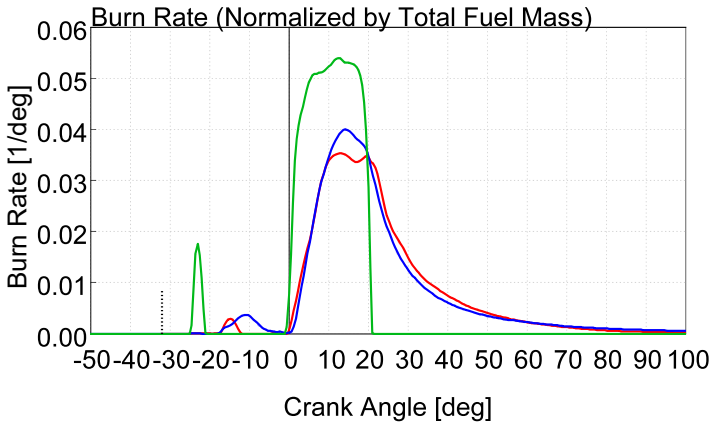


(b) Blended Mode

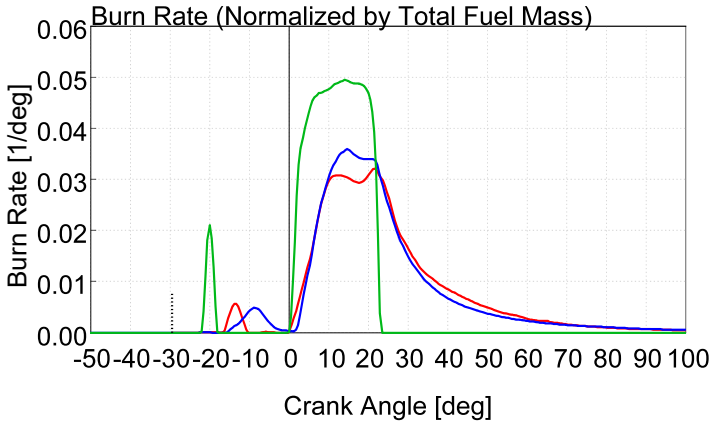


(c) Warm-up Mode

Figure 3.6: Measured and predicted Burn Rate at 3000 rpm and 200 Nm

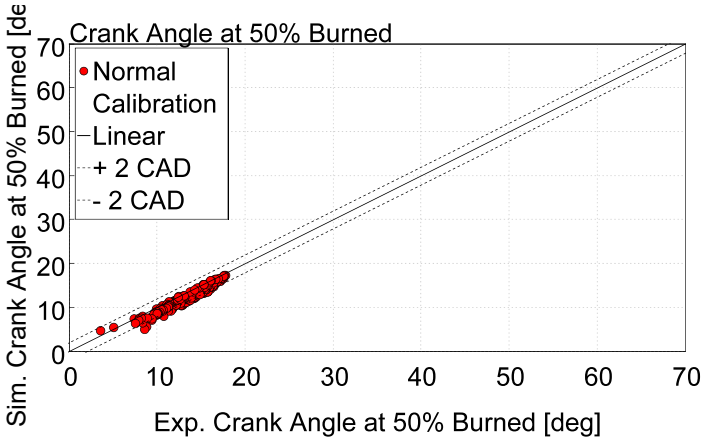


(a) Normal Mode

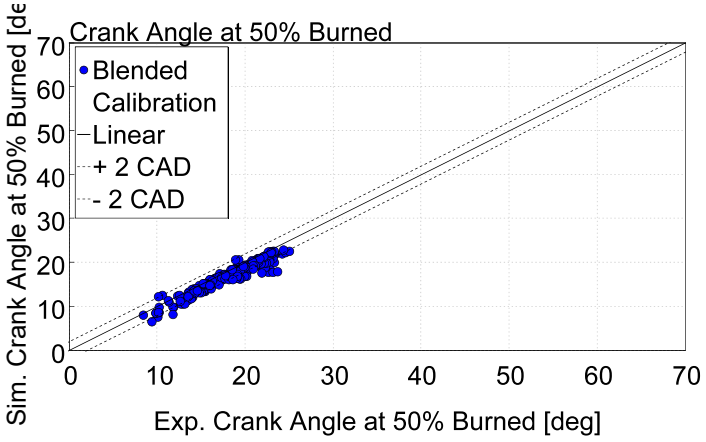


(b) Blended Mode

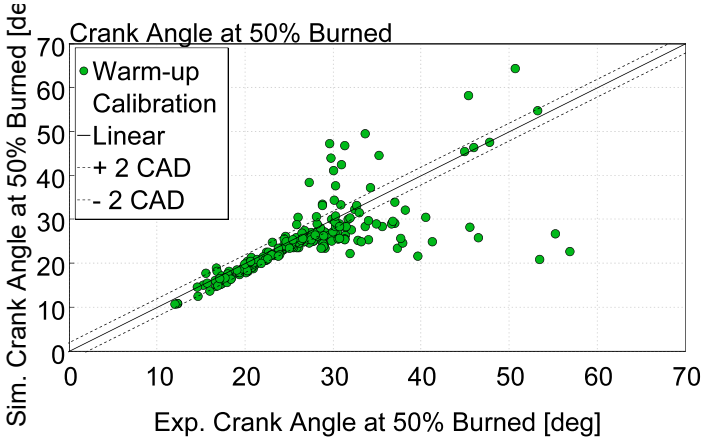


(c) Warm-up Mode

Figure 3.7: Experimental and Simulated MFB50%

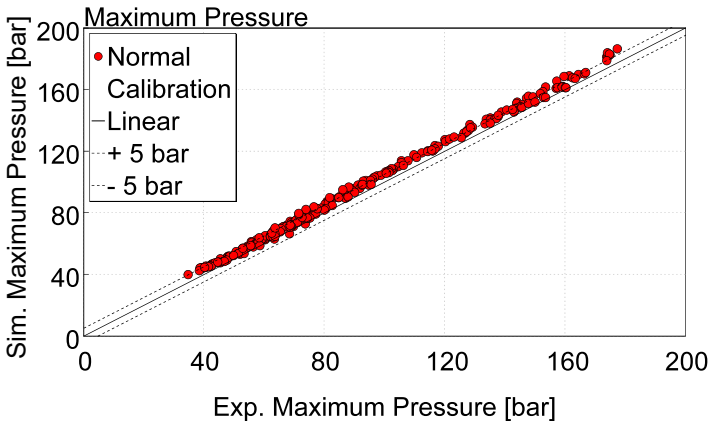


(a) Normal Mode

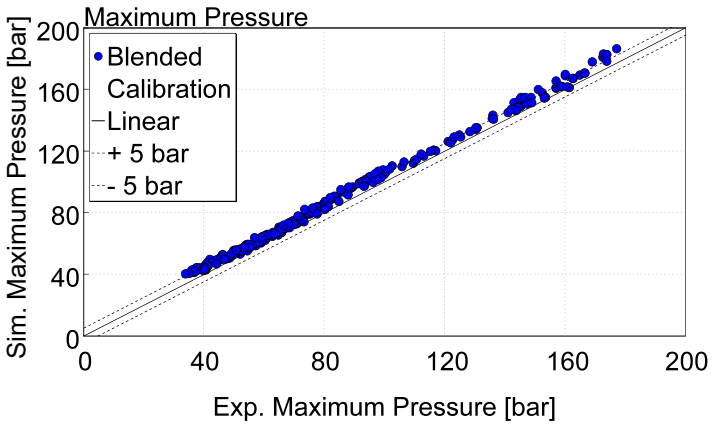


(b) Blended Mode

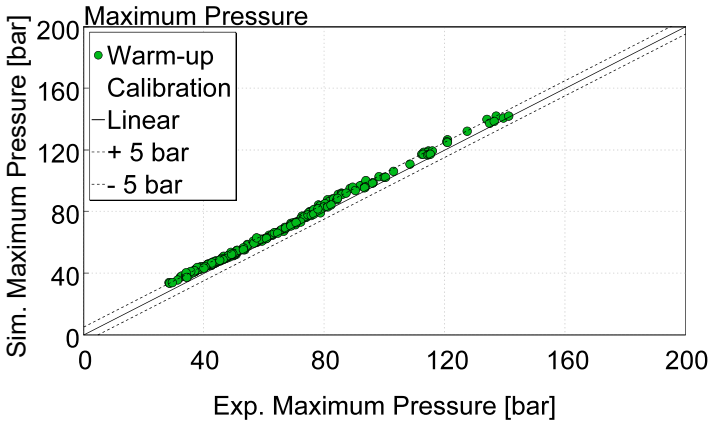


(c) Warm-up Mode

Figure 3.8: Experimental and Simulated maximum cylinder pressure

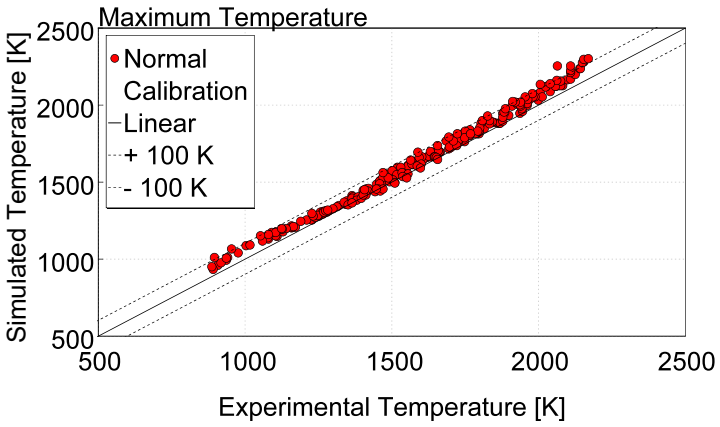


(a) Normal Mode

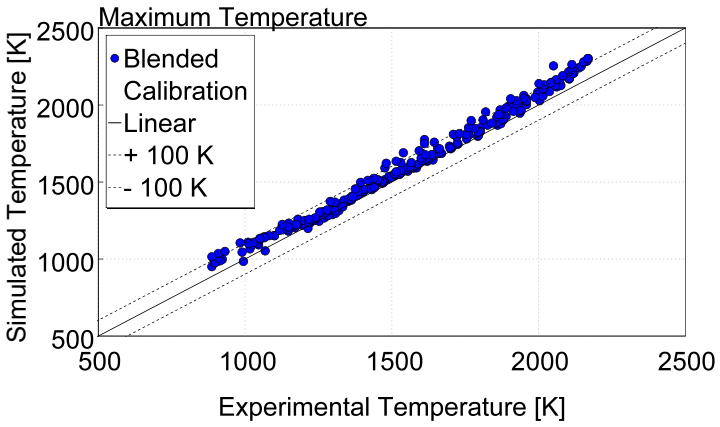


(b) Blended Mode

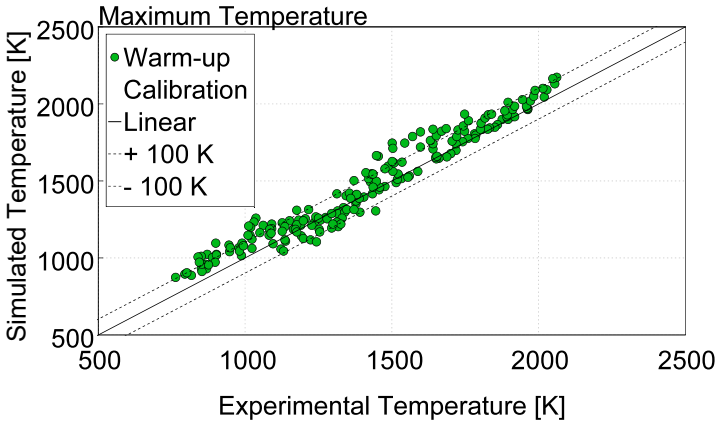


(c) Warm-up Mode

Figure 3.9: Experimental and Simulated maximum cylinder temperature

of soot emissions have been neglected since the model is able to reproduce the soot emissions for a qualitative analysis only [40].

In Fig.3.10 and 3.11 the comparison between simulated and experimental, respectively, NOx and CO emissions is shown. The agreement of the model to the experimental data is more than satisfactory considering the NOx emissions. In fact, up to a concentration of 600 ppm of NOx, the model predicts with a good accuracy the NOx emissions since more than 40% of the operating points fall in the range ±40 ppm with respect to the experimental data. Above 600 ppm of NOx, only a percentage slightly smaller than 20% of the operating points is placed in the ±40 ppm error range since the model overestimates the NOx emissions (this may be due to the fact that the in-cylinder temperature is overestimated above 2000 K, see Fig.3.9). Concerning CO emissions, the simulated and experimental operating points are scattered across the xy plan highlighting a less than satisfactory model prediction capability.

In Tab.3.1 the predictive combustion model quality using a linear regression is evaluated for the three combustion modes for the most significant engine parameters. The model shows good prediction accuracy for MFB50%, maximum in-cylinder pressure, maximum temperature and NOx emissions for Normal and Blended calibration modes. The accuracy of MFB50% for the Warm-up calibration is quite low (0.449) due to a scattering of the combustion phasing for operating points with MFB50% beyond 30° aTDCF, as see in Fig.3.7c. The accuracy of the model for the prediction of CO over the three combustion modes is low in terms of deviation from the y = x relation (i.e. the angular coefficient is far from 1) and in terms of fit of the linear regression (i.e. the R2 is low). For this reason, and since an overestimation of CO emissions affects the engine efficiency, the prediction of the CO emissions is switched off in the predictive combustion model and will not be taken into account in next phases of the work.

Table 3.1: Linear regression of experimental and simulated CPOA results for some notable engine parameters for the three combustion modes; R2 below 0.75 is highlighted in red

| | **Normal** | | **Blended** | | **Warm-up** | |
|---|---|---|---|---|---|---|
| | m | R2 | m | R2 | m | R2 |
| **MFB50%** | 0.92 | 0.94 | 0.93 | 0.92 | 0.91 | 0.45 |
| $\mathbf{P}_{max}$ | 1.05 | 1.00 | 1.05 | 1.00 | 1.05 | 0.99 |
| $\mathbf{T}_{max}$ | 1.03 | 0.99 | 1.04 | 0.99 | 1.03 | 0.95 |
| **NOx** | 1.02 | 0.92 | 1.05 | 0.93 | 1.09 | 0.93 |
| **CO** | 0.48 | 0.33 | 0.63 | 0.18 | 3.25 | 0.01 |

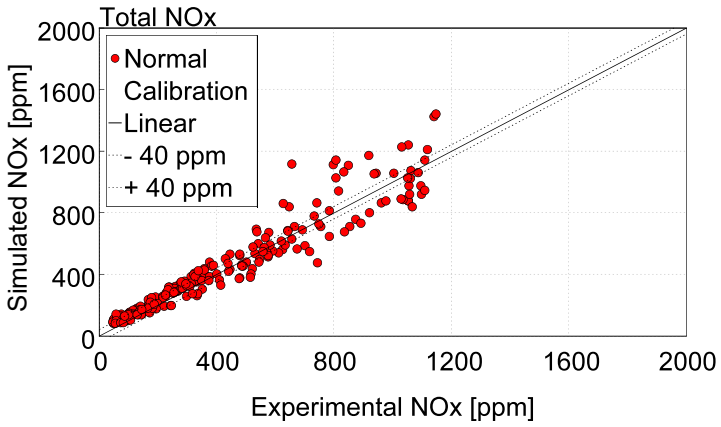


(a) Normal Mode

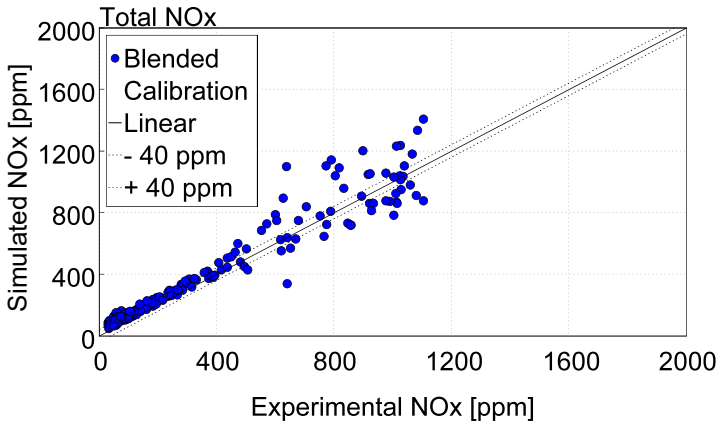


(b) Blended Mode

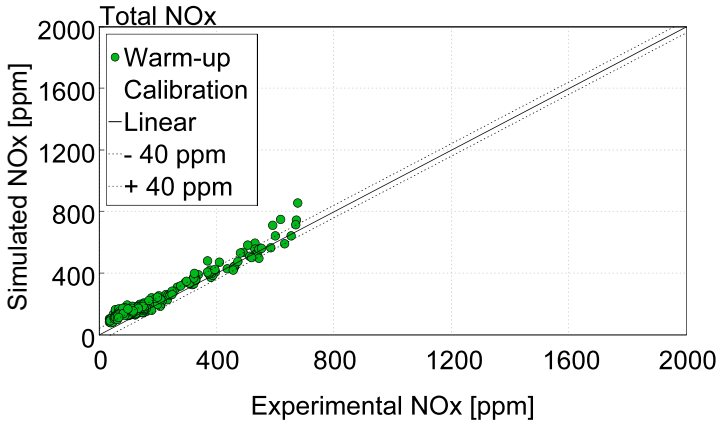


(c) Warm-up Mode

Figure 3.10: Experimental and Simulated NOx emissions

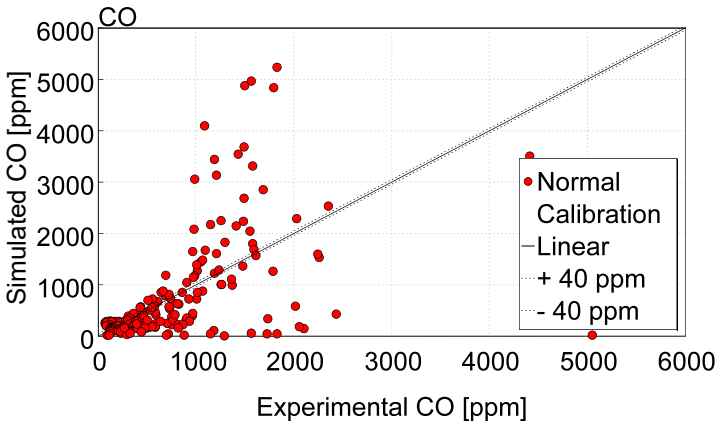


(a) Normal Mode

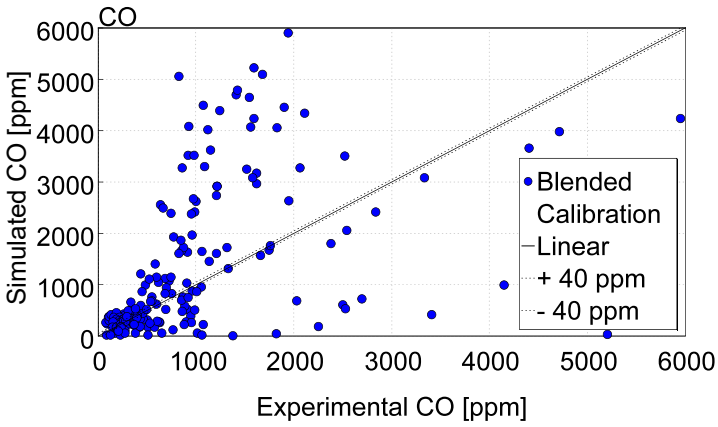


(b) Blended Mode

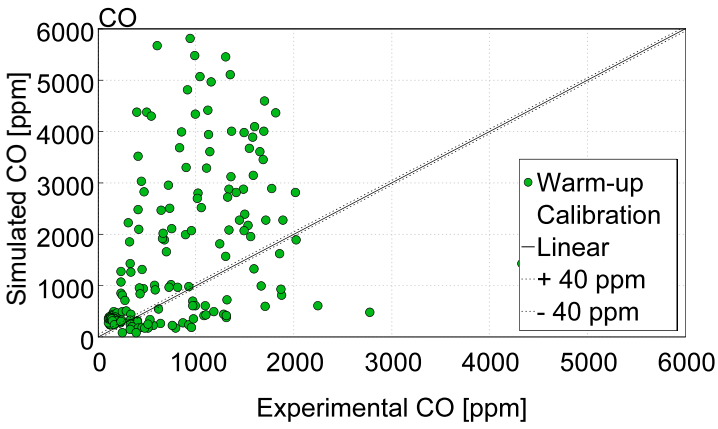


(c) Warm-up Mode

Figure 3.11: Experimental and Simulated CO emissions

## 3.2 Fast Running Model (FRM) Engine

In this section the validation of the FRM engine model is discussed. Commonly, 1D-CFD engine models are used for the evaluation of engine performance and efficiency and to assess hardware modification or innovation. These engine models are built from a detailed geometrical representation of the engine air path to account for pressure losses, wave effects and temperature gradients. With a detailed engine model properly calibrated, the accurate evaluation of several engine parameters is possible at the expense of simulation time that, for a detailed engine model ranges from 50 to above 100 times the real time. Usually, this is accepted during engine development since a steady state operating point needs only few simulation seconds (few real time minutes) to reach the convergence of the results. Conversely, when slower phenomena are to be investigated (e.g. thermal warm-up studies), the simulation time may become a bottleneck. In order to reduce the computational effort, Fast Running engine Models have been developed with the aim to guarantee a satisfactory accuracy (with deviation in the range of ±5% with respect to the experimental data) with low simulation time achieving a Real Time Factor (RTF) of 3 to 5. The starting point of a FRM engine is a detailed engine model, which, through a process of coarsening of the discretization (i.e. increasing the discretization length or lumping volumes) and subsequent model recalibration becomes a FRM engine [39]. In this work, the choice to build a FRM engine with a target RTF of 3, was driven by the need to perform driving cycle simulations with the required detail and accuracy of a 1D-CFD engine combined with acceptable simulation time. In order to rigorously mimic the warm-up during engine operation from a cold start (e.g. in the early phases of a driving cycle), a detailed thermal model of the engine cylinders, head and pistons based on a finite element method for the description of the engine geometry was employed. In addition to this, engine exhaust ports, exhaust manifold and turbine volute have been represented as lumped masses with heat transfer areas, to reproduce their thermal inertia during warm-up. A Chen-Flynn engine friction relation has been used for the instantaneous computation of the engine Friction Mean Effective Pressure (FMEP). The formula is reported in Eq.3.1, where $Pcil_{max}$ is the maximum in-cylinder pressure, $u$ is the average piston speed and $A$, $B$, $C$ and $D$ are the calibration constants. In order to account for cold start operation, the constant part of the FMEP (e.g. the $A$ parameter) depends on the coolant temperature according to a quadratic polynomial relation [42].

$$FMEP = A + B \cdot Pcil_{max} + C \cdot u + D \cdot u^2 \tag{3.1}$$

Moreover, since in GT-SUITE the combustion noise was not available directly as a simulation result, the user subroutine developed and validated by Piano [42] was used.

> First, the power spectrum of the cylinder pressure signal was obtained through a Fast Fourier Transform. A digital low pass filter was applied to clean the signal from the high-frequency content, related to normal modes

of the gas and acquisition's noise, which is not meaningful as far combustion noise is concerned [43]. At this end, GT–SUITE provides different digital filters [43]. In this analysis, the 24th order one was used, which provides full attenuation for frequencies higher than half of the maximum one in the spectrum. The power spectrum of the signal was divided in octave bands and the attenuation, introduced from the engine structure and the human ear, was applied according to the AVL [44, 45] and A weighting curves respectively.

### 3.2.1 FRM Engine Control Unit

Direct injection turbocharged diesel engines require a proper control of the complexity of the injection system and of the air management system in order to achieve low fuel consumption and low pollutant emissions. Usually, calibration maps that are assessed on the engine test bench for steady state operating points, contain the optimal values to control the engine across the entire operating map. In order to properly operate the FRM engine, three different calibration maps (one for each combustion mode: Normal, Blended and Warm-Up) that contain the control parameters, mapped as function of engine speed and total injected fuel mass or target torque, are used. These control parameters are the boost pressure target, the minimum allowed air to fuel ratio (i.e. the so called smoke limit), the EGR ratio and the swirl rate as far as the air management is concerned. Regarding the injection system, the calibration maps provide rail pressure, injection mass fraction for four different injections (two pilot injections, a main injection and an after injection) and the Start Of Injection (SOI) of the four injections. The temperature of the Charge Air Cooler (CAC) is controlled to reproduce the test bench CAC temperature. In addition to calibration maps, Proportional Integrative (PI) controllers are required to guarantee the achievement of mapped set-points. For this reason, three different PI controllers were introduced to control the boost pressure by acting on the VGT rack position, to control the EGR rate and to control the engine brake torque by acting on the total injected fuel mass. The boost pressure maps required by the VGT controller (one for each combustion mode) depend on the engine target torque and the engine speed while injection mass fraction, SOI, rail pressure, swirl rate and EGR ratio are function of the engine speed and on the total injected fuel mass (which is provided by the injection controller). In App.A, the controlled brake torque, the controlled air flow rate and the manifold volumetric efficiency of the FRM with respect to the experimental data are shown are reported in detail. The difference in manifold volumetric efficiency between the model and the experimental data about + 5 %, which is acceptable for this FRM engine developed for simulation time close to real time.

### 3.2.2 FRM Engine Steady-state Validation

Although a FRM engine is built from a detailed geometrical representation of the engine, the discretization may reduce the accuracy of the model. For this reason, the deviation between experimental and simulation engine performance, air and fuel mass flow rates, pressure and temperature along the engine air path should be evaluated. To do this, the FRM engine is operated to reproduce the behaviour of the engine at the test bench in steady state operating points and the error between experimental data and simulation is assessed. For the sake of brevity, in Fig.3.12 and 3.13 only the BSFC and the BSNOx of the FRM engine are here compared with the experimental data. Concerning the BSFC, the majority of the operating points (about 70% for Normal Mode combustion, above 75% for Blended Mode combustion, above 50% for Warm-Up Mode combustion) lies in a range ±5 % with respect to the experimental data both in warmed-up conditions. In App.A, in Fig.A.2 and A.3 model results and experimental data are compared also in cold conditions (i.e. coolant temperature kept at 40 °C for the Blended and Warm-up combustion mode. On average, about 40% of the engine operating points deviates from the experimental data less than ±5 %. A scattering of points for higher experimental BSFC is noticeable for Blended and Warm-up combustion mode due to a worsening of the prediction capabilities of the combustion model at low engine load. As far as the BSNOx is concerned, the error between experimental data and model is wider than for the BSFC and a significant part of the operating points lies in the range ±20 % (about 55 % for Normal Mode combustion, above 40% for Blended combustion and Warm-up combustion and around 30% for Blended and Warm-up combustion mode in cold condition). The scattering of the BSNOx points is wider than for the BSFC due to the exponential dependence of the NOx oxidation rate from the in-cylinder temperature and small deviations of the in-cylinder temperature above 2000 K, cause great variation of the NOx emissions.

In order to analyse the impact of BSFC and BSNOx error across the engine operating map, in Fig.3.14 and 3.15 the difference of the experimental and simulated BSFC and BSNOx as a function of engine speed and engine torque is, respectively, shown. When the calibration of the Normal combustion mode is selected, there is a slight overestimation of the fuel consumption by the FRM engine up to 6 % for high speed and high load engine operating points. At low engine load and speed below 3000 rpm, the fuel consumption is underestimated and in the Low End Torque (LET) region the difference between experimental data and model is close to zero. The operating map of the Blended combustion mode shows a wide area where the relative difference of fuel consumption difference is below 2 % (in absolute value). Similarly to the Normal combustion mode, although in a narrower area, at high load and high speed (above 2500 rpm and 150 Nm) the FRM overestimates the fuel consumption by up to 6 %. At low load (below 50 Nm) and low speed (below 3500 rpm) the fuel consumption is underestimated. Finally, when adopting the Warm-up combustion mode, the FRM engine overestimates the engine fuel consumption at high speed and load and underestimates the fuel consumption at

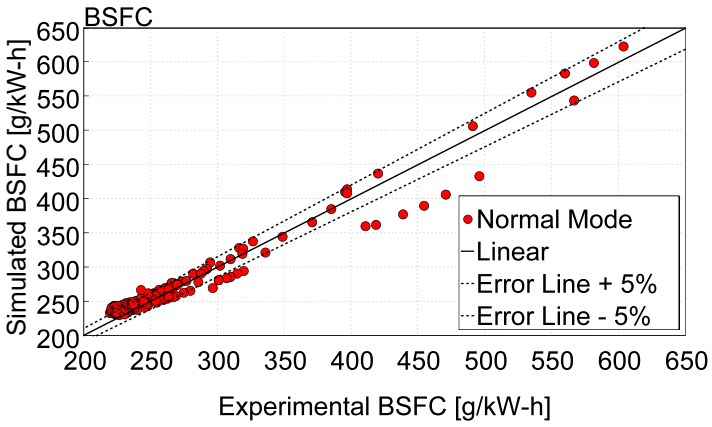


(a) Normal Mode

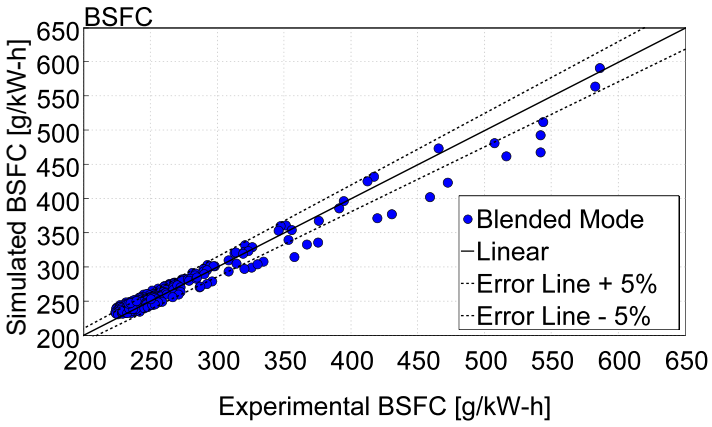


(b) Blended Mode

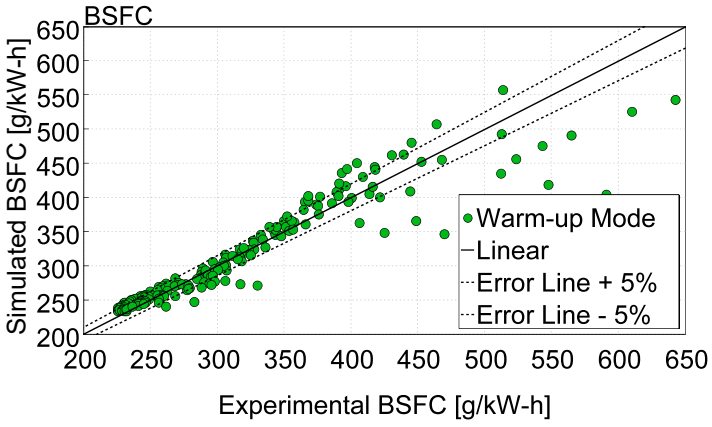


(c) Warm-up Mode

Figure 3.12: Experimental and Simulated BSFC

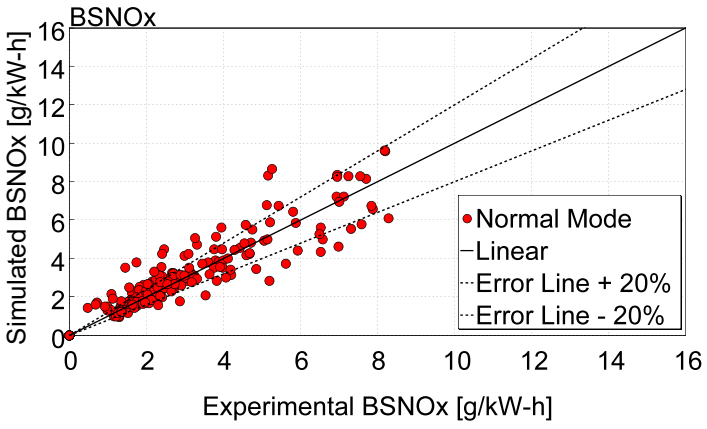


(a) Normal Mode

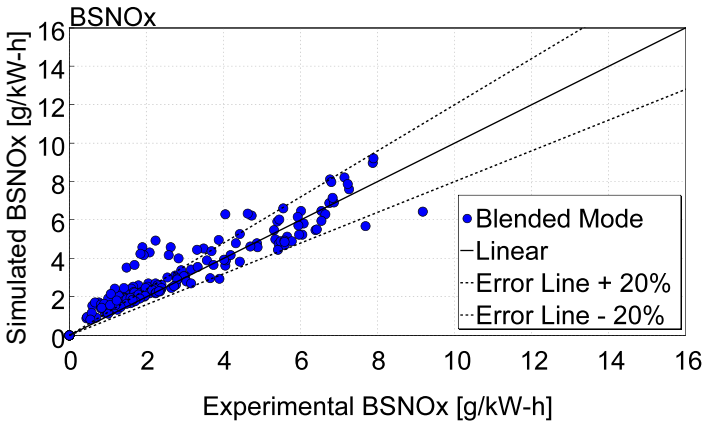


(b) Blended Mode

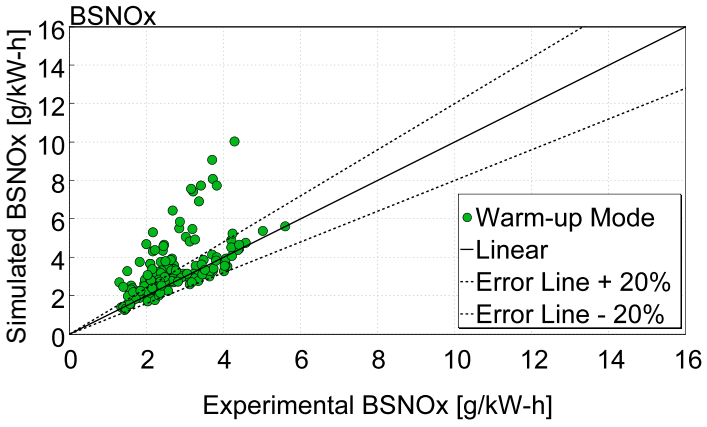


(c) Warm-up Mode

Figure 3.13: Experimental and Simulated BSNOx

low load and low speed. Concerning the model error in terms of BSNOx, the FRM overestimates by up to 60 % the specific NOx emissions at low load (below 50 Nm), up to 40% in the LET region while the NOx emissions are underestimated by low than - 40 % in a region surrounding 1500 rpm and 100 Nm when the Normal combustion mode is adopted. In the Blended combustion mode the overestimation of the NOx emissions is significant across a wide area from 2000 rpm to 4000 rpm and below 200 Nm. Except for the LET area, where the model overestimates by 20 % the NOx emissions, at load above 200 Nm the model overestimates the BSNOx by less than 20 %. In the Warm-up combustion mode, the region below 50 Nm is characterized by a overestimation of the BSNOx by more than 40 %. In the other part of the engine operating map, the error is in the range ±10 %.

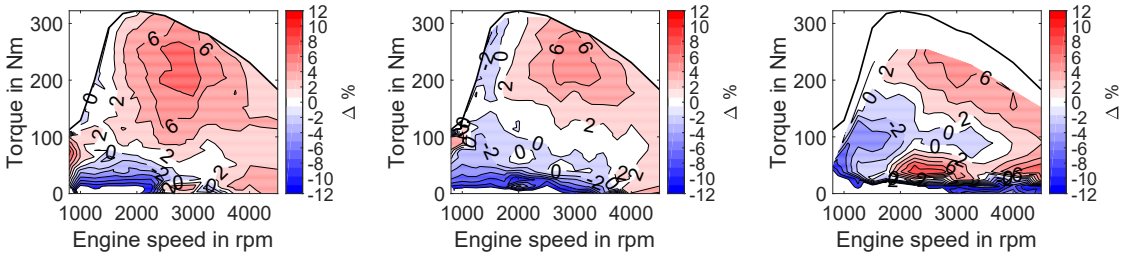


(a) Normal Mode (b) Blended Mode (c) Warm-up Mode

Figure 3.14: BSFC numerical experimental percentage difference across the engine map

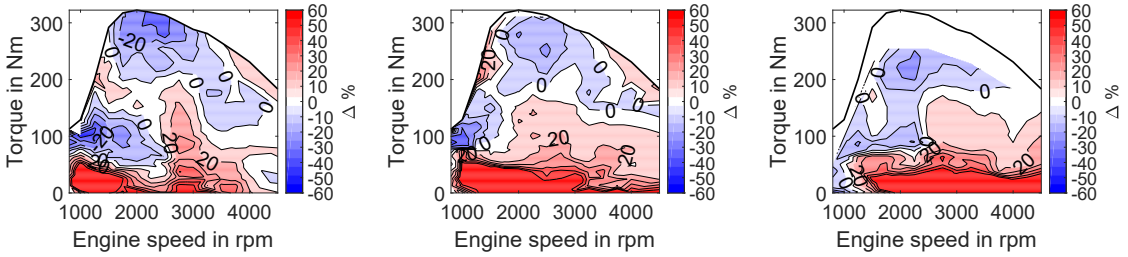


(a) Normal Mode (b) Blended Mode (c) Warm-up Mode

Figure 3.15: BSNOx numerical experimental percentage difference across the engine map

In Tab.3.2 the FRM engine quality is evaluated using a linear regression (in term of slope $m$ and correlation coefficient $R^2$) for the three combustion modes for some significant engine parameters. As previously seen in a different fashion, the model shows good prediction accuracy as far as the BSFC is concerned. The slope is equal to 1.01 for the Normal combustion mode since the model, as already seen in Fig.3.12 and 3.14, overestimates moderately the fuel consumption. Overall, the Blended and Warm-up combustion mode, both in hot and cold condition, only minimally underestimate the fuel consumption with a slope of 0.98 for Warm-up combustion mode in hot condition

and 0.99 for the other combustion modes. The slope representing the trend of BSNOx is close to linearity for Normal and Blended combustion mode (respectively 1.01 and 1.02), and it is in the range 1.16 to 1.19 for the Blended mode in cold condition and the hot and cold Warm-up combustion mode. Except for the Blended mode, where the correlation coefficient is equal to 0.83, a linear regression is only moderately able to represent the scattering of the BSNOx. The model is able to properly predict the Air to Fuel Ratio (AFR) with slopes that range from the perfect linearity of the Blended mode in cold condition and a close to linear relation for the Normal combustion mode, to a overestimation of 20% of the AFR for the Warm-up combustion mode in hot condition. The correlation coefficient is above 0.9 for any combustion mode. The temperature after the turbine (T4), which is significant for the warm-up of the exhaust aftertreatment system, is slightly overestimated (by 10% on average). Finally, concerning the Heat Rejection of the engine (i.e. the power that the engine exchanges with the cooling circuit), the slope is below 1 for Normal and Blended combustion mode (respectively 0.84 and 0.79), while no experimental data were available for the other combustion modes. This low value is due to a underestimation of the coolant power at high load of the engine, while at low engine speed the cooling power is overestimated.

Table 3.2: Linear regression of experimental and simulated engine FRM results for some notable engine parameters for the three combustion modes - H hot, C cold condition; R2 below 0.75 is highlighted in red

| | **Normal H** | | **Blended H** | | **Warm-up H** | | **Blended C** | | **Warm-up C** | |
|---|---|---|---|---|---|---|---|---|---|---|
| | m | R2 | m | R2 | m | R2 | m | R2 | m | R2 |
| **BSFC** | 1.01 | 0.95 | 0.99 | 0.94 | 0.98 | 0.88 | 0.99 | 0.94 | 0.99 | 0.92 |
| **BSNOx** | 1.01 | 0.80 | 1.02 | 0.86 | 1.19 | 0.35 | 1.16 | 0.19 | 1.19 | 0.36 |
| **AFR** | 1.04 | 0.94 | 1.07 | 0.96 | 1.21 | 0.91 | 1.00 | 0.96 | 1.08 | 0.97 |
| **T4** | 1.08 | 0.96 | 1.07 | 0.98 | 1.07 | 0.89 | 1.11 | 0.86 | 1.12 | 0.82 |
| **Heat Rej.** | 0.84 | 0.94 | 0.78 | 0.93 | - | - | - | - | - | - |

### 3.2.3 FRM Engine Time To Boost Validation

Once the FRM engine is validated during steady state operation, Time To Boost (TTB) validation is needed to assess the predictive capability of the model during a load step. A TTB test, done on an engine test bench, is composed by a preconditioning of the engine at fixed speed and load (in this test case a preconditioning load of 20 Nm was adopted) and a subsequent request of full engine load to the engine (maintaining the speed constant). The same approach is followed in the virtual test bench developed for this work: the engine, preconditioned at partial load, reacts to the request of maximum torque with an increase of the injected fuel mass (limited by the AFR limit) and moving the VGT rack position towards reduced flow permeability to extract higher power

from the exhaust gases (since the boost pressure set-point increases to the increase in requested torque). The other controlled quantity, in the engine virtual test bench, are actuated by means of the calibration maps already discussed, on the basis of engine speed and actual injected fuel mass.

In Fig.3.16, some engine parameters are evaluated during a TTB at 1500 rpm. In the figure, engine physical quantities as injected mass of the main injection, air mass flow rate and the temperature at turbine inlet are shown. The model replicates with good accuracy, during the TTB at 1500 rpm, the air mass flow rate of the engine and the temperature before the turbine. Additional engine parameters, such as main injection SOI, EGR rate, swirl valve actuation, are presented in Fig.A.4 in App.A. The slight deviation of the swirl valve actuation along the transient is due to the fact that the model uses the results from the interpolation of the calibration maps and does not take into account specific control strategies during transient operation.

The results of the TTB over different engine speeds (from 1000 to 2000 rpm) in terms of transient brake torque is shown in Fig.3.17. The engine model accurately reproduce the engine torque build-up in any investigated speed. More in detail, at 1000 rpm there is a small overestimation of the maximum engine brake torque, equal to 13 Nm. This discrepancy is due to the fact that at LET the performance of the turbocharger drives the overall maximum attainable torque of the engine and only small deviation in the turbine data have a big impact on engine performance. As a matter of fact, although experimental VGT data are preprocessed by GT-SUITE to fit physical relations in order to properly predict the turbine behaviour across and outside the available performance map of the turbine [46], the quality of experimental data may not be reliable enough for an accurate fitting. At 1500 rpm, while a small overestimation of the brake torque is noticeable (with a maximum deviation of 31 Nm at 10 s), the torque build-up along the 12 s of the TTB transient is well replicated. Finally, at 2000 rpm the torque gradient is accurately reproduced; the difference of less than 18 Nm at 14 s is considered acceptable for a detailed engine model which is required to have computational time close to real time (around 5%). The full load rated torque is achieved by the FRM in steady state operation when the engine achieves the thermal balance.

## 3.3 Vehicle

In this section, the comprehensive vehicle model is described. Besides the 1D-CFD FRM engine already described, a 0D mechanical model has been chosen for vehicle and driveline modelling. In GT-SUITE, standard driveline components and connections that can be used to construct various driveline layouts and configurations, are available [47]. For example, axle, differential, shafts, tyres and vehicle model can be connected with either rigid or slipping connections to build the driveline. Each component usually includes the inertia term.

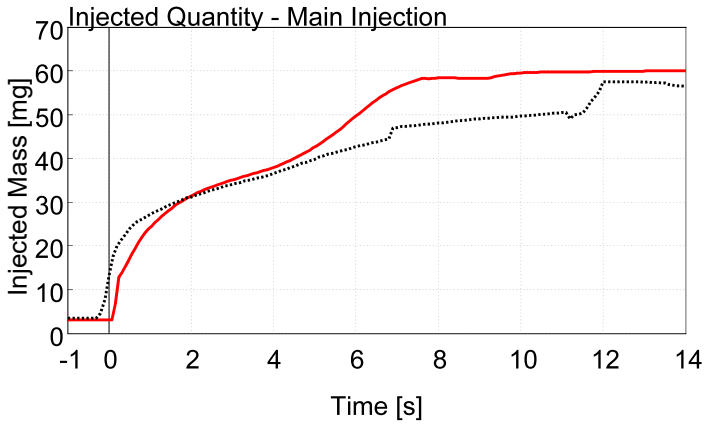


(a) Main Injection Quantity

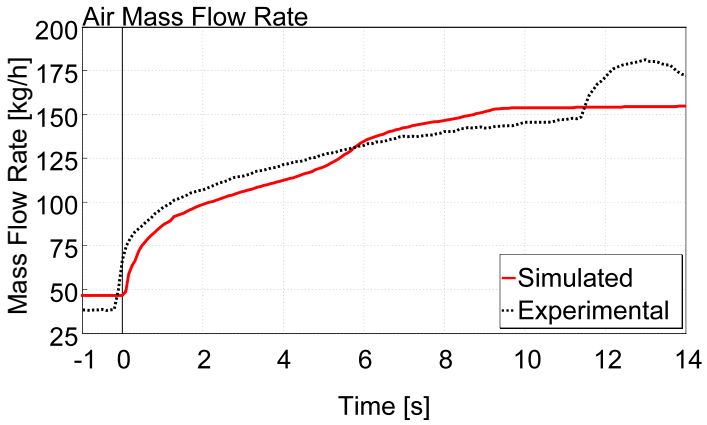


(b) Air Mass Flow Rate

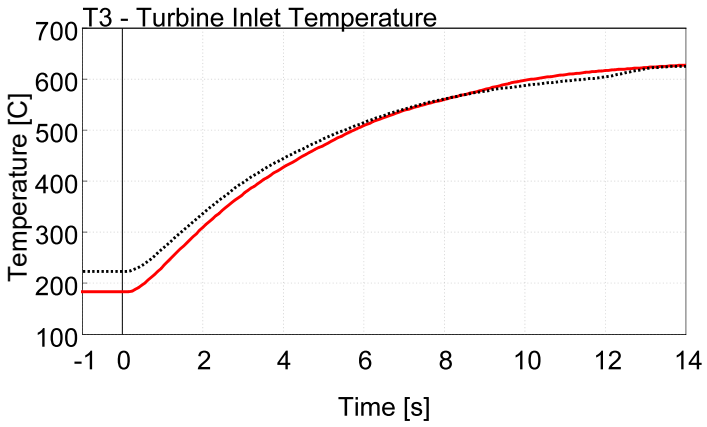


(c) T3 - Temperature at turbine inlet

Figure 3.16: TTB at 1500 rpm in Normal combustion mode - Engine parameters

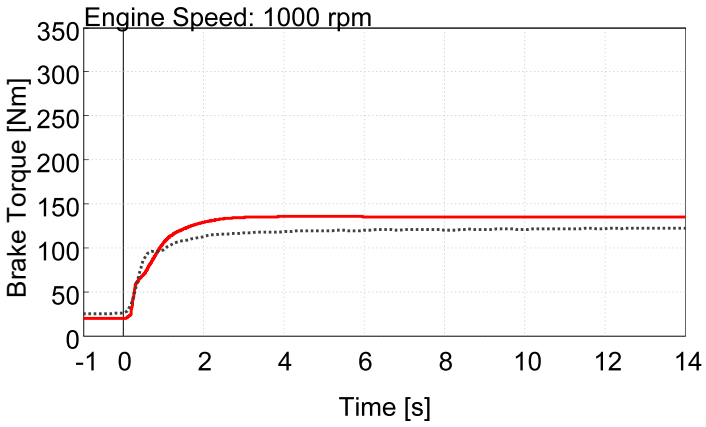


(a) 1000 rpm

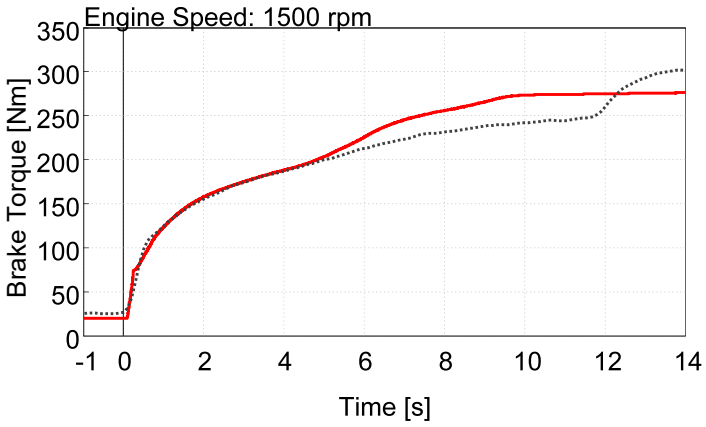


(b) 1500 rpm

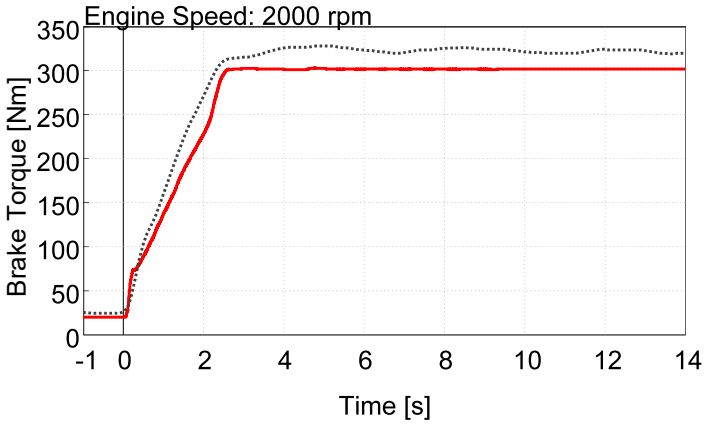


(c) 2000 rpm

Figure 3.17: TTB at different engine speeds in Normal combustion mode - Brake Torque

The main specification of vehicle road load and driveline have already been presented in Cha.2. Since the road loads were determined including transmission losses, no transmission efficiency was taken into account in the model. The experimental gear shifting pattern has been used for the conventional 12 V vehicle validation and for the 48 V mild hybrid vehicle validation.

The integration of the FRM in the virtual test rig provides a high level of accuracy for the fuel consumption evaluation also in highly dynamic driving cycles, as proved by Millo et al. [31]. It is worth noting that the fuel flow rate in this way is not estimated by interpolating a performance map, but is the result of a fully-physical engine model, that reproduces transient phenomena as the turbolag effect and the mechanical inertia of the components, which are crucial for the air charging operation and consequently for the fuel consumption. Moreover, in this way, it is also possible to evaluate vehicle performance during tip-in manoeuvres for which mechanical and fluid dynamics transient phenomena as turbolag need to be correctly captured. The development of a FRM engine has been presented so far, but a comprehensive powertrain and vehicle model requires the modelling of additional engine systems as the coolant circuit and the exhaust gas aftertreatment system.

### 3.3.1 Coolant circuit model

The coolant circuit model have been already developed in a previous activity done by Millo et al. [34] and it has been adopted for this work. This coolant circuit model is based on a detailed 1D-CFD representation of the system piping based on the geometry of the system. Pressure drop and heat exchange along the circuit have been calibrated according to experimental data. Additionally, ”radiator was modeled using a detailed representation that considers the geometrical characteristics and the thermal inertia of the wall material of the component” and the heat transfer coefficients as well as the pressure drop through this components have been calibrated to match the experimental data [34]. The switchable pump (SWP), by which it is possible to interrupt the flow of coolant within the coolant jacket during the early phases of the cycle to reduce the engine warm-up time, is described with measured performance data that correlates pump speed, flow rate, pressure rise and pump efficiency. The coolant pump is controlled with a switch that actuates a clutch which links the coolant pump with the engine when the coolant temperature has reached a certain temperature threshold (55 °C). The thermostat lift is defined on the basis of the coolant temperature and its working hysteresis as a function of the temperature has been taken into account. In order to couple the coolant circuit model with the FRM engine model, instead of heat rejection maps used for the work done in [34], the engine heat transfer power to the coolant is sent to the coolant model. This, provides the coolant temperature as boundary condition for the FRM engine. In addition to that, the EGR coolant power considered as secondary source of heat power for the coolant circuit. In order to cool the exhaust gases passing through the EGR valve, a simple cooler, defined in terms of coolant temperature (provided by the

coolant circuit model) and effectiveness (which depends on the exhaust mass flow rate), is modelled. Finally, Eq.3.2 is used to compute the dynamic air pressure at radiator inlet from the vehicle speed and, ultimately, the air flow through the radiator. In Eq.3.2, $p_{total}$ is the total pressure before the radiator, $p_{static}$ the static pressure, $c_{pc}$ is the ram air pressure coefficient which is used to tune the pressure drop across the radiator accounting for model approximation, $\rho$ is the air density and $V$ is the vehicle speed.

$$p_{total} = p_{static} + \frac{1}{2} \cdot c_{pc} \cdot \rho V^2 \tag{3.2}$$

### 3.3.2 Aftertreatment system model

The aftertreatment system model was provided by GM-GPS and it is a 1D-CFD detailed model of the exhaust aftertreatment system. The model consists in a flow inlet with imposed boundary conditions (from the FRM engine), a series of parts that describe geometrically the aftertreatment flow path, and a flow outlet representative of the ambient air. Additional objects, where the reactions take place, represent the catalyst devices which are placed along the flow path. Chemical kinetics, according to the Arrhenius reaction formulation, are used to describe the oxidation and reduction reactions on the DOC and SCR. The aftertreatment model consists of different catalytic objects: three different DOC bricks and a SCRoF brick. While the upstream brick represent an Electrically Heated Catalyst (EHC) with a lenght of 9 mm and the opportunity to apply a heat rate to the metal structure, the middle and the downstream DOC bricks represents the traditional DOC. The choice to model different bricks allows to represent different reaction regions along the DOC. The SCRoF brick, close coupled with the DOC, is modelled as a single catalyst brick and the impact of soot filtration on pressure losses is neglected. The reactions and the reaction rates adopted for DOC and SCRoF are provided by GM-GPS as encrypted model. In order to effectively reduce NOx, the SCRoF requires the injection of urea (commercially available as aqueous urea solution called AdBlue which decomposes to form ammonia ($NH_3$). This composite is used in the model and injected upstream of the SCRoF. In order to properly provide the SCRoF with the optimal amount of the reducing agent a dosing control strategy for the ammonia has been developed. In order to avoid injection before the SCRoF light-off, the injection is disabled below 180 °C. Above this temperature threshold, the ammonia is injected following Eq.3.3, where $\dot{m}_{amm}$ is the ammonia mass flow rate, $\dot{m}_{exh}$ is the exhaust gas mass flow rate, $[NOx]$ is the molar concentration of nitrogen oxides in the exhaust gas, $M_{amm}$ is the molar mass of ammonia and $M_{exh}$ is the molar mass of the exhaust gas. Finally, $\alpha_{amm}$ is the ammonia dosing factor. Ideally, an $\alpha_{amm}$ equal to 1 allows the complete reduction of the NOx species. However, since the NOx storage capacity of the SCR is inversely proportional to the SCR temperature a more refined dosing control strategy that accounts for the injected ammonia that is stored on the SCR or released to the exhaust gas is needed. There are different control strategies for the NOx dosing

[48] and for this work a closed loop strategy that takes into account the actual stored ammonia on the SCR is chosen. The actual stored ammonia is sensed using the SCR model itself and compared to the target storage capacity of the SCR that is shown in Fig.3.18. A PI controller acts on the $\alpha_{amm}$ in order to maintain the storage capacity that guarantees the optimal conversion efficiency of the SCRF. This dosing control strategy may be implemented in a vehicle using a NOx sensor upstream of the SCRF and an ammonia sensor downstream the SCRF and a storage capacity model. Moreover, in this study it is neglected the presence of an additional underfloor SCR, which is usually adopted for the compliance with current EU6D and RDE legislation or in more complex aftertreatment system for ultra-low NOx emissions[49].

$$\dot{m}_{amm} = \dot{m}_{exh} \cdot [NOx] \cdot \frac{M_{amm}}{M_{exh}} \cdot \alpha_{amm} \tag{3.3}$$

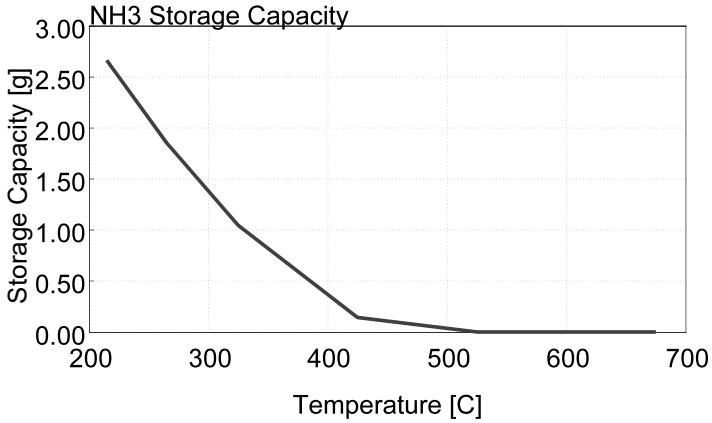


Figure 3.18: $NH_3$ storage capacity on the SCRF

Since the FRM engine is able to accurately predict carbon dioxide ($CO_2$) and nitrogen oxides (NOx), emissions maps evaluated at the engine test bench in steady state operating points are used for total unburned hydrocarbons (THC) and carbon monoxide (CO). The concentration of these pollutants will be imposed at the engine outlet depending on engine speeds and fuel injected mass. In this way, the aftertreatment system receive plausible boundary conditions and the comprehensive vehicle model can be used as virtual test bench to correctly predict tailpipe emissions. The aftertreatment model was fed with two separate hydrocarbon emissions, propylene and diesel vapour to represent partial and incomplete combustion and more accurately reproduce the oxidation mechanism on the DOC.

Due to software limitations in the managing the high concentration variability in terms of carbon monoxide emissions, the reaction rates for the CO oxidation were disabled. In Fig.3.19, the impact of the deactivation of carbon monoxide reactions on the DOC outlet temperature due to the exothermic oxidation of the carbon monoxide, the

conversion efficiency of THC and NOx in the DOC and the SCRF, along the WLTC, are respectively shown. With the inhibition of the carbon monoxide reactions the temperature after the DOC is lower by more than 20 °C at 100 s and after 144 s the DOC is less effective in promoting the oxidation of THC. Finally, the lower activity of the exothermic reaction in the DOC and the difference in the ratio nitrogen dioxide over nitrogen oxide reduces the SCR conversion efficiency in the early stages of the driving cycle. At the end of the cycle the difference in terms of SCR conversion efficiency is below 1%.

### 3.3.3 In-vehicle engine integration

The integration of the engine in the powertrain and vehicle model requires some steps. First, since three different combustion modes may be used, a simple rule for the mode selection is followed. The Warm-up combustion mode is selected in a cold start condition until the temperature after the DOC reaches a temperature of 210 °C. At this threshold the Blended combustion mode is chosen until the temperature after the DOC reaches a temperature of 250 °C or the engine coolant reaches a temperature of 67 °C (at lower coolant temperature the EGR cooler is bypassed to avoid the condensation of the exhaust gas water vapor that would foul up the EGR lines and cooler). Above this temperature threshold the Normal combustion mode is enabled unless lower DOC temperature or coolant temperature forces the adoption of Blended combustion mode, or, after a prolonged cooling down, the Warm-up combustion mode is needed.

The idle speed of the engine is dependent on the coolant temperature and it ranges from 1100 rpm at −30 °C to 750 rpm at 90 °C.

The vehicle model boost target was updated with the model results in order that the FRM engine air flow is comparable with the experimental one.

Moreover, a Start and Stop control is introduced in the model. The Start and Stop switches the engine off when the engaged gear is equal to zero and the vehicle speed is below 4 km/h. The cut-off strategy is introduced and activated whenever the brake torque request is negative and the engine speed is above 1100 rpm.

Finally, the vehicle driver is simulated by means of a proportional-integral controller that defines the required power, the brake pedal and the clutch position. The engine Electronic Control Unit (ECU) behaviour is mimicked in the engine model by means of controllers which translate the driveline torque request from the driver into a torque target and in a boost pressure target. The values of injection mass fraction, SOI, rail pressure, swirl rate and EGR ratio are defined from the combustion mode (i.e. the calibration map) selected, in the same manner as done on the FRM engine model.

The subsystems are modelled independently and they adopts different solver. The explicit solver is used for the time integration of the fluid dynamics of the FRM engine since it is suited for highly unsteady flow while for the cooling circuit adopts the implicit solver since it is more computationally efficient for fluid systems when there are minimal wave dynamics in the system. A Quasi-steady approach is followed to solve the 1D governing equations of the aftertreatment system. This solver is designed for fast

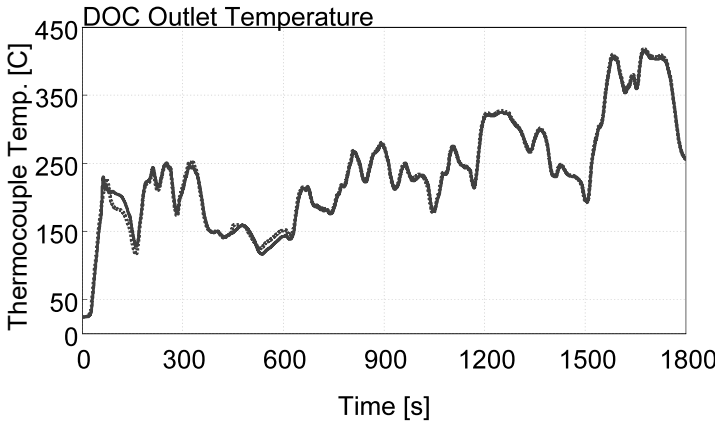


(a) DOC Outlet Temperature

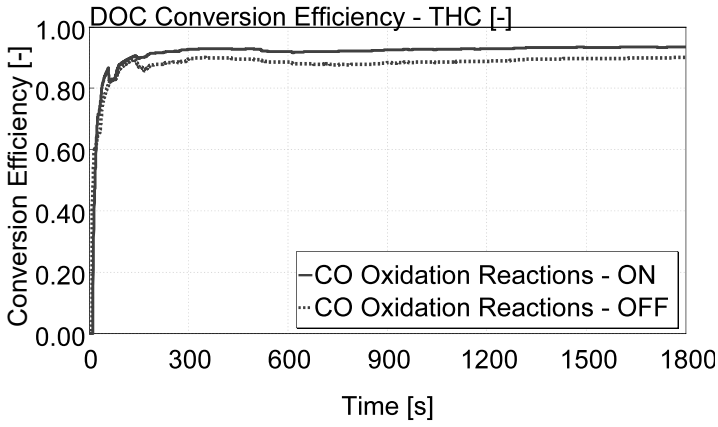


(b) THC Conversion Efficiency

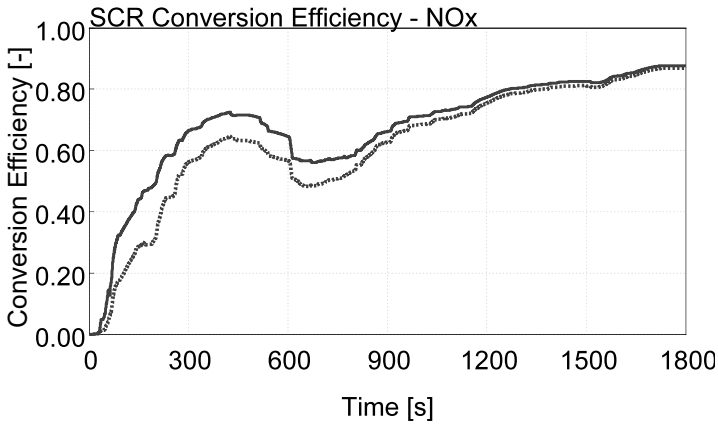


(c) NOx Conversion Efficiency

Figure 3.19: Impact of CO reactions

running chemical kinetic applications and is computationally efficient. The integration of the powertrain subsystems requires that these components are linked together in such a way that physical quantities are synchronously exchanged. The main physical signals are represented in App.A in Fig.A.6. As an example, the engine, which is controlled in load mode, provides a brake torque to the flywheel, which propels the vehicle and by means of the engaged gear defines the engine operating speeds. Moreover, the in-cylinder heat transfer directly affects the cooling circuit temperature which in turns has an impact on the combustion chamber temperature and on the engine friction. Then, the aftertreatment circuit determines the tailpipe emissions on the basis of the engine exhaust gas mass flow rate, the exhaust temperature and the exhaust pollutant concentrations.

It is to be pointed out that, in order to guarantee consistency among results, the same vehicle model can be equipped with different powertrain technologies in a click. The vehicle model is indeed built on a modular approach and any subsystem, being the air path downstream the turbine (where the eSC may or not be present) or the electric network (being it 12 V or 48 V), among the others, can be swapped in the full vehicle model with no impact on the other part of the powertrain and the vehicle. The engine system, on the other side, is kept the same, being it operated in steady state or transients, alone or integrated as propulsion system in the vehicle model. This means that the comprehensive vehicle model configures as a simulation platform where the deterministic effect of a single technology can be explored and analysed to the root cause.

A RTF of 6.5 was achieved for the comprehensive powertrain and vehicle model driving the WLTC, on a Intel i7 processor with a frequency of 3.6 GHz.

### 3.3.4 Conventional vehicle validation

In this section the validation along WLTC driving cycle of the conventional vehicle is presented. The vehicle is preconditioned along a WLTC in order that the ammonia stored on the SCRF at the beginning of the driving cycle is equal to the value at the end of the preconditioning driving cycle. Since on the test bench, electric load were externally supplied, simulations are performed assuming no electric load on the electric network. The validation of the conventional vehicle is done comparing two different vehicle simulations to the experimental results: the first one imposes the vehicle speed coming from the WLTC regulation as target for the driver model; the second simulation uses the experimental vehicle speed as target. This comparison has been made in order to evaluate, in the range allowed by the regulation, the impact of the vehicle speed on the vehicle main parameters. The vehicle model, indeed, is not able to take into account different driver aggressiveness which may affect actual vehicle speed and engine load. As a matter of fact, even though the experimental speed trace is within the ±2 km/h moving window (see A.7), the experimental speed profile differs at some extent from the regulatory driving cycle and a skilled driver can take advantage of this vehicle

speed tolerance. On the contrary, the vehicle model follows with negligible deviation the target speed profile. The aim of this comparison is therefore to evaluate the impact of the prescribed vehicle speed which impacts engine speed and load along the driving cycle. If on the one hand, the vehicle model is able to perform the driving cycle in a deterministic way and this allows to compare different results with no external disturbances, on the other hand the impact of the driver aggressiveness on the vehicle model may not be taken into account. In Fig.3.20 the comparison between simulation results and experimental result in the last part of the WLTC driving cycle is presented. Vehicle speed is controlled by the driver model and the gear ratio is imposed. The engine torque is considerably reproduced by the vehicle model when the experimental vehicle speed is imposed as target.

Before introducing the validation in terms of emissions, the evaluation along the driving cycle of different vehicle parameters is done. In Fig.3.21 the combustion mode selection, the coolant temperature and the SCRF inlet temperature are shown. The validity of the combustion mode control has a relevant impact on carbon dioxide and nitrogen oxides engine emissions and the model switches to the Normal combustion mode after 600 s, as from the experimental data. The differences in the first phase of the cycle are limited to the fact that the models select the Blended combustion earlier, from 65 s to 97 s, and they switch back to colder Combustion modes between 300 s and 430 s. Other differences are detectable at 100 s and 430 s, which may occur during engine start and stop (which is highlighted in grey in Fig.3.21a), but they have no impact since the engine is not in operation. As far as the coolant temperature is concerned, which is of great interest to correctly take into account the thermal state of the engine, the model which mimics the experimental vehicle speed follows the experimental data with a difference below 2 °C up to a coolant temperature of 80 °C. This difference increases up to 5 °C when the WLTC reference speed is imposed as vehicle speed target to the vehicle model. There is a considerable spike in the coolant temperature difference before 300 s when the switchable pump activates. Moreover, the correct reproduction of the SCRF inlet temperature, which affects the light-off of the catalytic converter and the nitrogen oxides reduction, is presented in Fig.3.21c. The experimental temperature is compared with the temperature sensed by a 3 mm K-thermocouple model which accounts for the size and material of the thermocouple [50]. The temperature difference between experimental data and simulation results at the inlet of the SCRF is significant (up to 70 °C), but during the early stages of the driving cycle (first 300 s), the model temperature well matches the experimental one.

In order to comprehensively validate the vehicle model, in Fig.3.22 the vehicle emissions in terms of carbon dioxide and nitrogen oxides, before and after the SCRF, are presented. As already said, a close-coupled SCRoF was available in the test case but an additional underfloor SCR is intended to be used for the series production vehicle. For this reason the ammonia slip phenomena will not be taken into account in the following analysis. The underfloor SCR would operate being fed by the ammonia slip of the close-coupled SCRoF. This analysis compares the experimental emissions data with the two

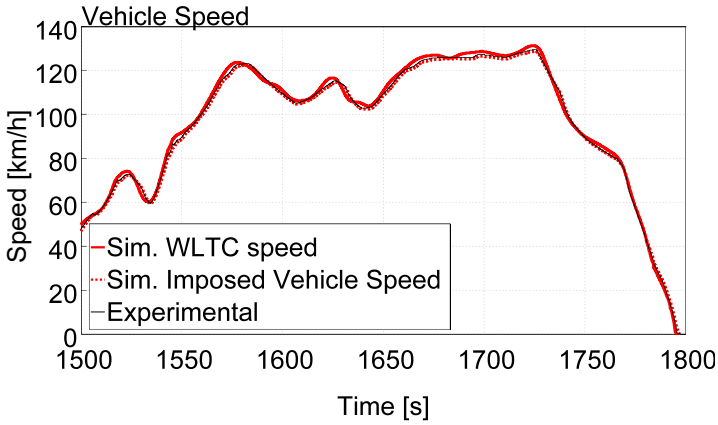


(a) Vehicle speed

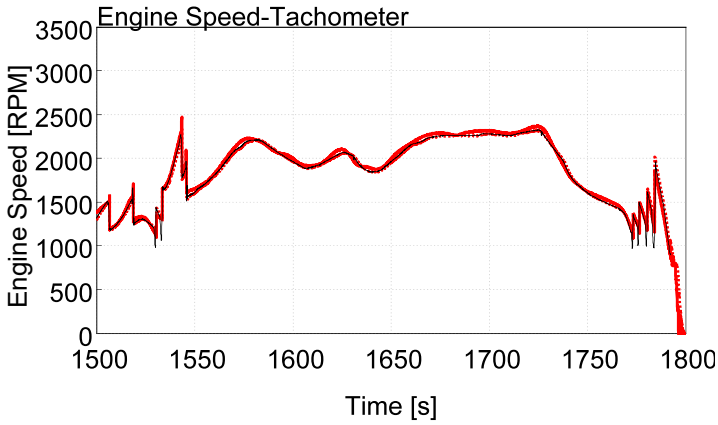


(b) Engine speed

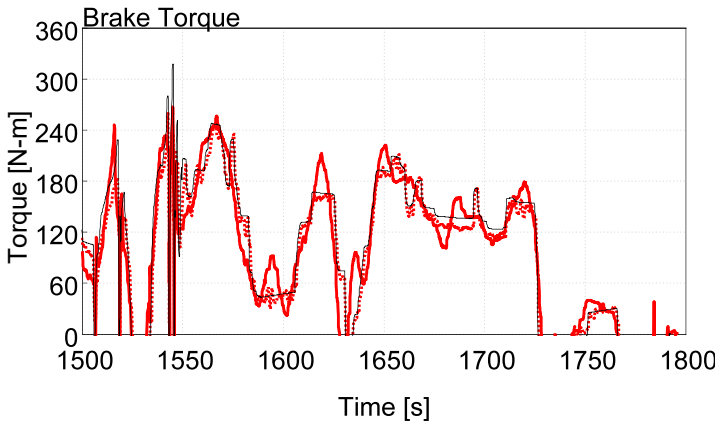


(c) Engine torque

Figure 3.20: 12 V Vehicle results - Test A - Fragment of WLTC

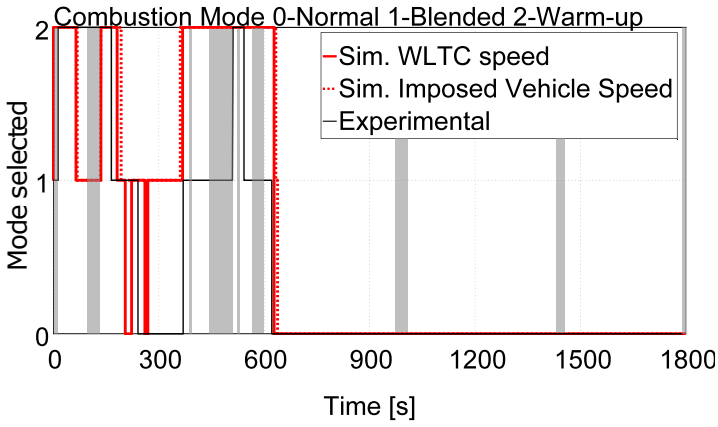


(a) Combustion Mode and Start-Stop on (grey boxes)

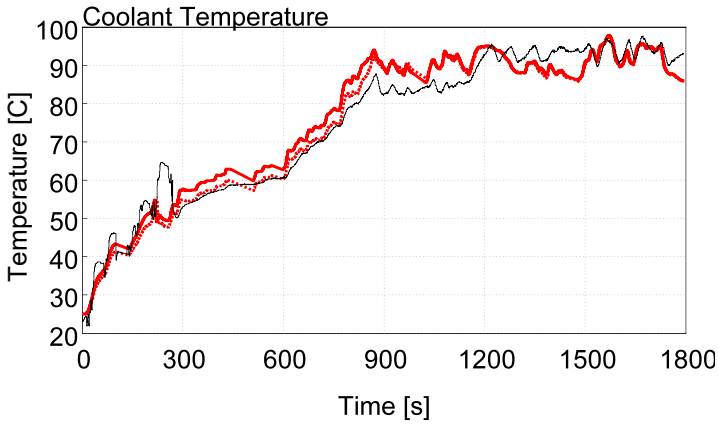


(b) Coolant circuit liquid temperature

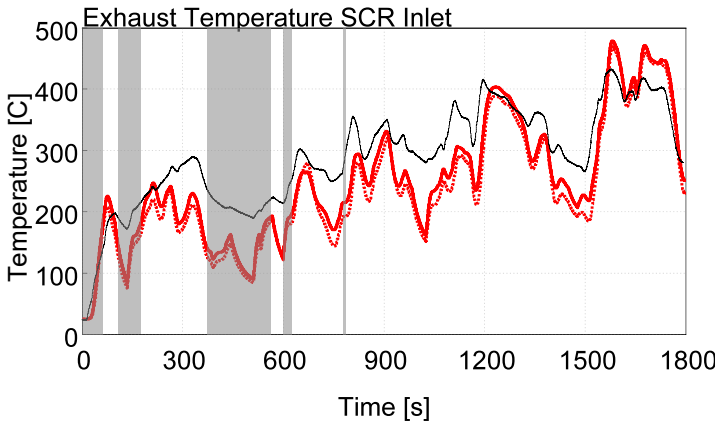


(c) SCRF Inlet Temperature and ammonia injection off

Figure 3.21: 12 V Vehicle results - Test A

different simulation results, the test where the vehicle speed of the model follows the experimental data and the additional test where the vehicle speed follows the regulatory WLTC speed. Hence, the comparison of the two simulation results has the objective to validate the model and to suggest a tolerance on the results based on different boundary vehicle speeds. The simulation results shows that the cumulated emission is slightly underestimated between 600 and 1600 s if the experimental vehicle speed is imposed as target, while when the WLTC regulatory speed the cumulated emissions are overestimated after 1200 s. Similarly, engine out nitrogen oxides are overestimated when the WLTC regulatory speed is imposed as target but the experimental speed allows to reproduce well the Engine-Out (EO) nitrogen oxides cumulated emissions. Tailpipe-Out (TO) nitrogen oxides cumulated emissions are well reproduced up to 400 s for both cases, while the vehicle model which follows the experimental speed produces higher nitrogen oxides at 800 s and up to the end of the driving cycle. Finally, the experimental tailpipe nitrogen oxides emissions increase in the final part of the WLTC cycle beyond 1500 s, but the vehicle model shows a almost flat behaviour. This may be due to the difference in the injection control strategy between model and test vehicle since the SCRoF inlet temperature are well reproduced in this phase of the driving cycle.

In Tab.3.3, the percentage deviation between model and experimental test is reported. If the experimental speed is imposed to the model the deviation in terms of final carbon dioxide emissions is equal to - 0.4 %, of - 0.3 % when the engine out nitrogen oxides emissions are concerned and an higher tailpipe nitrogen oxides emissions of + 19.9 %. The adoption of the regulatory WLTC vehicle speed increases the deviation of carbon dioxide to + 6.7% and of engine out nitrogen oxides to + 9.8%. Finally, the model overestimates the tailpipe nitrogen oxides emissions by + 5.3 %. To summarize, the choice of the prescribed vehicle speed has a non negligible direct impact (by increasing the engine speed and load) on the engine-out emissions and indirectly (by increasing the exhaust temperature) on the conversion efficiency of the aftertreatment. Similar results were obtained by Maggio [51], who compared the fuel consumption of the same vehicle on the same test bench along the NEDC driving cycle and found that different drivers may affect the energy request and therefore the fuel consumption up to 4 %. Additionally, Atzler et al. [52] reported that a difference up to 3.5% in $CO_2$ emissions among measurements on chassis dynamometers with real drivers was found. It is apparent that the simulation which adopts the experimental vehicle speed remarkably reproduces the cumulated end of cycle engine out emissions, but in order to abstract from the test condition, for the following analysis the regulatory vehicle speed will be imposed to the vehicle model.

A detailed analysis on the deviation in terms of emissions along the WLTC driving cycle (including the information about the five most relevant energy weighted key-points) is reported in App.A, in Fig.A.8 and A.8. The five most relevant energy weighted key-points for each combustion mode are reported in Tab.A.1.

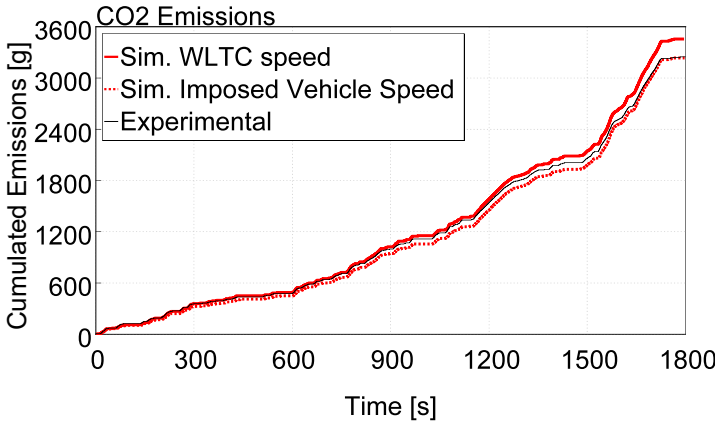


(a) Engine-out carbon dioxide emissions

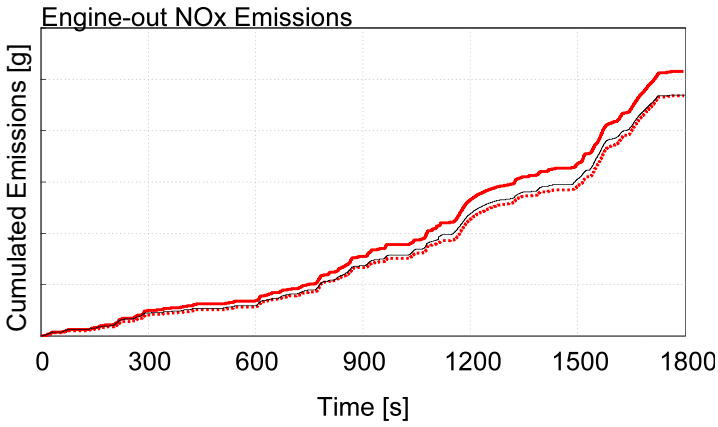


(b) Engine-out nitrogen oxides emissions

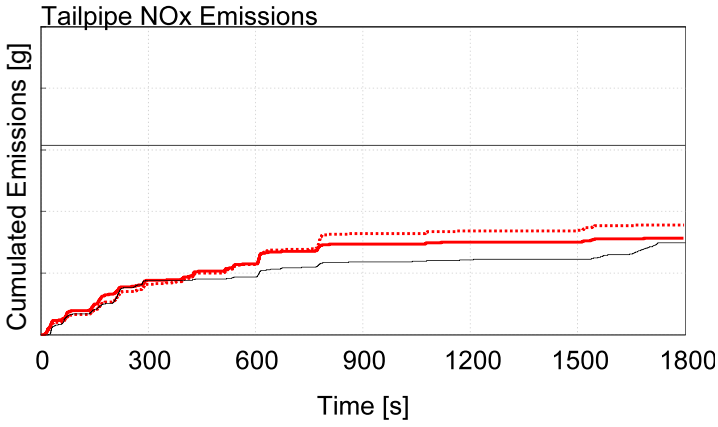


(c) Tailpipe-out nitrogen oxides emissions

Figure 3.22: 12 V Vehicle cumulated emissions - Test A

Table 3.3: Summary of the end of driving cycle carbon dioxide, engine-out and tailpipe nitrogen oxides emissions of the simulated results with respect to the experimental data - Test A

| | **Experiment** | **Sim - Exp. speed** | **Sim - WLTC speed** |
|---|---|---|---|
| Norm. $CO_2$ Emissions | 100% | 99.6% | 106.7% |
| Norm. EO NOx Emissions | 100% | 99.7% | 109.8% |
| Norm. TO NOx Emissions | 100% | 119.9% | 105.3% |

### 3.3.5 48 V vehicle validation

In this paragraph the validation of the 48 V vehicle model is presented. The 48 V MHV features a BSG and a 48 V Li-Ion battery pack, of which the main specification are reported in Tab.2.4 and Tab.2.5. The electric motor is described as 0D model defined on the basis of maximum and minimum torque curves and an efficiency map. Different torque constraints are accounted for depending on the BSG operating mode: when the BSG is used as generator the minimum torque is lower in absolute value than when the BSG is operated in regenerative braking (assuming that in this mode, the BSG is operated for short period of time). The battery is modelled as resistive electrical equivalent circuit battery model defined with an open circuit voltage and an open circuit resistance, which is one of the common battery modelling approaches for EV application [53].

The introduction of a power buffer (the battery pack) and the electric machine has been coupled with the introduction of an on-line Energy Management Strategy (EMS). During the validation activity the 48 V MHV model has been coupled with a black box EMS controller developed by GM-GPS in a co-simulation environment between GT-SUITE and Simulink. This EMS is based on the Equivalent Consumption Minimization Strategy (ECMS) which is an technique which showed to provide an effective solution to the energy management of hybrid vehicle. Moreover, the ECMS is the preferred choice for industrial application for the low requirements in terms of calibration effort with respect to rule based techniques [54]. The ECMS is

> based on the notion that, in charge-sustaining hybrid electric vehicles, the difference between the initial and final state of charge of the battery is very small, negligible with respect to the total energy used. This means that the electrical energy storage system is used only as an energy buffer: ultimately all energy comes from fuel, and the battery can be seen as an auxiliary, reversible fuel tank. Any stored electrical energy used during a battery discharge phase must be replenished at a later stage using fuel from the engine, or through regenerative braking. [...] The principle underlying the ECMS approach is that a cost is assigned to the electrical energy, so that the use of electrical stored energy is made equivalent to using (or saving)

a certain quantity of fuel. [55]

At each instant of time, the ECMS computes the equivalent fuel consumption for different powersplit between thermal engine and electric machine and chooses the powersplit that minimize the equivalent fuel consumption. The computation of the instantaneous equivalent fuel consumption is shown in Eq.3.4, where $\dot{m}_{fuel}$ is the instantaneous fuel flow rate looked-up from steady state maps as function of engine speed and engine torque and $\dot{m}_{rees}$ is the equivalent fuel consumption due the usage of the battery power. This battery power can be converted in equivalent fuel flow rate on the basis of an equivalence factor, defined as $S_0$, which:

> represents the chain of efficiencies through which fuel is transformed into electrical power and vice-versa. As such, it changes for each operating condition of the powertrain. [...] This parameter is representative of past, present, and future efficiency of the engine and the RESS (Author's note: RESS, Rechargeable Energy Storage System), and its value affects both the charge sustainability and the effectiveness of the strategy: if it is too high, an excessive cost is attributed to the use of electrical energy and therefore the full hybridization potential is not realized; if it is too low, the opposite happens and the RESS is depleted too soon (loss of charge sustainability). [55]

$$\dot{m}_{fueleqv} = \dot{m}_{fuel} + \dot{m}_{rees} \tag{3.4}$$

Therefore, by analogy with the engine fuel consumption, the equivalent fuel consumption can be computed as a virtual fuel consumption according to Eq.3.5, where $P_{batt}$ is the instantaneous battery power and $Q_{LHV}$ is the lower heating value of the fuel.

$$\dot{m}_{rees} = S_0 \cdot \frac{P_{batt}}{Q_{LHV}} \tag{3.5}$$

In order to reduce the cycling of the battery and guarantee that the battery SOC does not exceed the admissible limits, a penalty function is used. In the EMS developed by GM-GPS, this penalty function was made proportional to the difference from the actual SOC to a target SOC as presented in Eq.3.6, where $p_{SOC}$ is the proportional term, $SOC(t)$ is the istantaneous SOC and the EMS is aimed to operate the battery at the SOC defined as $SOC_{target}$.

$$S = S_0 + p_{SOC} \cdot f(SOC_{target}) \tag{3.6}$$

The BSG braking torque during regenerative braking events is defined by means of a map based approach and depends on vehicle speed and brake pedal. The Start and

Stop control of the 48 V MHV is updated in such a way that the engine is switched off when the vehicle speed is lower than 23 km/h.

Two experimental tests were available for the validation of the 48 V electric system: in test B the EMS uses a fixed equivalence ratio $S_0$; in test C the equivalence ratio is adapted along the cycle with a non-zero value of $p_{SOC}$.

In Fig.3.23 the comparison of some notable vehicle parameters between experimental data and simulation results of test B is reported. Concerning the Combustion Mode selection depending on the aftertreatment temperature and on the thermal state of the engine, the agreement between experimental data and simulation results is satisfactory. The switch of the vehicle model to Blended combustion mode occurs at 248 s, with the model that delays by 15 s. There is a difference between 300 and 400 s where the vehicle model underestimates the aftertreatment temperature selecting a colder combustion mode but the switch to the Normal combustion mode is correctly phased at 600 s. Similarly, the coolant temperature follows closely the experimental one, in terms of coolant pump switch on, which occurs before 300 s and in the subsequent rise in coolant temperature. Finally, in Fig.3.23c the 48 V battery state of charge is reported. The model reproduces remarkably well the discharge of the battery in the first 300 s (when the warm-up combustion mode is adopted), and the subsequent recharge of the battery after 600 s. The vehicle model overestimates the regenerative braking energy of the vehicle at 1300 s reaching the maximum allowed storage capacity of the battery of 0.7. This may be due to differences in the driver power demand computation between test vehicle and model. At 1500 s the deviation in terms of state of charge is equal to 0.05.

In Fig.3.24, the results of the validation according to test C is reported. Combustion mode selection is reproduced with the correct adoption of the Blended combustion mode at 210 s, at the same time for the vehicle model and the test vehicle. The switch to the normal combustion mode occurs at 300 s (although for less than 40 s). As in Test B, there is a mismatch between experimental and simulation combustion mode selection between 300 and 440 s due to a underestimation of the DOC outlet temperature. This can be explained by the deactivation of the CO oxidation reactions which reduce the exothermic contribution of the DOC reactions. The introduction of a proportional factor for the adaptation of the equivalence factor along the driving cycle, reduces by a great extent the SOC swing to less than 0.1 around a value of 0.5. In test C, the maximum deviation between experimental and simulated SOC is 0.055 at 1745 s.

The validation of the 48 V vehicle model concludes the validation of the vehicle model. The integration of the subsystem in the overall comprehensive vehicle model started from the calibration of the predictive combustion model and the assessment of the predictive capabilities of the combustion model across three different combustion modes. Then, the FRM engine model was validated with the numerical evaluation of the difference in terms of fuel consumption and pollutant emissions on the three combustion modes and during transient TTB operation. After the integration of the cooling circuit and of the aftertreatment system, the 12 V vehicle model showed an excellent agreement in terms of fuel consumption and nitrogen oxides (with deviation equal to

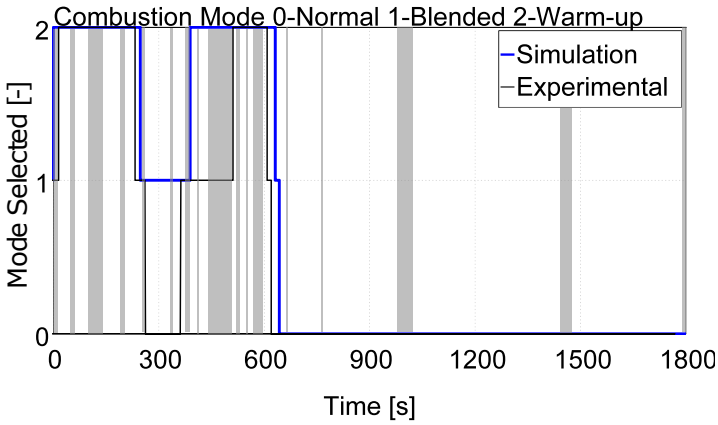


(a) Combustion Mode and Start-Stop on (grey boxes)

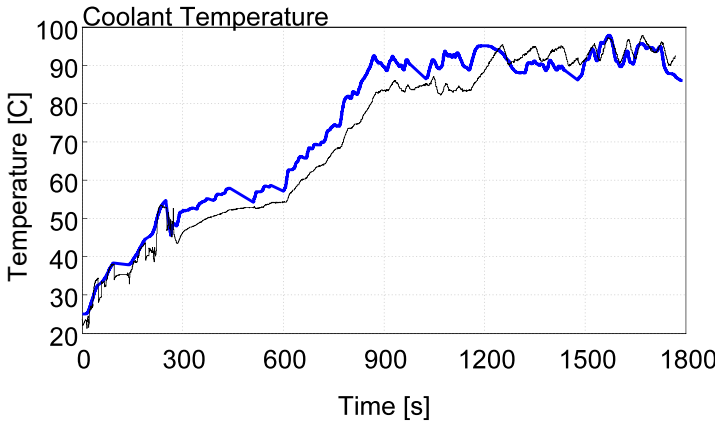


(b) Coolant circuit liquid temperature

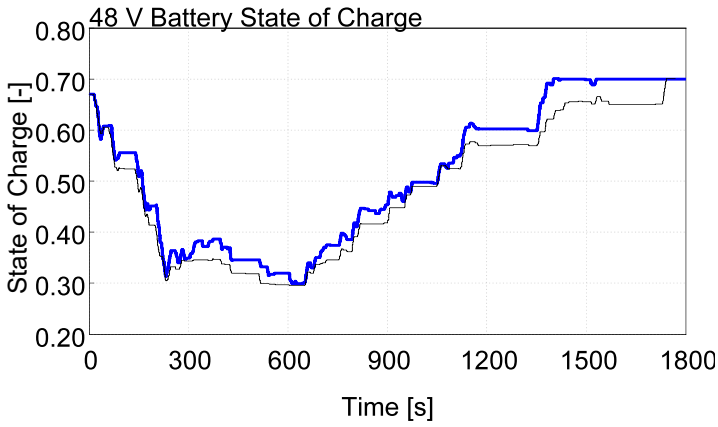


(c) 48 V Battery State of Charge

Figure 3.23: 48 V Vehicle validation - Test B

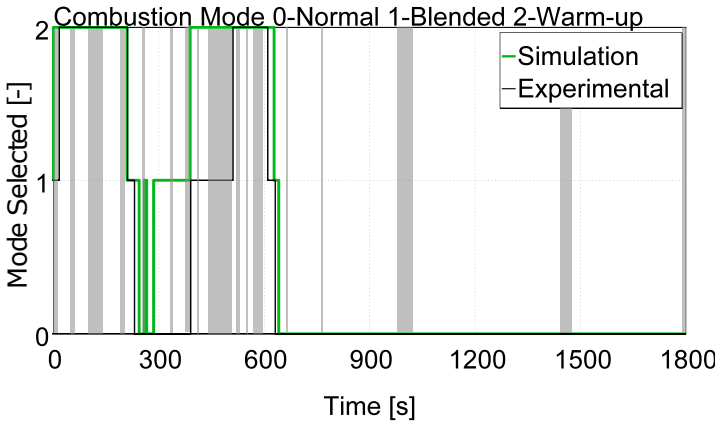


(a) Combustion Mode and Start-Stop on (grey boxes)

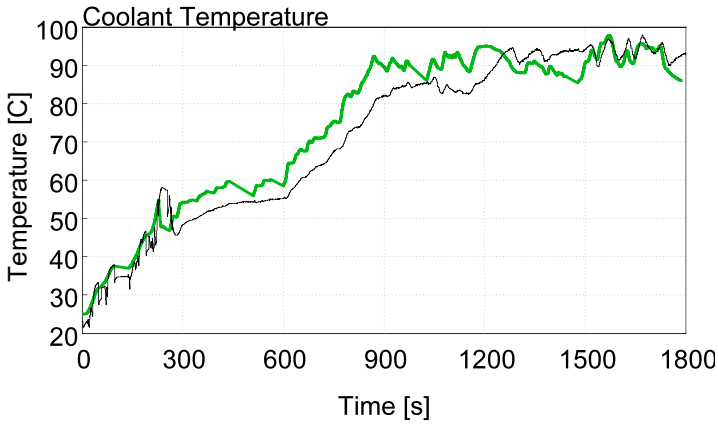


(b) Coolant circuit liquid temperature

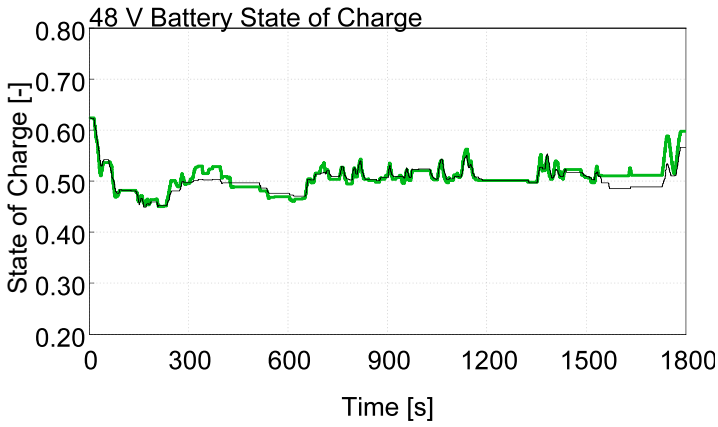


(c) 48 V Battery State of Charge

Figure 3.24: 48 V Vehicle validation - Test C

0.4 % and 0.3 % respectively) when the same vehicle speed was imposed. Finally, using the GM-GPS EMS, the assessment between experimental and simulated combustion mode selection, coolant circuit temperature and 48 V battery state of charge was done, showing a more than satisfactory predictive capabilities of the vehicle model.

# Chapter 4

# Results

In this chapter the comprehensive vehicle model developed in Ch.3 is used as virtual test bench. The predictive capabilities of the model are exploited for a thorough assessment of the 48 V Mild Hybrid Vehicle. First, the evaluation of the trade-off between fuel consumption and nitrogen oxides emissions is done with the aim to identify the optimal calibration of the EMS. Moreover the same analysis is carried out after the integration of the EHC, which was presented in terms of technical characteristics in Ch.2, with the aim to explore the increased flexibility of the powertrain. Additionally, the impact of the eSC (see Ch.2) on transient performance and fuel consumption is assessed. Finally, a novel methodology for the virtual calibration of the main engine calibration parameters and its impact on a driving cycle is reported.

Before the discussion on the EMS, the impact of the extended start and stop is reported. The reference 12 V vehicle and the 48 V MHV previously discussed in Ch.3 differs not only for the electric network, but the 48 V MHV is able to take advantage of the higher power of the electric motor for faster engine start-up. This feature can be exploited increasing the vehicle speed threshold to enable the engine start and stop at speed lower than 23 km/h, from 4 km/h. In order to consistently compare the impact of the electrification on carbon dioxide and nitrogen oxides emissions, two different tests are done to assess the impact of the extended start and stop. In test A, the speed threshold for the activation of the Start and Stop is 4 km/h, while in test B the activation speed is raised to 23 km/h; below these thresholds the engine is switched off. In both tests the BSG is used to start the engine up, while additional hybrid functionalities as torque-assist, load point moving and regenerative braking are disabled. Additionally, the start and stop is enabled when the neutral gear is inserted and since the experimental gearshift of the conventional vehicle is adopted for test A, while test B uses the experimental gearshift of the 48 V MHV, there may be some slight anticipation or delay in the gearshift. In Tab.4.1, the comparison of test A and test B is reported. Concerning carbon dioxide emissions, the extended start and stop reduces the fuel consumption on the WLTC by 1.4 % while the engine-out nitrogen oxides emissions increases by 7.8 %. This result is due to the higher load (and higher nitrogen oxides emissions) at which

the engine is requested to operate after the engine restart to eliminate the error with the speed profile target. However, the tailpipe nitrogen oxides emissions rises by just 2 % thanks to the fact that the SCoR partially compensate the increased nitrogen oxides emissions.

Table 4.1: Summary of the end of driving cycle carbon dioxide, engine-out and tailpipe nitrogen oxides emissions with respect to the experimental data when the Extended Start & Stop is individually evaluated

| | **Test A** | **Test B - 12 V** |
|---|---|---|
| $CO_2$ Emissions | 100% | 98.6% |
| Engine-out NOx Emissions | 100% | 107.8% |
| Tailpipe NOx Emissions | 100% | 102.0% |

## 4.1 Energy and Emission Management Strategy (EEMS)

In this section the Energy and Emission Management Strategy (EEMS) adopted for the analysis is described. The EMS differs from the one used in Ch.3 for the validation of the 48 V mild hybrid vehicle since a Polito EEMS, adapted from other works [25, 56, 57], on the basis of the Equivalent Consumption Minimization Strategy [58] has been adopted for the following analysis in order to leverage the higher flexibility in terms of model integration and tunability of a in-house solution. This EEMS couples a light supervisory control, which defines when the engine has to be switched off (during start and stop operation) and the fuel cut-off, with a modified version of the equivalent consumption minimization strategies. The ECMS approach, which has been explained in Ch.3, computes and minimize instant by instant the equivalent fuel consumption computed as per Eq.3.4. Since nitrogen oxides emissions are a great concern in engines, and this is especially true for diesel powertrain, the idea to shift the optimal control problem from the minimization of fuel consumption to the minimization of pollutant emissions, has been already explored. In particular, Musardo et al. considered the NOx emissions "adding a cost term to the instantaneous equivalent minimization" and adopting a coefficient to weight the relative importance of NOx minimization to the fuel consumption minimization [59], while Sagha et al. [60] introduced an additional penalty function defined on the basis of the engine emissions map. In this work, however, the formulation proposed by Millo et al. [56] have been followed. In analogy with the computation of the instantaneous equivalent fuel consumption shown in Eq.4.1, the instantaneous equivalent nitrogen oxides flow rate is evaluated as in Eq.4.2, where $dotm_{NOx}$ is the instantaneous nitrogen oxides flow rate, $P_{batt}$ is the instantaneous battery power and $Q_{LHV}$ is the lower heating value of the fuel. The term $NEF$ is defined as NOx Flow Rate Equivalent Factor and, according to the approach proposed by Millo et al. [56], is

used to correlate the use of the battery with an equivalent NOx emission rate such as that $NEF = S_0 \cdot EI$, where the Emission Index (EI) correlates NOx emissions to fuel consumption on the basis of the engine brake specific fuel consumption and NOx emissions maps. In the current work, since the BSNOx maps is quite "flat" (see Fig.2.2) due to a marked in-cylinder control of the NOx across the entire engine operating area, a unique average parameter $EI$ across the entire engine operating area has been adopted.

$$\dot{m}_{fueleqv} = \dot{m}_{fuel} + S_0 \cdot \frac{P_{batt}}{Q_{LHV}} \tag{4.1}$$

$$\dot{m}_{NOxeqv} = \dot{m}_{NOx} + NEF \cdot \frac{P_{batt}}{Q_{LHV}} \tag{4.2}$$

In order to manage at the same time the minimization of the fuel consumption and the minimization of NOx emissions, Eq.4.1 and Eq. 4.2 can be combined in a global cost function, Eq.4.3, where $W_{NOx}$ is the weighting factor for the concurrent minimization of carbon dioxide and nitrogen oxides, $\dot{m}_{fueleqv}$ is the equivalent fuel mass flow rate computed according to Eq.4.1, $\dot{m}_{fuelmax}$ is the maximum fuel mass flow rate of the Normal combustion mode, $\dot{m}_{NOxeqv}$ is the equivalent nitrogen oxides mass flow rate computed according to Eq.4.2, $\dot{m}_{NOxmax}$ is the maximum nitrogen oxides mass flow rate of the Normal combustion mode.

The values of fuel flow rate and nitrogen oxides mass flow rate are evaluated instantaneously from steady state maps (one for each combustion mode) as a function of engine speed and total injected quantity.

The combustion mode is required as input for the choice of the experimental map selected for the evaluation of the instantaneous fuel and nitrogen oxides mass flow rate. During the performance tests, the energy management system favours the top performances actuating the engine and the electric motor at the highest rated power taking into account the discharge limits of the battery. This EEMS is developed in Simulink and integrated in the model as a compiled library.

$$J = (1 - W_{NOx}) \cdot \frac{\dot{m}_{fueleqv}}{\dot{m}_{fuelmax}} + W_{NOx} \cdot \frac{\dot{m}_{NOxeqv}}{\dot{m}_{NOxmax}} \tag{4.3}$$

After the integration of the open EEMS in the vehicle model, its behaviour along a WLTC has been compared with that of the black-box EMS provided by ECMS by GM-GPS adopting the calibration of test B, with a calibration aimed to minimize the fuel consumption only. The open EEMS adopted, differently from the EMS by GM-GPS, a slightly lower equivalence factor $S_0$, to guarantee the charge sustaining operation. Moreover the regenerative braking torque of the BSG has been calibrated to guarantee a recovered specific energy comparable to that of the vehicle featuring the EMS by GM-GPS. In Fig.4.1, the comparison in terms of Combustion Mode, coolant temperature and 48 V battery SOC is reported. The selection of the combustion mode of the vehicle with open EEMS follows closely that of the vehicle with the EMS by GM-GPS. Nevertheless,

the Polito EEMS anticipates by 4 s the switch to the Blended combustion mode at 243 s and shows a reversal to the Blended combustion at 668 s for just 5 s. The coolant temperature of the vehicle model equipped with the Polito EEMS is slightly higher than that of the vehicle model equipped with the EMS developed by GM-GPS. This, combined with the behaviour of the Combustion Modes suggests that the engine of the vehicle model which runs with the Polito EEMS is operated at higher load and thus presents higher exhaust temperature and a faster rise of the coolant temperature. The comparison of the SOCs is presented in Fig.4.1c. The battery SOC of the vehicle operated with the open EEMS shows a limited discharge during the first 300 s of the WLTC reaching a SOC of 0.43 while the vehicle with the EMS by GM-GPS reaches a value of SOC equal to 0.31. Between 300 s and 600 s the SOC is mirrored at a distance of, on average, 0.1. After 600 s the SOC of the vehicle featuring the open EEMS rises at a lower rate with respect to that equipped with the EMS by GM-GPS. The same discharge trend is seen at 1150 s but the Polito EEMS exploits in a deeper way the BSG in this phase. After 1400 s the EMS by GM-GPS reaches the controller maximum allowed SOC and stays constant up to the end of the cycle, while the vehicle with open EEMS is able to exploit the electric power at 1500 s and recharge the battery back during the last braking to a SOC which guarantees the charge sustaining operation. However, the behaviour of the Polito EEMS, which controls the battery SOC showing a difference of only 0.1 (i.e. 48 Wh) in the early 600 s and at the end of the cycle, suggests that it can properly used for the following analysis with the advantages of a open and flexible architecture.

## 4.2 Electrically Heated Catalyst (EHC)

Electrically Heated Catalysts (EHC) have been proposed for years since they can improve the catalyst conversion rate by increasing locally the catalyst temperature, with advantages in terms of control flexibility. The engine may, indeed, operate at its highest efficiency while the aftertreatment conversion rate is maintained at the highest efficiency. Several analysis have evaluated the benefits of the EHC: Pfahl et al. [61] investigated the impact of a EHC on a 3-litre Diesel engine placed in different locations along the aftertreatment line or in the SCR. They achieved a reduction of 67 % in terms of nitrogen oxides emissions along the Artemis Urban Cycle. Pautasso et al. [62], investigated the trade-off between fuel consumption and nitrogen oxides tailpipe emissions by means of numerical simulation achieving a reduction of 46 % in terms of tailpipe nitrogen oxides reduction with a fuel penalty of 2.2 % assuming that the electric power needed by the EHC is supplied by the alternator with fixed efficiency.

The current work, instead, aims to investigate the impact of the EHC in the developed comprehensive mild hybrid vehicle model, exploiting the EEMS to concurrently account for tailpipe nitrogen oxides emissions and fuel consumption. In this section the introduction of the electric catalyst (EHC), which was presented in terms of technical characteristics in Ch.2, in the comprehensive vehicle model is reported. The EHC

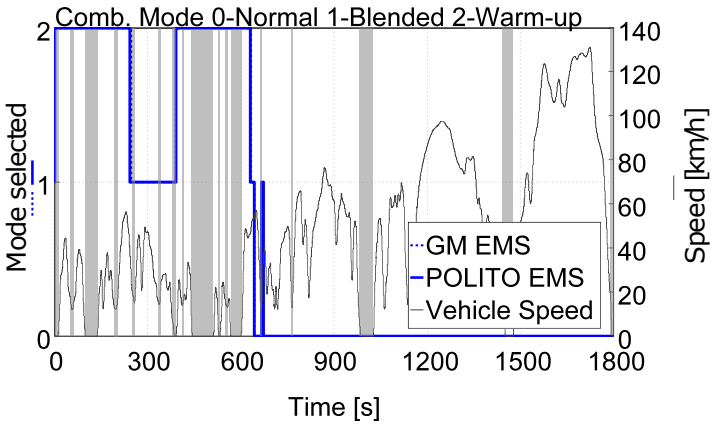


(a) Combustion Mode and Start-Stop on (grey boxes)

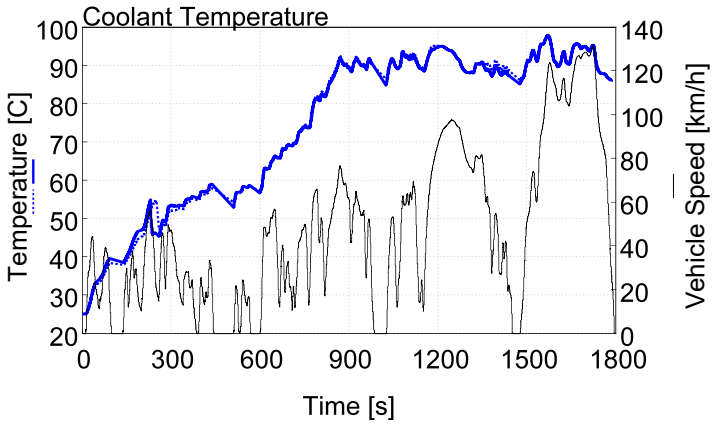


(b) Coolant circuit liquid temperature

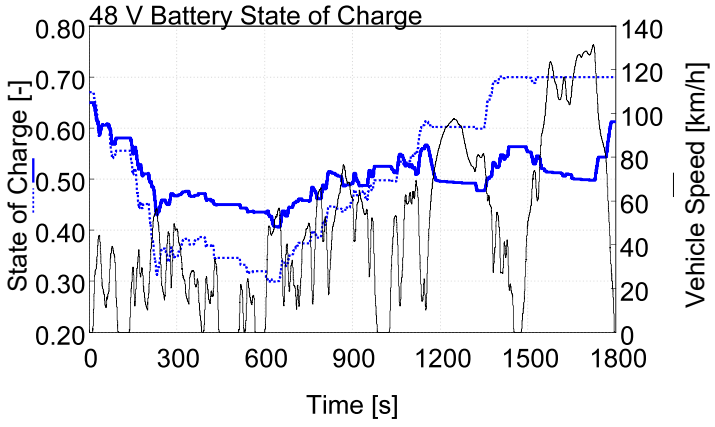


(c) 48 V Battery State of Charge

Figure 4.1: 48 V Vehicle EMS comparision

is modelled as an additional catalyst brick where oxidation reactions can occur. It is placed upstream of the main DOC catalyst and receives, when it is activated, a heat input power to the substrate. The heat distribution is uniform across and along the EHC catalyst brick.

### 4.2.1 EHC Rule Based Controller

A simple rule based controller for the activation and deactivation of the EHC is developed as follows. The EHC is active until the outlet DOC temperature reaches 240 °C, which is a temperature that enables the ammonia injection and promotes efficiently the reduction of nitrogen oxides. To prevent the overheating of the EHC substrate, the EHC is deactivated when the engine is switched off. The EHC reactivates when the engine is switched on and the outlet DOC temperature is below 190 °C, in order to guarantee that the ammonia injection can take place (above 180 °C). When the EHC is activated the thermal power provided to the metallic substrate is equal to 3000 W and goes to zero when it is deactivated. A more refined control strategies, including pulse-width modulation (PWM) technique, combined with an analysis of the DOC outlet target temperature to maximise SCRoF nitrogen oxides conversion efficiency, may be a further development of this work.

## 4.3 48 V Mild Hybrid Vehicle results

In this section the impact of the electrification on vehicle fuel consumption and nitrogen oxides emissions is assessed. The objective is here to show whether it is possible to take advantage of the flexibility of a 48 V MHV to achieve higher performance in terms of vehicle emissions. In order to give a complete overview of the interaction of different EEMS calibration choice and the introduction of the EHC, the results of the conventional vehicle (test A, see Ch.3) are firstly compared with the results of a 48 V MHV with a calibration selected for minimum fuel consumption. The same analysis is carried out after the integration of the EHC with the aim to explore the effect of this component on the trade-off carbon dioxide and nitrogen oxides emissions.

In Fig.4.2 the combustion mode, the coolant temperature and the 48 V battery SOC of the conventional vehicle, the 48 V MHV with a minimum consumption EEMS calibration and the 48 V MHV featuring the EHC along the WLTC are shown. To guarantee that both the 48 V MHV models achieve the charge sustaining operation, the equivalence factor $S_0$ is adjusted from 1.95 to 2.1 in the vehicle with EHC to balance the increased energy demand of this electric auxiliary. The 48 V MHV remains in the Warm-up combustion mode for longer time than the conventional vehicle (243 s, while the conventional switches to the Blended combustion mode at 66 s) and switches finally to the Normal combustion mode at 671 s. On the contrary, the vehicle with EHC adopts the Blended combustion mode at 75 s (just 11 s after the conventional vehicle), and the

Normal combustion at 85 s. With the EHC, the final transition to Normal combustion occurs at 610 s, 20 s before that of the conventional vehicle. Concerning the coolant temperature, the hybrid vehicles show a lower temperature up to 900 s. As an example, at 500 s, the conventional vehicle has a coolant temperature of 60 °C, while the hybrid vehicle with EHC reaches a coolant temperature 5 °C lower and the MHV of just 53 °C. The temperature of 70 °C is reached at 644 s by the conventional vehicle, at 690 s by the MHV with EHC and only at 723 s by the MHV. Concerning the 48 V battery state of charge, in the early phases of the cycle (early 150 s), the MHV with EHC shows a higher discharge rate caused by the activation of the electric catalyst. This component affects the battery discharge rate also before 600 s, where the low vehicle speed target reduces the engine load and allows the engine to be switched off thanks to the extended start and stop.

Fig.4.3 presents the early 300 s of the cycle which are considered representative of the aftertreatment light-off in terms of BSG brake torque, DOC outlet temperature and activation of the EHC and injected ammonia. The explanation of the different EEMS strategy between MHV with and without EHC may be found in Fig.4.3a. In order to guarantee charge sustaining operation, the BSG of the MHV with EHC operates less frequently to assist the engine during the acceleration phases (this is apparent between 120 s and 240 s). Concerning the DOC outlet temperature, the MHV vehicle shows a lower temperature along the first 300 s, as high as 110 °C at 75 s (where the conventional vehicle DOC outlet temperature achieves 240 °C. At the same time, the activation of the EHC allows to increase the DOC outlet temperature up to 210 °C. The EHC greatly enhance the DOC temperature after 120 s up to 284 °C while the DOC outlet temperature of the MHV stays below 160 °C. This difference in terms of DOC outlet temperature affects the injection of the ammonia and the efficient activation of the SCR reduction reactions. Indeed, the MHV shows no ammonia injection up to 240 s while the ammonia injection on conventional vehicle and MHV with EHC starts at around 60 s.

Finally, in Fig.4.4, the cumulated carbon dioxide, engine-out and tailpipe nitrogen oxides emissions along the driving cycle are reported. Both MHVs achieve lower cumulated carbon dioxide emissions along and at the end of the driving cycle. The vehicle with EHC has a higher fuel consumption than the vehicle without EHC, because the energy recovered by the regenerative braking may not fully be used to assist the thermal engine and the engine of the vehicle with EHC is operated at higher load to recharge the battery. Moving to engine-out nitrogen oxides emissions, the 48 V MHV without EHC shows the lowest emissions, due to the fact that the EEMS uses the BSG to assist the engine. On the contrary, the need to recharge the battery given the activation of the EHC pushes the engine-out nitrogen oxides emissions above those of the conventional vehicle. Nevertheless, the advantage of the EHC is apparent when tailpipe nitrogen oxides emissions are concerned. Indeed, the MHV with EHC shows the lower cumulated nitrogen oxides emissions thanks to a higher SCR efficiency and the possibility to anticipate the ammonia injection earlier during the driving cycle. The MHV without EHC achieves higher tailpipe nitrogen oxides emissions (but still below the legal limit)

because the temperature of the exhaust aftertreatment are lower hence reducing the reduction reaction rates.

In Fig.4.5 the combustion mode, the coolant temperature and the 48 V battery SOC of the 48 V MHV with the EEMS calibration aimed to reduce nitrogen oxides emissions and the 48 V MHV featuring the EHC along the WLTC are reported. Simulation results of the conventional vehicle are added as reference. The two 48 V MHV models achieve the charge sustaining operation, hence the nitrogen oxides equivalence factor $NEF$ is adjusted in the vehicle with EHC to balance the increased energy demand of this electric auxiliary. Differently from the MHV with the EEMS calibrated for minimum fuel consumption (see Fig.4.2), both the 48 V MHVs switch earlier to the Blended combustion mode: the vehicle without EHC at 77 s and the vehicle with EHC at 67 s. Both hybrid vehicles finally adopt the Normal combustion mode before the conventional vehicle (at 608 s the MHV with EHC and at 620 s the vehicle without EHC). Concerning the coolant temperature, the hybrid vehicles calibrated for minimum nitrogen oxides emissions follow closely the coolant temperature of the conventional vehicle. As an example, at 500 s, the conventional vehicle has a coolant temperature of 60 °C, while the hybrid vehicle with EHC reaches a coolant temperature 3 °C lower and the MHV of 55 °C. The temperature of 70 °C is reached at 647 s by the MHV with EHC (just 3 s after the conventional vehicle and at 691 s by the MHV (32 s before the MHV adopting the calibration that minimize the fuel consumption). Concerning the 48 V battery state of charge, differently by the MHV aimed at minimizing the carbon dioxide emissions, here, in the first half of the cycle (up to 150 s), the MHV without EHC recharges the battery up to 0.75, while the MHV with EHC keep the SOC flat in spite of the activation of the electric catalyst. This behaviour is explained by the fact that in the first half of the cycle, the adoption of Warm-up and Blended calibration, with lower nitrogen oxides emissions with respect to the Normal combustion mode, and the low traction power required by the vehicle, favours the load point moving. After 1200 s, the EEMS chooses to act to reduce the load on the engine exploiting the energy available in the battery.

Fig.4.6 presents the early 300 s of the cycle which are considered representative of the aftertreatment light-off in terms of BSG brake torque, DOC outlet temperature and activation of the EHC and injected ammonia. The explanation of the different EEMS strategy between MHV with and without EHC may be found in Fig.4.3a. Differently from the case where the EEMS was calibrated for the minimum fuel consumption, in this case the EEMS take advantage of the lower nitrogen oxides emissions at low load using the colder combustion modes and the BSG is operated at negative torque to recharge the battery. In terms of BSG operation, the MHV with EHC, with respect to the vehicle without EHC, reduces the torque assist operation (e.g. at 210 s) and increases the load point moving operation (e.g. at 180 s). Concerning the DOC outlet temperature, the MHV vehicle shows a comparable temperature along the first 300 s, as high as 200 °C at 75 s (90 °C higher than the case where fuel consumption was the priority). At the same time, along the WLTC, the activation of the EHC allows to increase the DOC outlet temperature up to 270 °C (60 °C higher than the vehicle with the EEMS calibrated

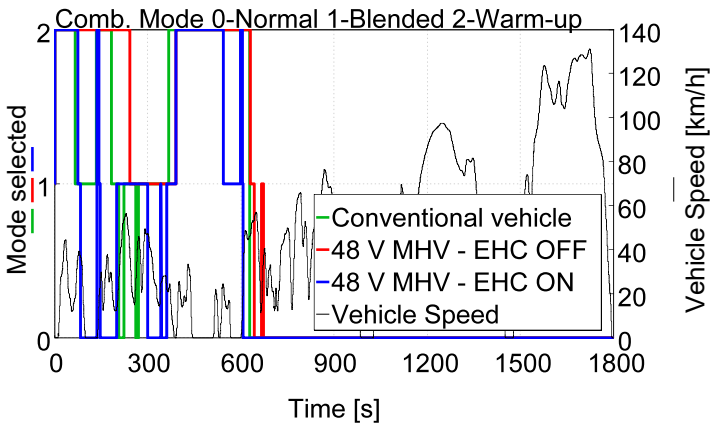


(a) Combustion Mode selection

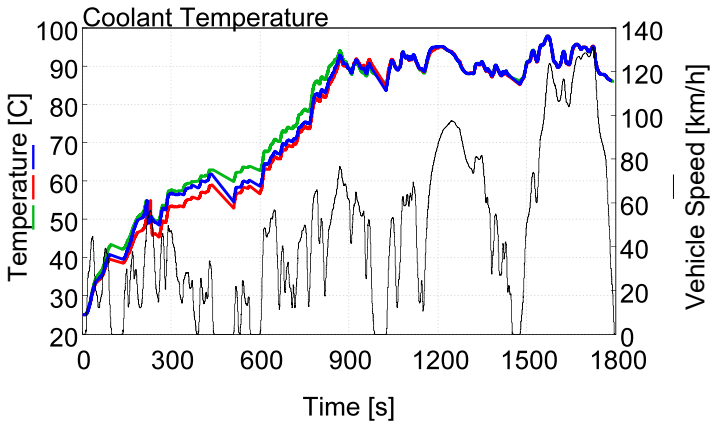


(b) Coolant circuit liquid Temperature

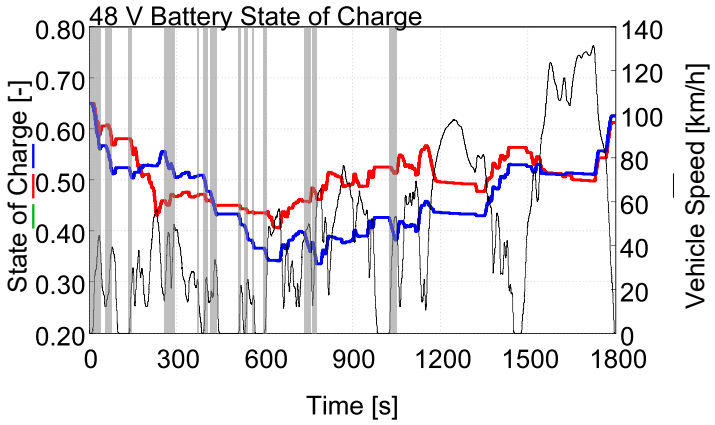


(c) 48 V Battery SOC and EHC ON (grey boxes)

Figure 4.2: MHV with and without EHC along the WLTC driving cycle - EEMS calibrated for minimum $CO_2$ emissions

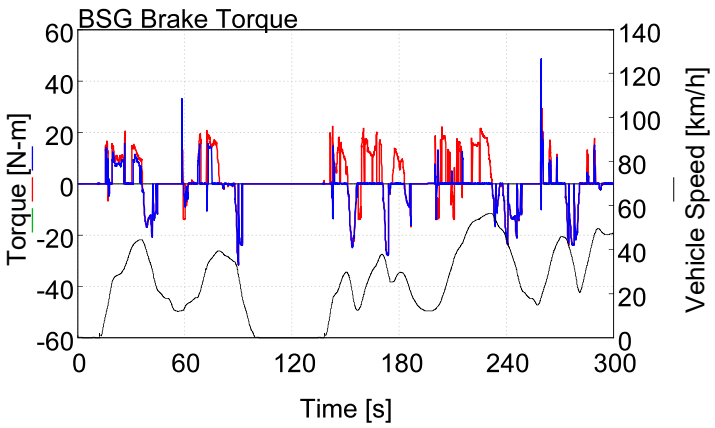


(a) BSG Brake Torque

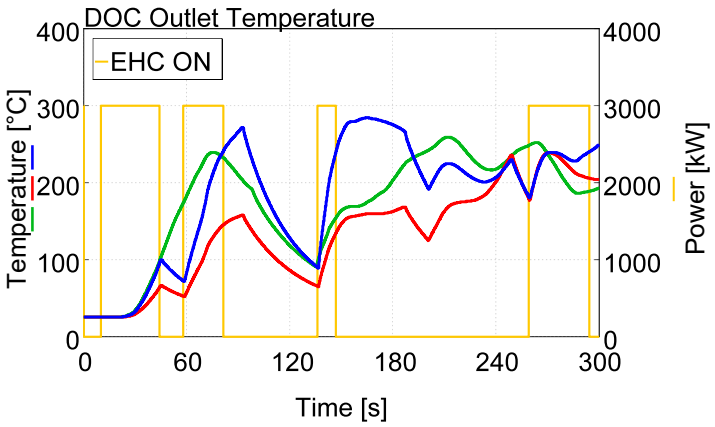


(b) DOC light-off

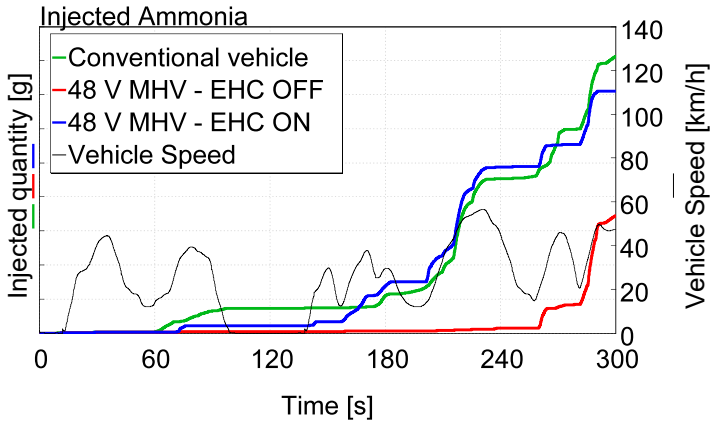


(c) Injected ammonia

Figure 4.3: MHV with and without EHC along the WLTC driving cycle - EEMS calibrated for minimum $CO_2$ emissions - Focus on light-off

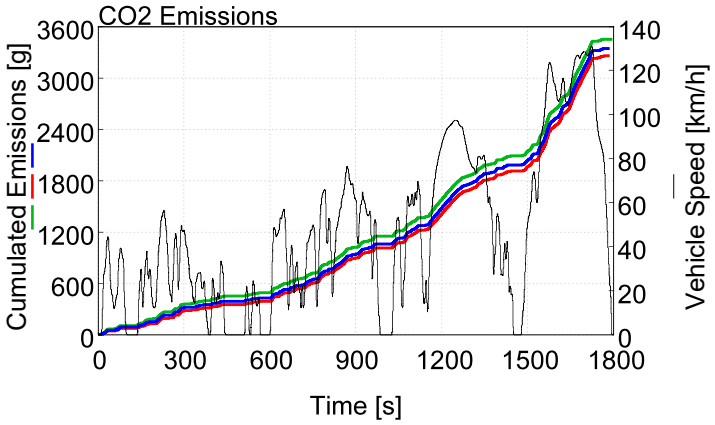


(a) $CO_2$ Emissions

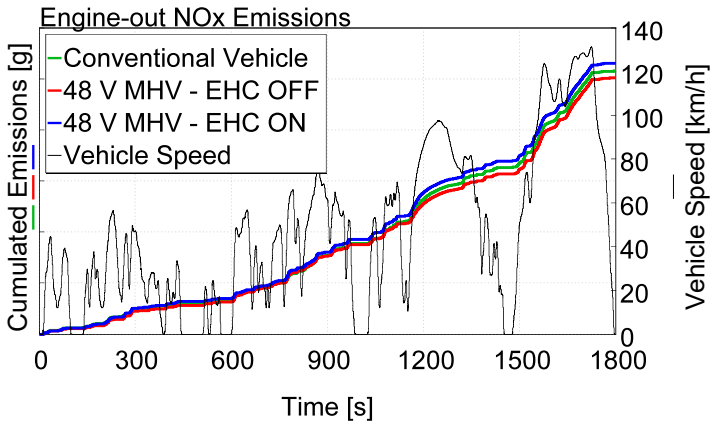


(b) Engine-out NOx Emissions

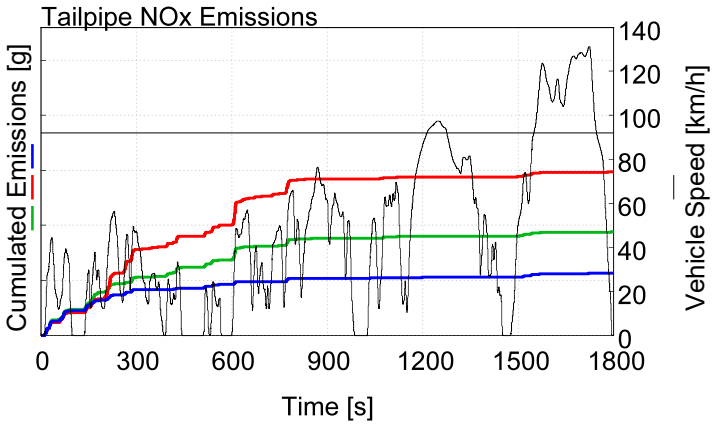


(c) Tailpipe NOx Emissions

Figure 4.4: MHV with and without EHC along the WLTC driving cycle - EEMS calibrated for minimum $CO_2$ emissions - Emissions

for minimum fuel consumption). The EHC greatly enhance the DOC temperature after 120 s up to 310 °C while the DOC outlet temperature of the MHV stays below 238 °C. The MHV starts the ammonia injection at the same time as the conventional vehicle and the MHV with EHC starts at around 60 s.

Finally, in Fig.4.7, the cumulated carbon dioxide, engine-out and tailpipe nitrogen oxides emissions along the driving cycle are reported. The MHVs without EHC achieves lower cumulated carbon dioxide emissions along and at the end of the driving cycle while, in this case, the vehicle with EHC shows comparable carbon dioxide emissions as the conventional vehicle. Moving to engine-out nitrogen oxides emissions, the 48 V MHV without EHC shows the lower emissions, similarly as the case where the EEMS was aimed to lower fuel consumption. Also the vehicle with EHC shows lower engine-out nitrogen oxides emissions than the conventional vehicle. As for the previous case, the advantage of the EHC is apparent when tailpipe nitrogen oxides emissions are concerned. Indeed, the MHV with EHC shows the lower cumulated nitrogen oxides emissions thanks to a higher SCR efficiency. In this case also the MHV without EHC is able to achieve lower tailpipe nitrogen oxides emissions because the temperature of the exhaust aftrtreatment are similar to that of the conventional vehicle but the engine out nitrogen oxides emissions are lower.

### 4.3.1 EEMS Calibration summary

A summary of the trade-off between carbon dioxide with respect to engine out and tailpipe out nitrogen oxides emissions is shown in Fig.4.8. Although all the simulations are operated in charge sustaining, the results in terms of carbon dioxide are corrected to account for even the smallest difference in terms of added or depleted energy in the battery. The correction assumes that, for limited deviation of the battery energy (below 0.5 % of the fuel energy consumed along the cycle), the equivalence factor $S_0$ represent a reliable estimation of the electric energy to fuel conversion and the relation of Eq.4.1 has been used. No correction has been adopted for tailpipe nitrogen oxides emissions given the not negligible impact of secondary effects (the DOC outlet temperature and the ammonia injection). The analysis is done varying the parameter $W_{NOx}$ from a value of zero, representative of a EEMS prioritizing the optimization of the fuel consumption (see Fig.4.4) to a value of one to operate the EEMS towards the reduction of the nitrogen oxides (see Fig.4.7). These charts give evidence of the beneficial impact that electrification has on the reduction of the tailpipe emissions. The improvement in terms of fuel consumption ranges from a minimum of - 6.5 % to - 3.6 % with respect to the conventional vehicle, when the MHV without EHC is considered. This advantage comes with a reduction of the engine-out nitrogen oxides emissions which range between - 1.3 % in the MHV with the EEMS calibrated with minimum fuel consumption ($W_{NOx}$ equal to zero) and - 17.5 % when the focus is on the reduction of the nitrogen oxides emissions. This results can be compared to the ones obtained in [63], where the test case used for this thesis has been equipped with a 48 V BSG and experimentally tested. In

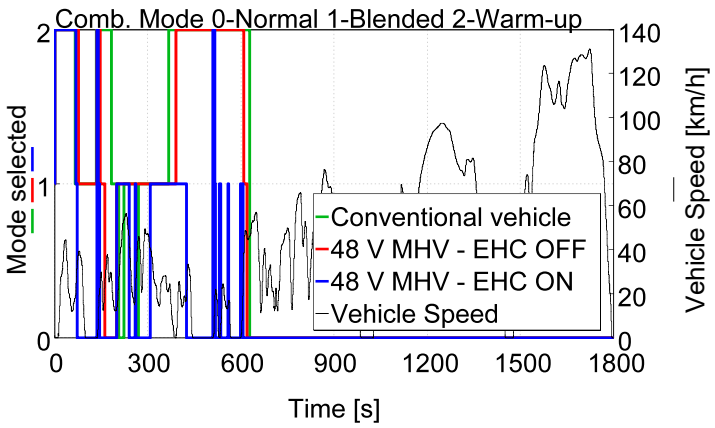


(a) Combustion Mode selection

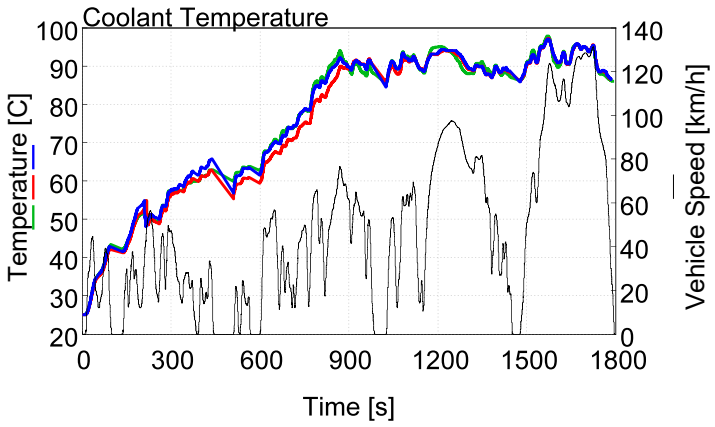


(b) Coolant circuit liquid Temperature

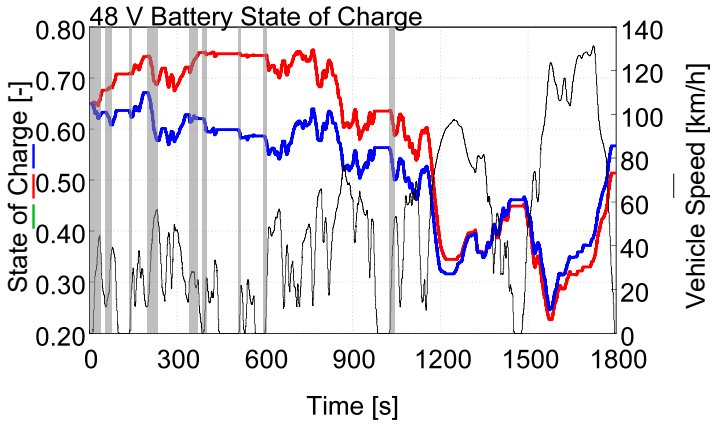


(c) 48 V Battery SOC and EHC ON (grey boxes)

Figure 4.5: MHV with and without EHC along the WLTC driving cycle - EEMS calibrated for minimum NOx emissions

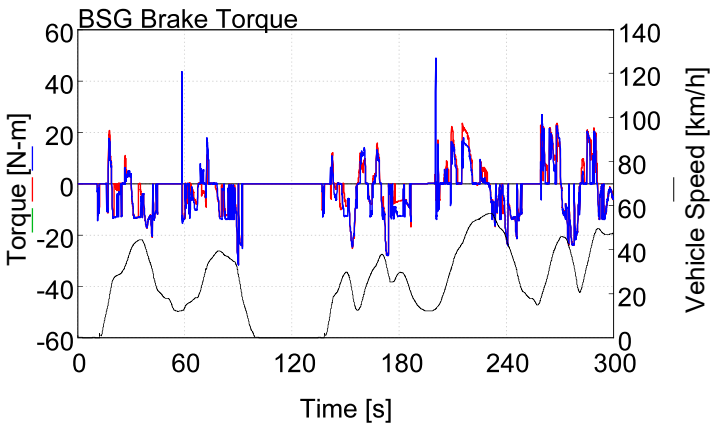


(a) BSG Brake Torque

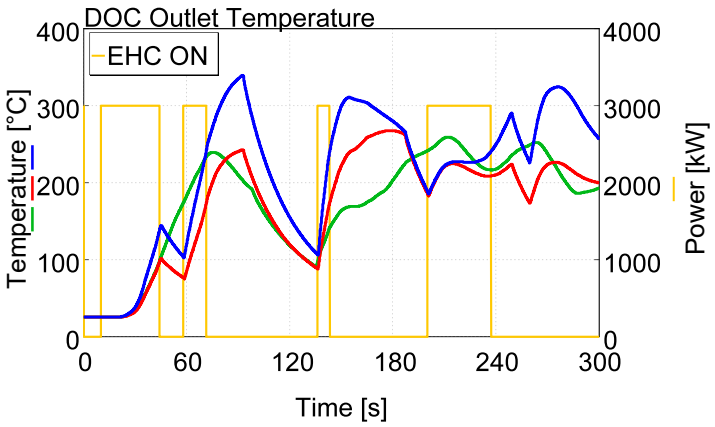


(b) DOC light-off

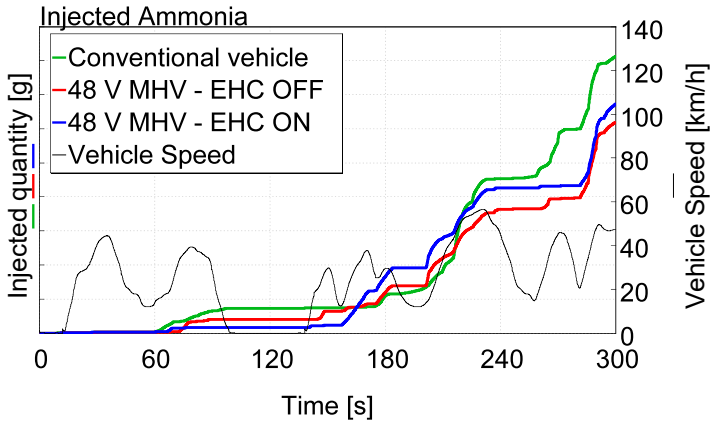


(c) Injected ammonia

Figure 4.6: MHV with and without EHC along the WLTC driving cycle - EEMS calibrated for minimum NOx emissions - Focus on light-off

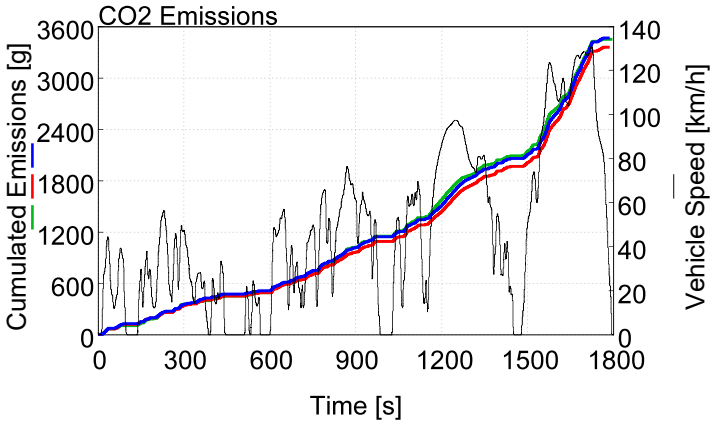


(a) $CO_2$ Emissions

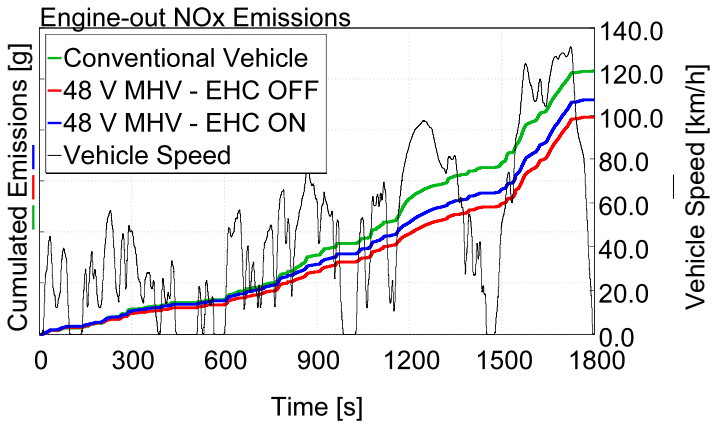


(b) Engine-out NOx Emissions

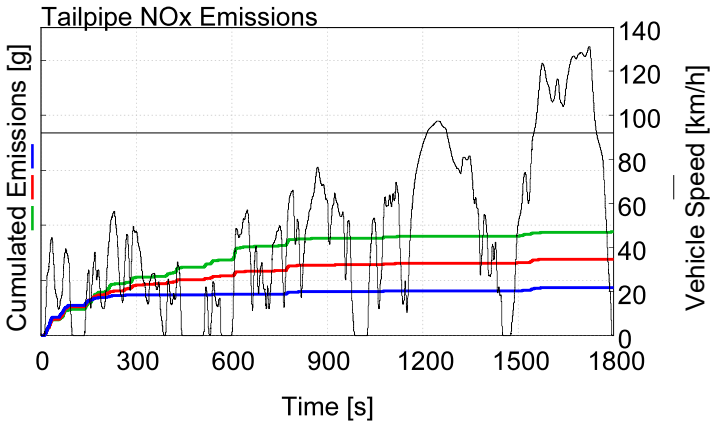


(c) Tailpipe NOx Emissions

Figure 4.7: MHV with and without EHC along the WLTC driving cycle - EEMS calibrated for minimum NOx emissions - Emissions

that experimental analysis, a - 4.8 % reduction in terms of carbon dioxides emissions and engine out nitrogen oxides emissions decrease by 22 % were obtained. While the fuel consumption improvement falls in the range achieved by the comprehensive vehicle model developed in this work, the nitrogen oxides reduction is experimentally higher. This may be explained recollecting the outcomes of Tab.3.3, where the comparison among the experimental results in terms of fuel consumption and nitrogen oxides emissions and the simulation results of a vehicle following the experimental speed trace and the regulated WLTC speed were summarised. In that table, the impact of a different vehicle speed profile brought to a difference of 6.7 % in terms of fuel consumption and almost 10 % in terms of nitrogen oxides production. It is reasonable to assume that the driver aggressiveness has an significant impact in the the underestimation of the advantage in terms of nitrogen oxides emissions reduction.

To guarantee the highest advantage in terms of fuel consumption, and tailpipe emissions lower than that of the conventional vehicle, the EEMS was calibrated with a value of $W_{NOx}$ equal to 0.6. In this case, the MHV emits the 94 % of the carbon dioxide emissions and the 84 % of the engine-out nitrogen oxides emissions, while the tailpipe nitrogen oxides emissions are equal to the 88.4 %. These result of the MHV vehicle with and without EHC adopting a $W_{NOx}$ equal to 0.6, are summarized in Tab.4.2. In [63] the 48 V benefit is claimed to result in a reduction of the tailpipe nitrogen oxides emissions around −15 % similarly to the reduction achieved in this work. Concerning the MHV featuring the EHC, the trade-off carbon dioxide and engine-out nitrogen oxides moves closer to the conventional vehicle since this vehicle has higher engine-out emissions with respect to the MHV vehicle without EHC. In particular the carbon dioxide ranges from - 4.2 % when the EEMS is calibrated for minimum fuel consumption (combined with an increase of + 3% of EO nitrogen oxides emissions) to just - 0.6 % (with a reduction of - 12.3 % of EO nitrogen oxides emissions). Moving to the trade-off between carbon dioxide and tailpipe nitrogen oxides, the impact of electrification on emissions is remarkably different. Actually, the advantage of fuel consumption reduction for the MHV without EHC is counterbalanced by an increase of tailpipe nitrogen oxides emissions up to 58 % due to lower exhaust temperature. On the other hand, the flexibility of the electrification allows that, when the EEMS is focused at minimum nitrogen oxides emissions, the tailpipe emissions reduces as well up to - 26 %. Moreover, the introduction of the EHC has an impressive impact in reducing the tailpipe emissions with respect to the conventional vehicle in a range of - 40 % to - 54 % depending on the EEMS calibration at the expenses of an increase of the fuel consumption. Adopting a $W_{NOx}$ equal to 0.6, the reduction in terms of tailpipe nitrogen oxides emissions is equal to 52.9 %. This seems to overestimate the advantage of the EHC analysed experimentally in [63], where a reduction of tailpipe nitrogen oxides by 28.6 % was stated. It is to be pointed out, however, that a rule based control logic different from the one adopted in this work may have been followed (e.g. different DOC outlet temperature for the deactivation of the EHC) which may affect the overall result. The impact of different set-point temperatures, used to control the switch to warm combustion modes and for the activation of

the EHC, has been extensively reported in [64] for a 48 V Diesel hybrid architecture by means of numerical simulation. In this paper, depending on the set-point temperature, the tailpipe nitrogen oxides emission levels ranges from 10 mg km$^{-1}$ to 100 mg km$^{-1}$ and from 125 g km$^{-1}$ to 160 g km$^{-1}$ when the carbon dioxide emissions are concerned. Although no clear indication of the impact on nitrogen oxides emissions for the same set-point temperature after the introduction of the EHC is given, an increase of the fuel consumption by 2 % is claimed. In the present work, considering the calibration with $W_{NOx}$ equal to 0.6, the impact of the EHC on the fuel consumption is detrimental and equal to an increase of the carbon dioxide emissions by 2.7 %. Also, the MHV without EHC calibrated for minimum nitrogen oxides achieves slightly higher fuel consumption than the MHV with EHC with the EEMS aimed to reduce fuel consumption.

Therefore, the electrification showed a positive impact in terms of nitrogen oxides and carbon dioxide emissions reduction with the possibility to tune the EEMS response to the optimal trade-off given the case study and overall vehicle design targets. Moreover, the introduction of the EHC, while worsening the fuel consumption of the MHV vehicle allows to achieve unprecedented nitrogen oxides emission reduction.

Table 4.2: Impact of hybridization and introduction of an Electrically Heated Catalyst on the WLTC driving cycle

| | **BASE** | **MHV** | **MHV + EHC** |
|---|---|---|---|
| Norm. Corrected CO2 | 100% | 93.9% | 96.6% |
| Norm. EO NOx emissions | 100% | 83.9% | 92.9% |
| Norm. TO NOx emissions | 100% | 88.4% | 47.1% |

### 4.3.2 Phlegmatization

Researchers have proposed that reducing the load gradients on the engine, the so-called phlegmatization, made possible thanks to the electrification, can be a viable way to achieve lowest emissions and fuel consumption in diesel powertrains [52, 65–67]. In this paragraph the impact of the adoption of the EEMS for the concurrent reduction of carbon dioxide and nitrogen oxides emissions on engine load and emissions is analysed. Fig.4.9 reports engine brake torque and EO nitrogen oxides emissions of the conventional vehicle and of the MHV with the EEMS targeted for minimum fuel consumption or minimum nitrogen oxides emissions. Looking at this plot, while the vehicle featuring the EEMS for minimum fuel consumption reduces the engine brake torque when high load is requested to the powertrain, the vehicle aimed at reducing nitrogen oxides emissions makes the engine operate with smaller load gradients. As it is noticeable, when higher load is requested to the conventional engine (e.g. 1330 and 1430 s), the EEMS for minimum NOx emissions reduces the engine peak torque smoothening the power request to the engine. Moreover, when the load request to the vehicle is low, the EEMS

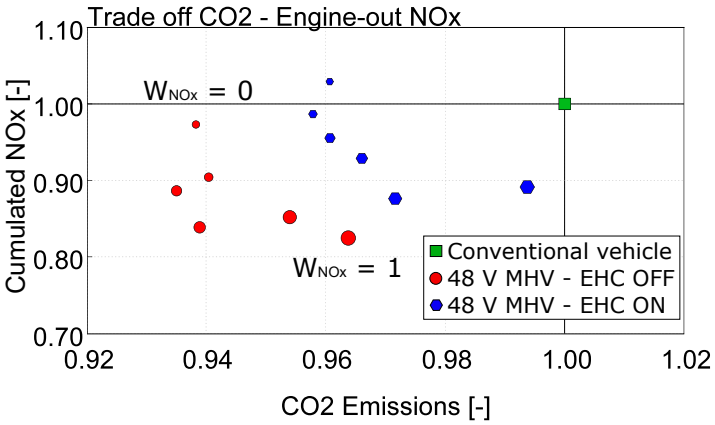


(a) $CO_2$ - EO NOx

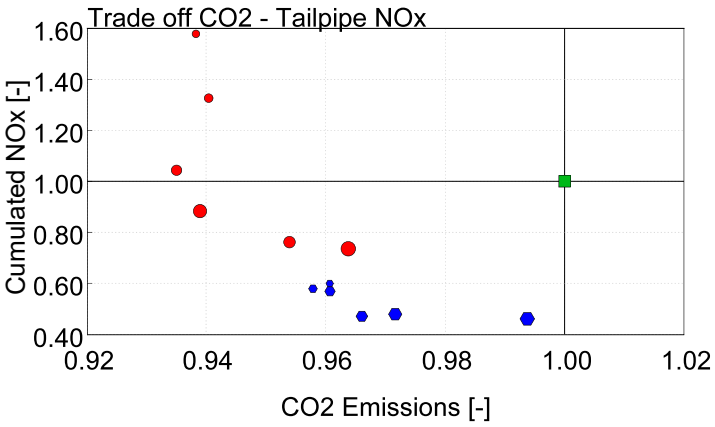


(b) $CO_2$ - TO NOx

Figure 4.8: 48 V Mild Hybrid Vehicle EEMS calibration

maintains a non-negligible load request: the engine load gradient is smoothed, and the battery is recharged. The reduction of engine load gradients remarkably lowers the EO nitrogen oxide mass flow rate along the driving cycle. This engine management is similar to the one proposed by Auerbach et al. [66], where the phlegmatization showed advantages in terms of nitrogen oxides emissions and soot formation. In the present study, the impact of the EEMS on soot emissions has not been investigated for the lack of a quantitative reliable soot model, but it may be an interesting future development of this work.

### 4.3.3 Additional results on type approval and RDE driving cycles

In this section, the emissions of the conventional vehicle and of the MHVs are analysed along different type approval and RDE driving cycle, the RTS-95, the FTP-75 and

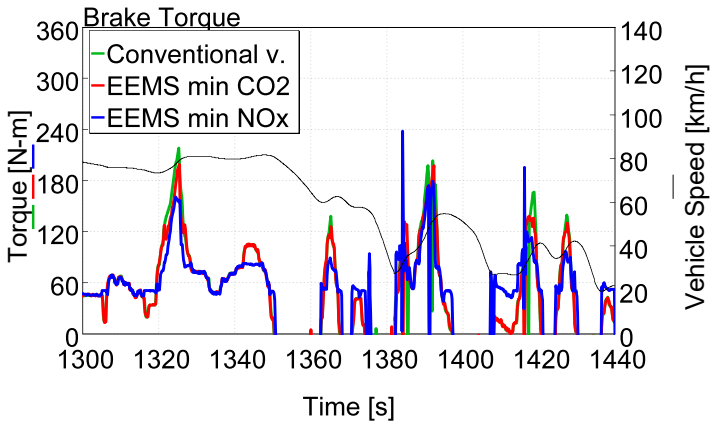


(a) Engine Brake Torque

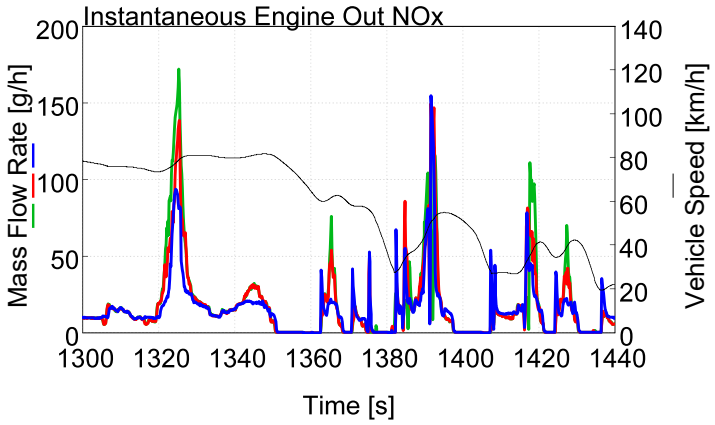


(b) Instantaneous NOx emissions

Figure 4.9: Phlegmatization effect of the EEMS on a snippet of the WLTC

the US06 in order to evaluate the benefit of the electrification, in terms of emissions, on different driving conditions. Also these analyses include the cold start. The calibration chosen for these analyses of the MHVs along the additional type approval and RDE driving cycles is the one that guarantees, on the WLTC, the lowest fuel consumption with tailpipe nitrogen oxides emissions slightly lower than the conventional vehicle. This corresponds to a $W_{NOx}$ equal to 0.6 which is kept the same for the MHV with and without EHC.

As a preliminary analysis, in Tab.4.3 the ”driving cycle effect” in terms of corrected carbon dioxide emissions, engine out and tailpipe nitrogen oxides emissions is reported for the conventional vehicle. The results are normalized on the basis of the WLTC driving cycle. The driving cycle where the conventional vehicle emits more than + 30 % of carbon dioxide is the RTS-95, while the FTP-75 shows the lower emissions equal to 83.3 % with respect to the WLTC. The US06 presents a slight fuel consumption increase with

respect to the WLTC with a + 4.8 %. The RTS-95 which is a very aggressive cycle shows an increase of the engine-out nitrogen oxides emissions with respect to the WLTC by 55.6 %, while FTP-75 and US06 have slightly lower emissions (- 4.3 % and - 1.7 %, respectively). Tailpipe nitrogen oxides emissions depends, in addition to the engine-out emissions, also to the thermal state of the aftertreatment which affects the ammonia injection and thus the SCR reduction efficiency. Due to the shorter duration of the cycle, along RTS-95 (which lasts 900 s, half of the WLTC duration) and US06 (which lasts only 600 s), the time required for the light-off of the aftertreatment has an impact on the tailpipe emissions which is more significant on this driving cycles than that on the WLTC. Indeed, the tailpipe emissions on RTS-95 increases by 106.2 % and on US06 by 134.8 %. On FTP-75 the increase in terms of tailpipe nitrogen oxides emissions by + 89 % is due to the fact the the DOC outlet temperature stays for the majority of the time around 180 °C, due to the relatively low vehicle speed of the cycle and to the low load on the engine, hindering the ammonia injection and the efficient reduction of the nitrogen oxides in the SCR.

Table 4.3: Comparison among different driving cycles of the emissions of the conventional vehicle

| | **WLTC** | **RTS-95** | **FTP-75** | **US06** |
|---|---|---|---|---|
| Norm. Corrected $CO_2$ | 100% | 130.9% | 83.3% | 104.8% |
| Norm. EO NOx emissions | 100% | 155.6% | 95.7% | 98.3% |
| Norm. TO NOx emissions | 100% | 206.2% | 189.0% | 234.8% |

In Fig.4.4, the comparison of the different specific energy usage (the ratio between BSG energy in a defined hybrid mode and cycle distance) of the 48 V MHV with respect to the WLTC is presented. The steeper deceleration of the RTS-95 with respect to the WLTC is recollected by the regenerative braking, increasing the specific energy recovered by the BSG by 14.2 %. On FTP-75 the regenerative braking contributes as much as on the WLTC (just - 0.2 %), while the US06 shows the smaller specific regenerative energy among the four driving cycles since this cycle is characterized by few deceleration events, even if its negative acceleration is only smaller than the RTS-95 (see Tab.2.8. Similarly, the US06 shows few acceleration events which reduce the specific energy used to assist the engine to just 58.1 % of the WLTC and the specific energy devoted to the load point moving is just less than one sixth of that along the WLTC. The load point moving is exploited significantly more on the FTP-75 than on the WLTC (more than five times as much).

After the short summary about the main differences in terms of BSG usage along the driving cycle, in Tab.4.5 the emissions of the conventional vehicle, the MHV and the MHV with EHC on the RTS-95 are summarized. The hybridization improves the fuel consumption by 8.4 %, the engine-out nitrogen oxides emissions reduces by 21.8 % and the tailpipe emissions decreases by 7.3 %. With the same EEMS calibration and adopting

Table 4.4: Comparison among different driving cycles of the specific BSG energy usage of the Mild Hybrid Vehicle

| | **WLTC** | **RTS-95** | **FTP-75** | **US06** |
|---|---|---|---|---|
| Regenerative Braking | 100% | 114.2% | 99.8% | 59.0% |
| Torque Assist | 100% | 123.6% | 104.8% | 58.1% |
| Load Point Moving | 100% | 73.2% | 566.9% | 16.2% |

the EHC rule based control strategy discussed in Sec.4.2.1, the introduction of the EHC shows an increased fuel consumption with respect to the MHV with an improvement of just 6.5 % with respect to the conventional vehicle. Also, the engine-out nitrogen oxides emissions increases, with respect to the MHV, to 80.6 % of the emissions produced by the conventional vehicle. On the other hand the introduction of the EHC reduces the tailpipe nitrogen oxides emission by 22.8 % with respect to the conventional vehicle, reducing by additional 15.5 % the emissions of the MHV.

Table 4.5: Impact of hybridization and introduction of an Electrically Heated Catalyst on the RTS-95 driving cycle

| | **BASE** | **MHV** | **MHV + EHC** |
|---|---|---|---|
| Norm. Corrected $CO_2$ | 100% | 91.6% | 93.5% |
| Norm. EO NOx emissions | 100% | 78.2% | 80.6% |
| Norm. TO NOx emissions | 100% | 92.7% | 77.2% |

Along the FTP-75, see Tab.4.6, the electrification shows promising results in terms of carbon dioxide emissions (- 9 %) as well as on tailpipe nitrogen oxides emissions (- 29.7 %), while the introduction of the EHC reduces the advantage in terms of fuel consumption to just 0.5 % but has a remarkable impact on the reduction of the tailpipe nitrogen oxides emissions (- 56.4 %). This is due to the fact that the EHC contributes to the increase of the DOC temperature that along this driving cycle are low because of the low engine load.

Finally, the results on the US06 driving cycle are summarized in Tab.4.7. Along this driving cycle the electrification improves the fuel consumption by 6.1 % for the MHV and by 5 % for the MHV equipped with the EHC. Tailpipe nitrogen oxides emissions are improved by 16 % when the MHV is considered and by 23.6 % when the EHC is adopted.

## 4.4 Electric Supercharger (eSC)

The availability of high electric power given the introduction of a 48 V battery, gives room for the assessment of the impact, in terms of transient performance and

Table 4.6: Impact of hybridization and introduction of an Electrically Heated Catalyst on the FTP-75 driving cycle

| | BASE | MHV | MHV + EHC |
|---|---|---|---|
| Norm. Corrected $CO_2$ | 100% | 91.0% | 99.5% |
| Norm. EO NOx emissions | 100% | 75.0% | 80.2% |
| Norm. TO NOx emissions | 100% | 70.3% | 43.6% |

Table 4.7: Impact of hybridization and introduction of an Electrically Heated Catalyst on the US06 driving cycle

| | BASE | MHV | MHV + EHC |
|---|---|---|---|
| Norm. Corrected $CO_2$ | 100% | 93.9% | 95.0% |
| Norm. EO NOx emissions | 100% | 84.9% | 87.9% |
| Norm. TO NOx emissions | 100% | 84.0% | 74.4% |

fuel consumption, of an additional electric device: the electric Supercharger (eSC). This component, of which technical characteristics were reported in Ch.2, is modelled by means of an electric motor (described in terms of torque curve and efficiency map) that drives a compressor (represented by map data). A shaft (that reproduces the dynamics of the eSC on the basis of its moment of inertia and a friction torque) links the electric motor with the compressor. In this analysis, the eSC is placed downstream of the main turbocharger before the Charge Water Cooler. A downstream layout is preferred for compressor map width, as pointed out by Rothgang et al. [68] and Breitbach et al. [69] since due to the lower boost pressure ratio, the power consumption is lower as well as the required compressor map width. In a previous work [24], in which a B-SUV vehicle was equipped with a 1.5 L engine, the downstream eSC layout showed slight advantages, in terms of vehicle transient performance, only if coupled with major engine modification. As a matter of fact, the advantage of the downstream layout with respect to the upstream layout ranged from 0 s, for a manoeuvre time of 5.1 s in the 60-80 km/h in VI gear, to 0.4 s (5.1 s vs 5.5 s) in the same manoeuvre when the Miller engine is adopted.

A bypass is modelled on the main air path so that when the eSC is activated the charging system works as a series dual stage charging, while when the eSC is deactivated (above engine speed of 3000 rpm), it does not result in a flow restriction.

### 4.4.1 eSC Rule Based Controller

Currently, several approaches could be exploited to integrate the electric boosting system in the engine control strategy. Heuristic control techniques were developed by

Griefnow et al. [33] for mild hybrid gasoline powertrains and by Schaub et al. [70] for a mild hybrid diesel powertrain. Model Predictive Control (MPC) was also investigated by Liu et al. [71] on a small Diesel engine with variable geometry turbine and exhaust gas recirculation valve.

In order to assess the potential in terms of fuel consumption and transient performance of the vehicle with eSC, in this work the rule based controller for eSC activation and controller developed in [24] was used. The controller defines the operating modes of the eSC and provides the eSC target speed to a PI controller which acts on the electric power request of the eSC motor. In addition, when deactivated, the eSC is still operated at an idle speed of 5000 rpm so that it can accelerate in a faster way and to avoid too frequent high static load to the eSC bearings due to the start from zero speed. When at idle the eSC requires an electric power of about 20 W. The controller flowchart, available in App.A in Fig.A.10, shows the states of the eSC and the system signals needed for the control. At engine start-up the eSC switches on in the eSC idle operation mode and, as already said, it is operated at 5000 rpm while the bypass valve is kept open. If the engine speed is below 3000 rpm and the boost request before the throttle is above the actual boost provided by the main turbocharger by a threshold (0.4 bar) the eSC is activated with a target speed equal to the eSC maximum speed and the bypass valve is closed. The choice to activate the eSC at engine speed lower than 3000 rpm is driven by the fact that for this engine at speed higher than 3000 rpm the turbolag is negligible. When the requested boost pressure is achieved, the eSC speed is controlled to operate at the speed computed on the compressor map from the corrected (according to eSC intake pressure and temperature) mass flow of the engine and the pressure ratio required by the eSC. In this analysis the eSC is initially devoted to reduce the so called turbolag of the turbocharger engine. For this reason the required eSC pressure ratio is computed as the ratio between the demanded boost pressure and the actual pressure ratio provided by the main turbocharger. This latter is computed sensing on the FRM engine the pressure upstream and downstream the main turbocharger and taking into account the pressure losses of the low and high pressure line (e.g. the intercooler pressure drop). In this way the eSC operation is transparent to the main turbocharger that is exploited in the same manner (i.e. as if it were the only charging device) as in the conventional engine. Additionally, a bypass valve opening and closure rate equal to $\pm 450\,^{\circ}\,s^{-1}$ is considered in order to take into account the physical actuation delay of the component. The controller is able to operate the eSC at steady state operation, as well as during vehicle transient manoeuvres or along a driving cycle.

### 4.4.2 Engine full load

The introduction of an auxiliary electric boosting system may be exploited for the increase of the low end torque of the engine since at low speed the energy that can be extracted by the turbine is low. For this reason an analysis of the potential full load curve given the introduction of the eSC is here investigated. For the evaluation of the

full load curve with eSC, the engine limitations shown in Tab.4.8 are considered. These limitations take into account the maximum allowed gas inlet temperature of the turbocharger, the maximum in-cylinder pressure and the engine noise. Additionally the air-fuel ratio has been bounded below by the air to fuel stoichiometric ratio.

Table 4.8: Engine limitations

| | | |
|---|---|---|
| Max Fueling per cycle per cylinder | 65 | mg |
| Outlet compressor temperature | 170 | ˚C |
| Outlet eSC temperature | 180 | ˚C |
| T3 | 850 | ˚C |
| Pmax | 160 | bar |
| Noise | 90 | dB |

The rail pressure, the boost pressure, main and pilot injected fuel mass and respective start of injection were optimized to obtain the maximum brake torque, in such a way to guarantee the compliance with the engine limitations previously discussed. The result of this optimization is shown in Fig.4.10. In this figure the brake torque, the boost pressure and the eSC electric power of the base engine and those achieved after the introduction of the electric boosting system are shown. Concerning the brake torque, the higher boost pressure available thanks to the electric boosting system improves the torque by 20 Nm at 1500 rpm with an electric power request of 860 W. The beneficial impact of the eSC increases at 1250 rpm where a mere electrical need of 1022 W improves the engine brake torque from 201 Nm to 305 Nm. Finally, at 1000 rpm the engine with eSC achieves 281 Nm with a noteworthy improvement by 118 % over the base engine, at the expense of a steady state electric requirement of 3570 W.

### 4.4.3 Transient results

After the development of the engine steady state performance, in this section the assessment of the transient performance of the vehicle is presented. Three different vehicle transient manoeuvres are evaluated with the aim to cover the typical elasticity manoeuvres for the characterization of the vehicle drivability and the so-called fun to drive, as reported by Coltro [72]. Moreover, the performance of the engine on a wide range of engine speed is explored by adopting these transient test as reference manoeuvres. The vehicle transient performance is therefore evaluated according to two elasticity tests from 80 to 120 $\mathrm{km\,h^{-1}}$ with two different engaged gear, V and VI gear and a elasticity test from 60 to 80 $\mathrm{km\,h^{-1}}$ in the VI gear for the assessment of the transient performance from very low engine speed (1082 rpm). In order to evaluate the impact of the hybridization and the introduction of the electrified boosting system, different cases exploring the individual activation of BSG and of the eSC are analysed. In Fig.4.11, engine brake torque, engine boost pressure and BSG mechanical power along the 80 to

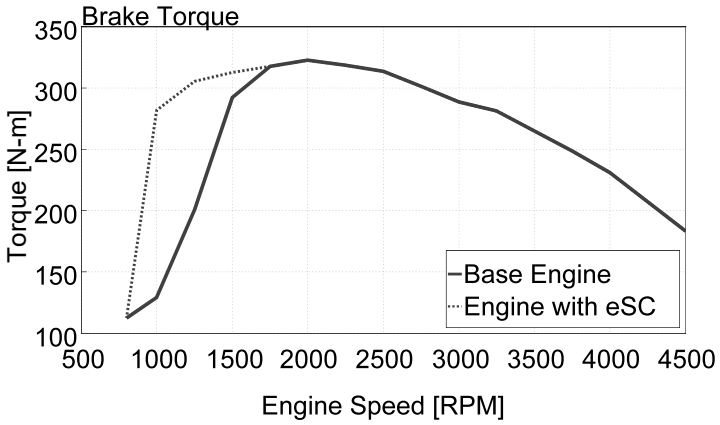


(a) Engine Brake Torque

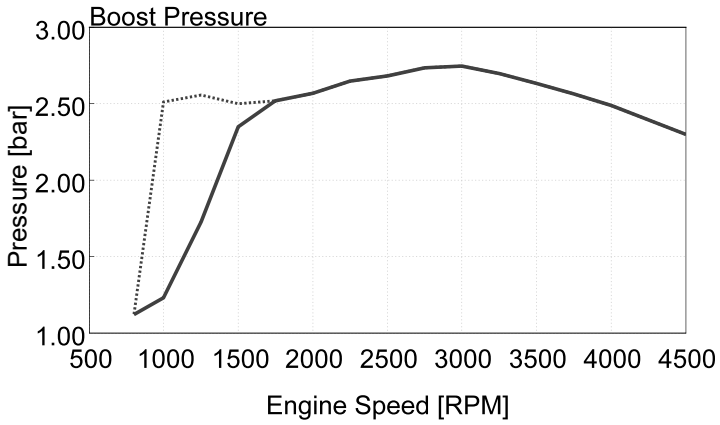


(b) Boost pressure

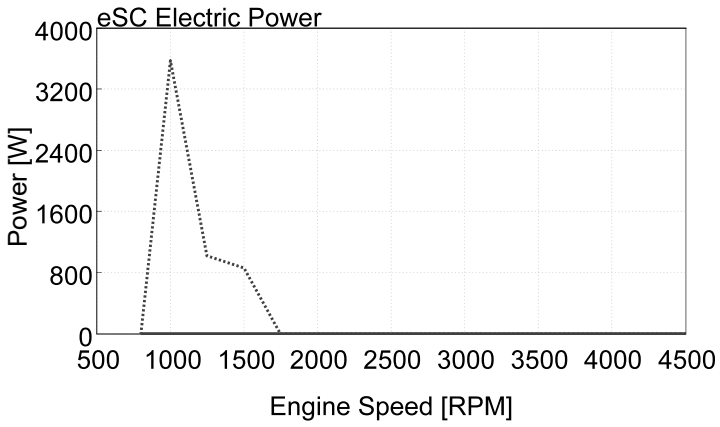


(c) eSC electric power request

Figure 4.10: Engine full load curve: base and with eSC

120 km h$^{-1}$ in V gear are shown. The activation of the BSG improves the vehicle speed and acceleration with an indirect impact of the engine torque only limited to the faster rise of the engine speed. The eSC, on the other hand, guarantees a prompt boost pressure build-up with consequent rise of the engine brake torque. The BSG is affected by the activation of the eSC since the maximum battery discharge power limits the electric power available and the eSC has the priority over the BSG. In this manoeuver the eSC activation lasts just 4 s. For the sake of brevity, vehicle speed, acceleration and eSC speed, alongside the elasticity manoeuvres from 80 to 120 km h$^{-1}$ in VI gear and the 60 to 80 km h$^{-1}$ in VI gear, are presented in App.A.

Additionally, the full load of the engine exploiting the eSC also during steady state operation is considered (see Fig.4.10), defined as engine adopting an Overtorque (OT) mode. For this case, the calibration maps of, as an example, the boost pressure, the injected quantity and the start of injection are expanded beyond the base engine rated torque curve adopting the calibration of the engine featuring the eSC. In Fig.4.12 the adoption of the engine overtorque from low engine speed on the engine performance along the manoeuvre 60 to 80 km h$^{-1}$ in VI gear is reported and compared with the case with the base full load curve. In this manoeuvre the engine with overtorque (i.e. the updated calibration) achieves a higher boost pressure actually reducing the eSC activation time (but not the eSC required energy along the transient manoeuvre, see Tab.4.11). Moreover the brake torque of 300 Nm is achieved rapidly with a constant gradient while the base engine shows a two step behaviour: a fast rise to 150 Nm and a slower rise to 300 Nm. The impact of the BSG on the brake torque is negligible and only small differences are noticeable on the boost pressure, showing the beneficial impact of the engine speed increase given the torque contribution of the BSG on the overall vehicle speed. For this reason, if the BSG is used, the eSC switches off earlier along the transient.

In Tab.4.9, the comparison in terms of elasticity time among transient manoeuvres and the impact of BSG and eSC activation is presented. The usage of BSG or eSC along the transient 80 to 120 km h$^{-1}$ in V gear gives the same improvement by 12.3 %, while the concurrent activation of the two electric devices improves the transient time up to 77.6 % of the reference. The impact of the overtorque is negligible and the reduction in time is only 0.1 % when both BSG and eSC are activated. A higher impact on transient time reduction given the electrification is achieved on the 80 to 120 km h$^{-1}$ in VI manoeuvre. The eSC improves the transient time by 17.3 %, slightly lower than the introduction of the BSG (−17.8 %), while the concurrent activation of the two reduces the transient time by 40.5 %. In this configuration the engine with overtorque improves the transient time of the vehicle by just an additional −0.4 %. Finally on the 60 to 80 km h$^{-1}$ manoeuvre, the BSG only vehicle performs better than the eSC vehicle (−37.9 % and −30.9 %, respectively). When the activation of the two is combined, the vehicle improves its elasticity time by 51.8 %. The engine with overtorque allows to achieve an impressive −63.1 % on this manoeuvre.

The experimental data available in [63] show that, thanks to the activation of the

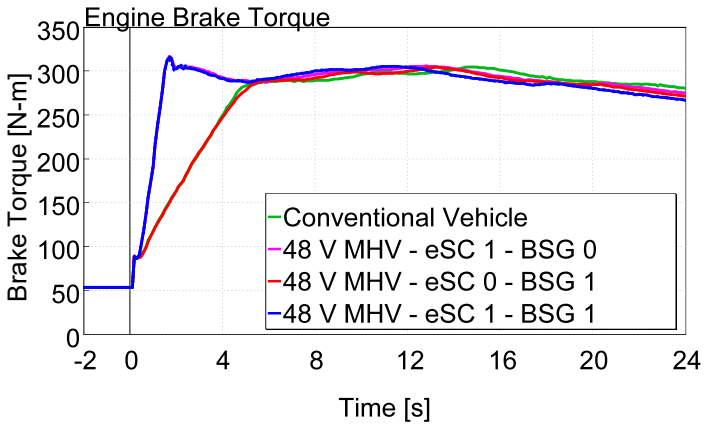


(a) Engine Brake torque

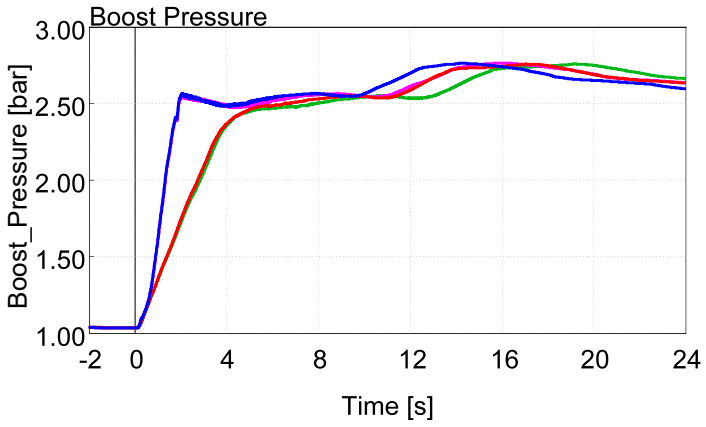


(b) Engine Boost pressure

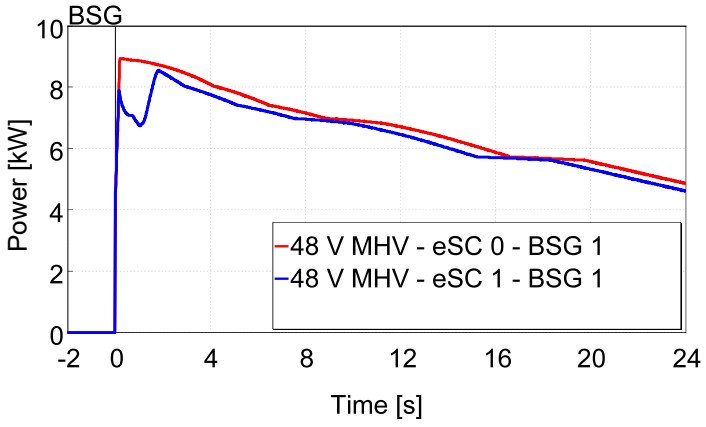


(c) BSG Mechanical Power

Figure 4.11: Elasticity manoeuver 80-120 km/h in V gear

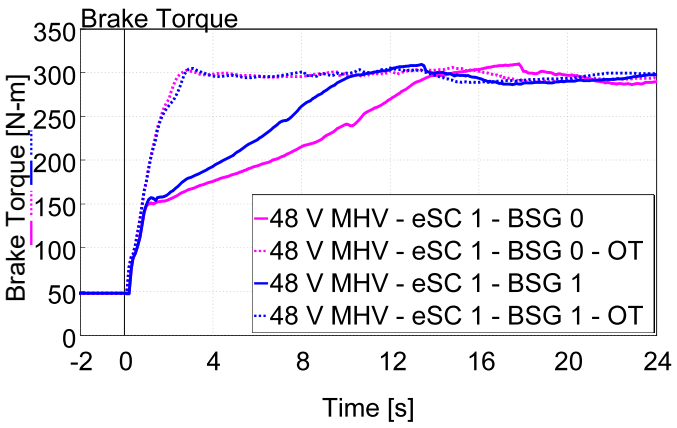


(a) Engine Brake Torque

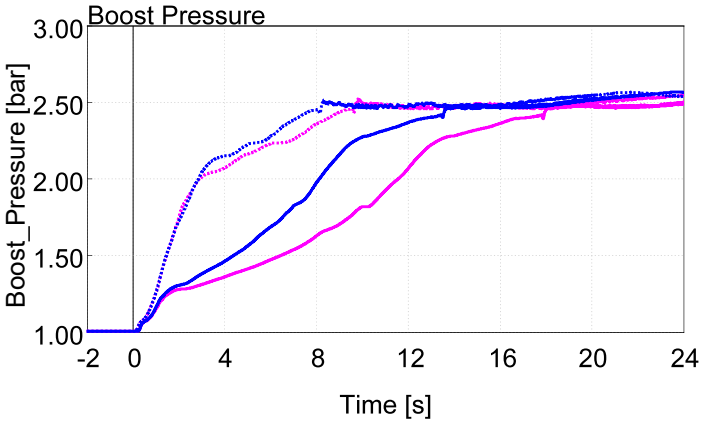


(b) Boost pressure

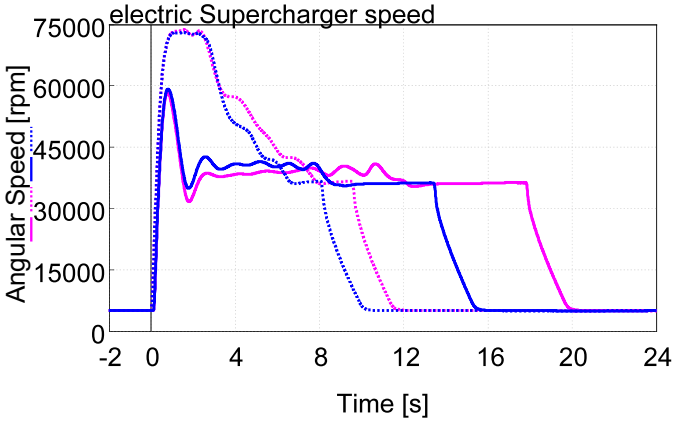


(c) eSC electric power request

Figure 4.12: Elasticity manoeuver 60-80 km/h in VI gear: impact of the engine with Overtorque feature

Table 4.9: Transient manoeuvers time summary. OT: overtorque

| **Transient time [s]** | **80-120 km/h V** | **80-120 km/h VI** | **60-80 km/h VI** |
|---|---|---|---|
| Conventional Vehicle | 100% | 100% | 100% |
| MHV - eSC 1 - BSG 0 | 87.7% | 82.7% | 69.1% |
| MHV - eSC 1 - BSG 0 - OT | 87.7% | 82.0% | 44.5% |
| MHV - eSC 0 - BSG 1 | 87.7% | 82.2% | 62.1% |
| MHV - eSC 1 - BSG 1 | 77.6% | 69.5% | 48.2% |
| MHV - eSC 1 - BSG 1 - OT | 77.5% | 69.1% | 36.9% |

eSC, an improvement by 74 % of the time to reach the 90 % of the full load engine torque and a reduction by 13 % of the elasticity time in the manoeuvre 80 to 120 km h$^{-1}$ in VI gear. In the present simulation work, the 90 % of the full load engine torque is achieved, given the introduction of the eSC, 81 % earlier and the time to reach the final speed of 120 km h$^{-1}$ is 17.3 % lower. Although this difference seems reasonable, the reason to this deviation between the experimental test and the simulation results may be due to the fact that the eSC controller developed and adopted in the model performs differently from the one developed for the experimental activity. Indeed, in the vehicle model developed in this work, the eSC is transparent to the VGT controller. This means that the VGT is controlled to achieve the target boost pressure as if it were the only boosting system, but in [63] a difference in the VGT controller actuation after the activation of the eSC is shown. The difference in turbocharger control, hence, may cause the difference in the impact that the eSC may have on this transient manoeuvre.

In Tab.4.10 and 4.11, the mechanical energy required by the BSG and the electrical energy required by the eSC along the transient is shown. While BSG energy is mainly dependent on the transient length, the eSC energy is a measure of the engine requirement to fill the boost request and reduce the so-called turbolag. The eSC deactivates, indeed, when the difference between target and sensed boot pressure reduces below 50 mbar. The BSG energy is slightly more than 20 Wh along the 80 to 120 km h$^{-1}$ in V gear, which increase to around 20 Wh when the same manoeuvre is performed in VI gear. The BSG mechanical energy ranges from 12.76 Wh to 25.59 Wh on the 60 to 80 km h$^{-1}$ in VI gear, where the lower value is when the vehicle exploits the engine overtorque and the combined eSC and BSG power. This is due to the strong reduction in transient time in this configuration with respect to the vehicle that relies on the BSG contribution only. The eSC energy is, overall, one order of magnitude less than the BSG energy also neglecting the electric to mechanical conversion efficiency, even if on the 80 to 120 km h$^{-1}$ manoeuvres the BSG and the eSC individually brings the vehicle to achieve the same transient performance. Finally, the adoption of the overtorque full load curve reduces the energy required by the eSC thanks to the updated calibration of the engine that more effectively exploits and integrates the assistance of the electric supercharger. Indeed, anticipating a higher boost pressure from low engine speed

increases the engine mass flow rate and the power of the exhaust gases that can be extracted by the turbine.

Table 4.10: BSG Mechanical Energy along the transient manoeuvers

| BSG Mech. Energy [Wh] | 80-120 km/h V | 80-120 km/h VI | 60-80 km/h VI |
|---|---|---|---|
| Conventional Vehicle | 0 | 0 | 0 |
| MHV - eSC 1 - BSG 0 | 0 | 0 | 0 |
| MHV - eSC 1 - BSG 0 - OT | 0 | 0 | 0 |
| MHV - eSC 0 - BSG 1 | 25.61 | 36.69 | 25.59 |
| MHV - eSC 1 - BSG 1 | 21.66 | 29.38 | 18.68 |
| MHV - eSC 1 - BSG 1 - OT | 21.65 | 29.6 | 12.76 |

Table 4.11: eSC Electric Energy along the transient manouevers

| eSC El. Energy in [Wh] | 80-120 km/h V | 80-120 km/h VI | 60-80 km/h VI |
|---|---|---|---|
| Conventional Vehicle | 0 | 0 | 0 |
| MHV - eSC 1 - BSG 0 | 1.28 | 2.55 | 2.32 |
| MHV - eSC 1 - BSG 0 - OT | 1.28 | 1.74 | 4.06 |
| MHV - eSC 0 - BSG 1 | 0 | 0 | 0 |
| MHV - eSC 1 - BSG 1 | 1.27 | 2.28 | 1.83 |
| MHV - eSC 1 - BSG 1 - OT | 1.27 | 1.51 | 3.57 |

### 4.4.4 Driving cycle results

The impact of the introduction of the eSC is evaluated along different driving cycles. The impact of the EHC is not considered in this analysis and this device is disabled in the following analysis. Carbon dioxide emissions and engine out and tailpipe nitrogen oxides emissions are reported in Tab.4.12. Concerning carbon dioxide emissions, the vehicle featuring the eSC has slightly higher fuel consumption in any driving cycle. This increase ranges from 0.1 % on WLTC and RTS95, to 0.6 % along the FTP75. The vehicle featuring the eSC reduces by up to 3.3 % the engine out nitrogen oxides emissions on the WLTC. The activation of the eSC rapidly increases the air mass flow rate and the air to fuel ratio and at the same time reducing the in-cylinder temperature with a beneficial effect in hindering the nitrogen oxides emissions formation. On the contrary, lower engine out temperature translates in lower conversion efficiency for the SCR, thus suggesting that the eSC should be operated when the engine is fully warmed-up. Hence, the tailpipe emissions increases significantly on all driving cycles ranging from 3.4 % on the US06 up to 18.6 % on WLTC and 19.9 % on the RTS-95. The slight increment of

the engine out nitrogen oxides emissions on the RTS-95 may be explained by the fact that, since this is an aggressive cycle, when the engine performance is bounded by the smoke limit and the eSC is activated, more fuel is injected and the engine operates at higher load. If this phenomenon on the overall cycle has a negligible impact on the fuel consumption (just 0.1 %), it has a higher impact on the nitrogen oxides emissions which are extremely sensitive to in-cylinder temperature.

Even if these results show that the direct adoption of an eSC in a powertrain may cause an increase of fuel consumption and pollutant emissions, this device may, in some cases, become beneficial. As a matter of fact, the air management improvement after the introduction of the eSC may reduce soot emissions during transient operation, thus reducing the soot loading on the DPF with a lowering of the fuel penalty from the soot trap regeneration. When adopted on a powertrain featuring Low Pressure EGR, an higher amount of EGR can be attained with benefits in terms of nitrogen oxides engine out emissions. Moreover, the performance improvement that can be achieved by the powertrain featuring the eSC can be traded for fuel consumption improvement [50], adjusting the turbocharger size, through downsizing or downspeeding [73]. For this, final drive elongation and the adoption of a turbine with a higher flow permeability may be adopted. As reported by Schaub [74], the introduction of the eSC can reduce the fuel consumption by 0.9 % when coupled with a large exhaust gas turbocharger designed for higher efficiency and lower back-pressure.

Table 4.12: Carbon dioxide, engine-out and tailpipe nitrogen oxides emissions along type approval and RDE driving cycles with and without the eSC (normalized on the basis of the conventional vehicle)

| | **WLTC** | | **RTS-95** | | **FTP-75** | | **US06** | |
|---|---|---|---|---|---|---|---|---|
| | **MHV** | **+ eSC** | **MHV** | **+ eSC** | **MHV** | **+ eSC** | **MHV** | **+ eSC** |
| Norm. $CO_2$ | 93.8% | 93.9% | 91.6% | 91.7% | 91.0% | 91.6% | 93.9% | 94.1% |
| Norm. EO NOx | 89.4% | 86.1% | 78.2% | 79.8% | 75.0% | 74.6% | 84.9% | 83.1% |
| Norm. TO NOx | 77.9% | 96.5% | 92.7% | 112.6% | 70.3% | 83.4% | 84.0% | 87.4% |

In Tab.4.13 the specific mechanical energy of the BSG when operated in different hybrid modes as regenerative braking, torque assist and load point moving are shown. Additionally the specific energy requirement for the eSC is reported. The eSC energy need increases for aggressive driving cycle, while remaining one order of magnitude less than the regenerative braking energy. Moreover, the activation of the eSC goes to the detriment of the torque assist in all the driving cycle reported.

To conclude, in Tab.4.14, the breakdown of the electric energy consumed by the eSC is presented along different driving cycles. The electric to mechanical conversion reduces the mechanical energy available by 20.7 % on the RTS-95 to the 25.1 % on the FTP-75. The inertia energy is negligible since the energy used to accelerate the eSC is provided to the flow when the eSC is deactivated. Concerning the friction energy, this

Table 4.13: Specific energy of hybrid functionalities and eSC specific electric energy along type approval and RDE driving cycles

| Wh/km | WLTC | | RTS-95 | | FTP-75 | | US06 | |
|---|---|---|---|---|---|---|---|---|
| | **MHV** | **+ eSC** | **MHV** | **+ eSC** | **MHV** | **+ eSC** | **MHV** | **+ eSC** |
| Regen. Braking | -20.8 | -20.9 | -42.7 | -42.8 | -30.8 | -30.9 | -25.1 | -25.1 |
| Torque Assist | 14.1 | 13.3 | 25.8 | 22.9 | 19.5 | 19.0 | 15.6 | 14.2 |
| Load Point Mov. | -4.5 | -4.7 | -1.1 | -1.1 | -4.6 | -4.6 | -1.0 | -1.0 |
| eSC El. Energy | 0.0 | 1.6 | 0.0 | 3.7 | 0.0 | 1.5 | 0.0 | 2.5 |

value increases for cycle where the overall eSC electric energy demand is low since the eSC is operated, when not activated, at 5000 rpm which corresponds to a power consumption of 20 W required to counteract the device friction. The lower value of the friction energy is achieved on the RTS-95 with only 14.8 % which increases to 32.0 % on the FTP-75. The energy which is at last usable for the compression work ranges between the 42.8 % on the FTP-75 to the 64.4 % on the RTS-95.

Table 4.14: Energy breakdown of the electric energy utilization of the eSC along type approval and RDE driving cycles

| | **WLTC** | **RTS-95** | **FTP-75** | **US06** |
|---|---|---|---|---|
| eSC Elec. Energy | 100% | 100% | 100% | 100% |
| eSC Mech. Energy | 76.6% | 79.3% | 74.9% | 79.2% |
| eSC Inertia Energy | 0.1% | 0.0% | 0.0% | 0.1% |
| eSC Friction Energy | 25.2% | 14.8% | 32.0% | 15.0% |
| eSC Compr. Energy | 51.3% | 64.4% | 42.8% | 64.1% |

## 4.5 Virtual Calibration

The opportunity and the potential of the comprehensive vehicle integrated platform goes beyond the assessment of the impact of the electrification on fuel consumption and pollutant emissions. The virtual test rig developed in this work moved from a in-cylinder predictive combustion model to a MHV model featuring auxiliary devices as EHC and eSC. Moreover the integration of the coolant circuit and of the aftertreatment circuit enabled the vehicle model to a fully predictive assessment of vehicle transient performance, fuel consumption, engine-out and tailpipe nitrogen oxides emissions. The high level of accuracy shown during the validation activity (see Ch.3) and the flexibility in terms of architectures (e.g. the assessment of the eSC impact on the engine maximum performance and on vehicle transient manoeuvres) enables this vehicle model to

be proficiently used for the virtual calibration of the entire powertrain. For this reason, in this section, a methodology for the virtual calibration of the engine is developed and discussed. Firstly the selection of the Key Points is discussed. Afterwards the optimization methodology is presented and the updated calibration maps are defined. Finally the results in term of fuel consumption and nitrogen oxides emission along the WLTC are shown.

### 4.5.1 Key Points Selection

In this work, the local approach for engine calibration has been chosen, in which the operating points of the driving cycles are grouped into a reduced number of points which are commonly referred to as Key Points. Moreover, in "a driving cycle as the WLTC, to adequately model the engine behavior the number of KPs can be anywhere between 18 and 25. For RDE, the number of KPs are typically between 25 and 30" [75]. This approach has been chosen in such a way that any KP can be optimized locally with no dependence from the other KPs and the calibration map is revised with the updated calibration.

> This means that value of the control parameter or emission at different KPs do not influence each other in any way. Thus, both the modelling and optimization is carried out locally for each KP. This is the reason that the approach is known as local approach for calibration. Once the optimum value of the control parameters for all the KPs are found, the calibration maps are generated using interpolation and extrapolation. [75]

For this reason, the value of the control parameter for neighbouring KPs can be very different, and this would require a manual smoothening of the calibration map. However, in this work, no smoothness requirement has been considered.

The procedure for the definition of the KPs starts from the engine operating points of the conventional vehicle driven along WLTC, RTS-95, FTP75 and US06. These points are then grouped by a clustering algorithm (the nearest neighbour algorithm) to a grid defined on the basis of the engine operating points on the experimental engine calibration map. Moreover, each engine operating point is weighted and sorted on the basis of the frequency and its energy impact on the driving cycles. For this analysis the first 17 KPs based on the high energy weight and the first 2 KPs above 1000 rpm based on the frequency of occurrence are selected. In Fig.4.14, these KPs, which are chosen for the subsequent optimization, are shown. They are reported with their relative weight in App.A, in Tab.A.2. These KPs are representative of more than the 35 % of the total energy along the driving cycles investigated.

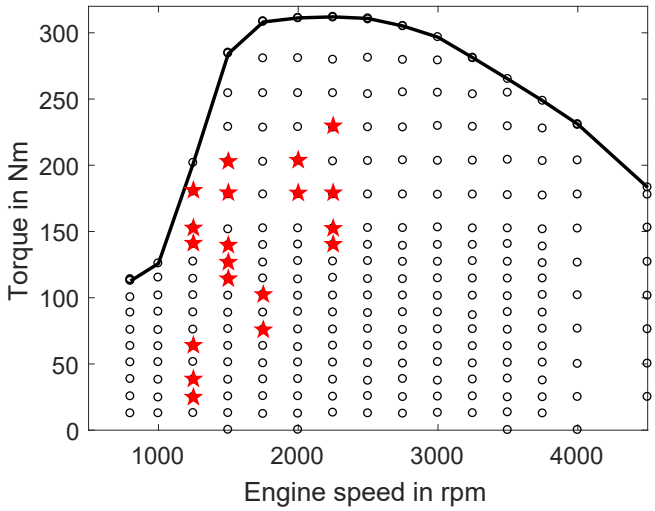


Figure 4.13: Virtual calibration key points (red star) and reference calibration map points (circle)

### 4.5.2 Optimization

Since the aim of this work is to illustrate the potential of an integrated modelling approach, different hardware improvements on top of the base engine are considered. Hence, before introducing the optimization methodology, the test matrix chosen is reported in Tab.4.15. To explore the potential of the base system, in Case A the number of fuel injections is increased from 4 (two pilot injection, a main and an after injection) up to 7 (with three additional pilot injections) with the aim to exploit the Injection Rate Shaping (IRS) concept. For the sake of simplicity and to avoid an excessive number of independent variables, a single optimization variable defines the fuel mass of the first three additional pilot injections. Case B sees the introduction of a theoretical injector with no injection delay allowing shorter injection patterns. Even if this is only a theoretical investigation, the reduction of the injection delay may be achieved with piezoelectric injectors. This analysis, indeed, is aimed to show the potential of this ideal injector in terms of engine performance on a driving cycle. In the last two cases, Case C and D, the eSC as additional boosting system is investigated and the base injector (i.e. with injection delay) is maintained. Differently from Case C, Case D adopts a continuous valve actuation which is operated for Late Intake Valve Closing (LIVC) to exploits the advantages of the Miller cycle.

The independent variables selected for the optimization can be divided in injection variables and gas exchange variables. The injection variables are: four injected fuel mass variables, since the first three pilot injections share the same fuel mass and the main injection is controlled to achieve the target load, and seven different SOIs. The

Table 4.15: Test matrix and technologies investigated

| | **Technology** |
|---|---|
| A | Injection Rate Shaping (up to 7 injections) |
| B | IRS with theoretical injector (without hydraulic delay) |
| C | eSC (electric boosting in steady state operation) |
| D | eSC and Miller cycle (LIVC) |

gas exchange variables are EGR rate, the set-point for the boost pressure and the intake valve closing (for case D only). The boost pressure set-point, in Case C and D, is used to control the eSC operation according to the rule based eSC controller presented in Sec.4.4.1: when the VGT is not able to provide sufficient charging power to achieve the target boost pressure, the eSC activates to close the gap. Overall, the independent variables are fourteen (fifteen, when Case D is considered) and as settings for the GA optimization a population size of 50 members and a number of generations equal to 40 are chosen. These settings provide, at the end of the optimization (i.e. after 2000 iterations) that a sufficient number of potential calibration sets is available. Among the results of the optimization, the calibration sets that do not satisfy the constraints of torque (±3 %) and air to fuel ratio (i.e. the minimum allowed air to fuel ratio is 0.5, lower than that of the reference case), are removed from the results. These results have been analysed evaluating the optimal calibration sets on a Pareto front based on BSFC and combustion noise for all the KPs.

An example of the optimized Pareto fronts with the technologies presented in Tab.4.15 is shown in Fig.4.14 for the operating point at 1500 rpm and 179 Nm. Adopting the IRS (Case A), an improvement of the trade-off between BSFC and combustion noise is noticeable. The IRS, at a comparable BSFC as the base engine, reduces the combustion noise by −2 dB at the cost of an increase of BSNOx by 50 %. The scenario changes remarkably when the theoretical injector with no hydraulic delay is introduced. In this case both fuel consumption and combustion noise reduce by a great extent: the BSFC reduces by slightly more than 1.5 % while the combustion noise fall by about 7 dB. These results are confirmed by some previous simulation activity done by Piano et al. [76]. The adoption of the eSC and the base injector (Case C), has a beneficial effect on BSNOx with respect to Case A considering the calibration set that achieves the same BSFC of the reference case with a reduction of the combustion noise. The best BSFC obtained by the engine featuring the technologies of Case C is lower by 3 %, excluding the eSC electric energy requirement but at BSNOx higher than the Base engine. The eSC electric power is neglected in the computation of the BSFC since a proper assessment of the powertrain efficiency is to be done along the driving cycle in order to correctly weight the electric cost in the overall vehicle fuel consumption. The energy coming from the regenerative braking may, indeed, reduce the cost of the electric energy along the cycle thus promoting the usage of the eSC to improve the engine efficiency. Finally, the adoption of the

LIVC has a great impact on the reduction of the nitrogen oxides specific emissions: the same BSNOx of the base engine is combined with a reduction of BSNOx higher than 3 %.

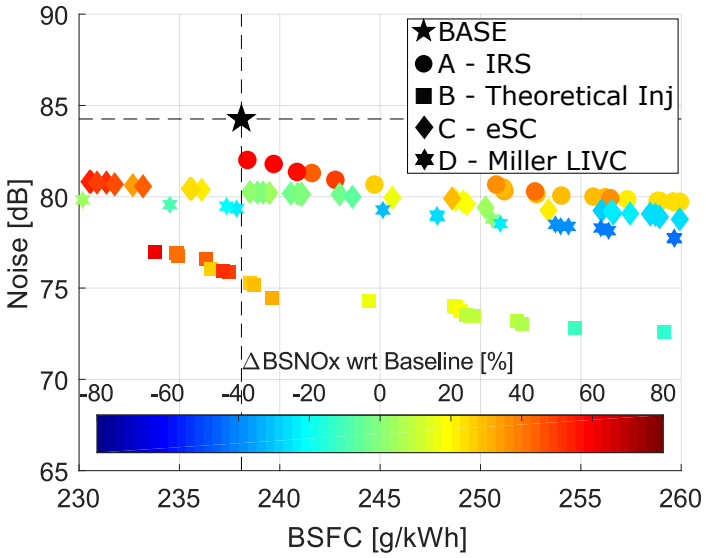


Figure 4.14: Virtual calibration: Pareto front BSFC - Noise for Case A, B, C and D at 1500 rpm and 179 Nm

### 4.5.3 Updated calibration maps

After the optimization process, several calibration sets for each operating points can be chosen to update locally the calibration map. In this work, the calibration set that gives the lower BSFC while at the same time having a combustion noise equal or lower to the reference, is taken as optimum for each operating points. Since each operating point is optimized independently, no information is available among the operating points and no smoothness requirement is here taken into account. Moreover, interpolation between calibration variables is performed along the driving cycle when the engine speed and load falls among the discrete operating points on the calibration map. For this reason, two different methods to build the maps, which affects the interpolation among operating points, have been followed and graphically shown in Fig.4.15. The first method, to which the figure refers to as Type I, simply consists in swapping the original calibration sets of the KP with the optimized calibration sets that guarantees the minimum BSFC. The second method, Type II, assumes that the interpolation among KP properly describe the optimal choice of the calibration sets. Therefore, each KP can be representative of a wider region on the engine operating map and the calibration sets of the operating points that lie among the optimized KP can be neglected.

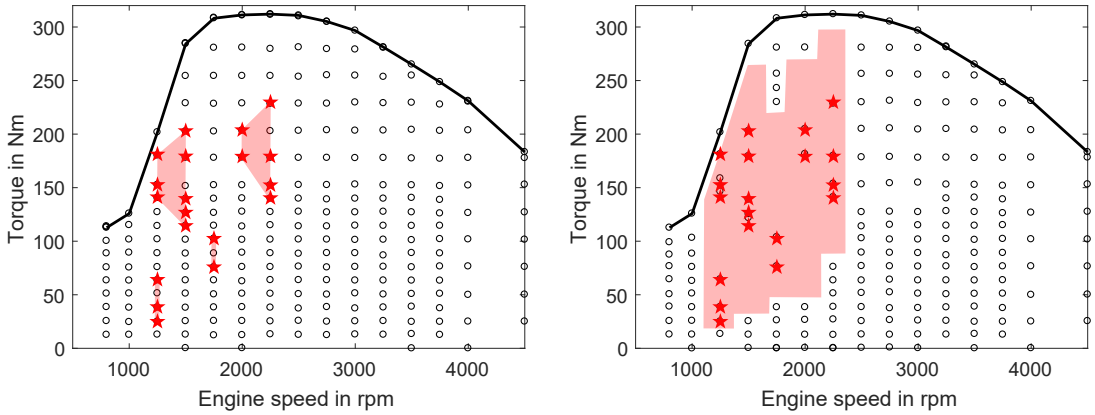


(a) Type I

(b) Type II

Figure 4.15: Map Interpolation

### 4.5.4 Driving cycle results

In this section the results of the calibration maps is reported. The results of the optimization from Case A (with the IRS), Case B (theoretical injector without hydraulic delay) and Case C are considered. Type I and Type II interpolation is performed on Case A, but for the sake of brevity only Type II interpolation on Case B and Case C is followed. The results in terms of emission along the WLTC of the vehicles featuring the updated calibration maps are compared with the reference vehicle. Case A and Case B calibration maps are assessed using the 12 V conventional vehicle model, while to correctly account for the electric consumption of the eSC, the 48 V MHV model is adopted for Case C. In Tab.4.16 the results in terms of carbon dioxide, engine out nitrogen oxides and tailpipe out emissions are presented. The calibration map A - Type I achieves a reduction of about 0.5 % with an increase in terms of engine-out nitrogen oxides emission by 17.2 %. Thanks to increased temperature at the DOC outlet in the medium and high phase of the WLTC cycle, this calibration map improve the tailpipe nitrogen oxides emission by 10.1 %. The calibration map A - Type II, reduces by 0.7 % the fuel consumption with engine out nitrogen oxides emissions higher than the calibration map Type I. Overall the tailpipe emissions are slightly lower than the reference case by 1 %. The Case B - Type II calibration maps achieve the lowest fuel consumption among the cases with an improvement of 0.9 % with respect to the reference case. Moreover, the tailpipe emissions of nitrogen oxides is reduced by 8.2 %. Fig.4.16 compares DOC outlet temperature, engine-out and tailpipe NOx emissions of the conventional vehicle with Case A calibration (with both interpolation methods) and Case B calibration (with Type II interpolation), along the WLTC.

Regarding Case C, the updated calibration map is provided to the engine virtual electronic central unit as new boost pressure and injection set-points and also to the EEMS

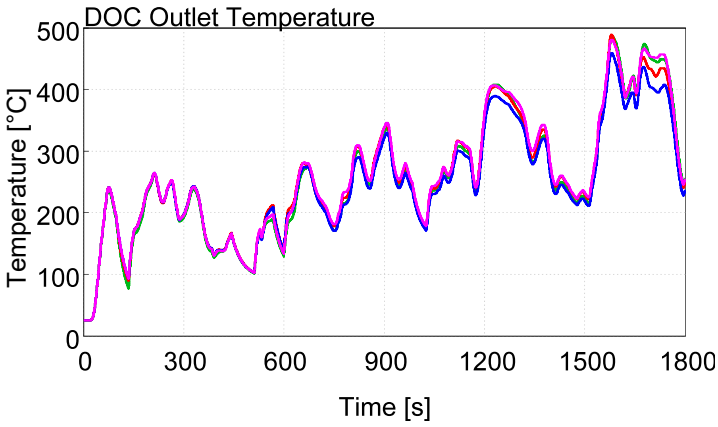


(a) T DOC

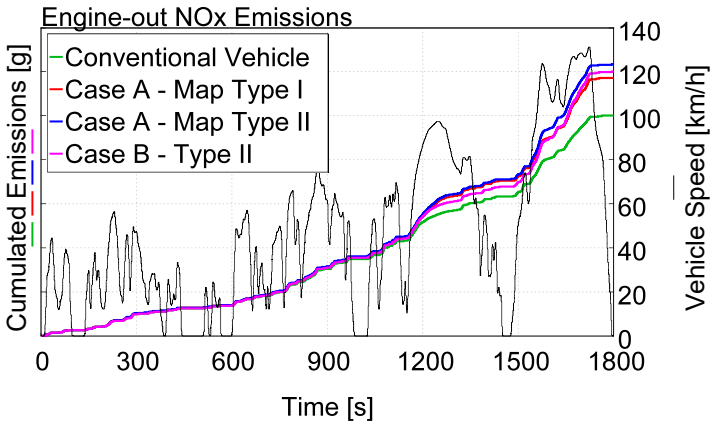


(b) EO NOx Emissions

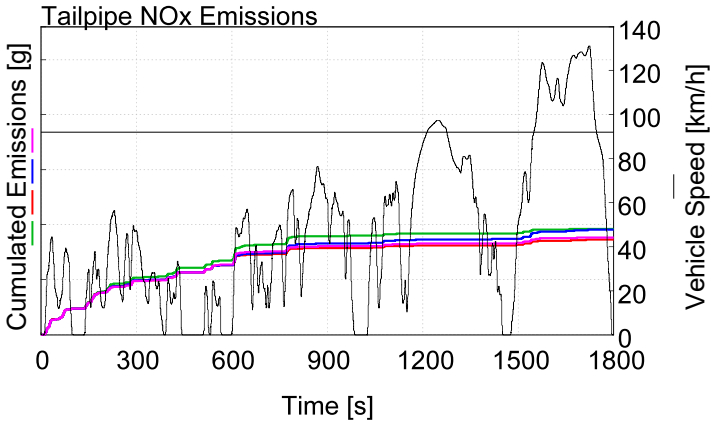


(c) TO NOx Emissions

Figure 4.16: Virtual calibration: comparison of calibration maps

Table 4.16: Virtual calibration: emission results

| | Base | A - Type I | A - Type II | B - Type II |
|---|---|---|---|---|
| $CO_2$ | 100% | 99.5% | 99.3% | 99.1% |
| EO NOx | 100% | 117.2% | 123.2% | 120.0% |
| TO NOx | 100% | 89.9% | 99.0% | 91.8% |

as new steady state maps for engine fuel mass and nitrogen oxides mass flow rate. In Tab.4.17 the results of the 48 V vehicle featuring the Case C calibration, in which the engine exploits higher fuel conversion efficiency thanks to the eSC, are compared with the reference vehicle, the 48 MHV with and without eSC. These results shows that for this case study the adoption of Case C calibration is detrimental for the fuel consumption with respect to the MHV with base calibration 0.8 % and to the MHV with the eSC 0.7 %. In this latter case, the eSC is activated only if the turbocharger does not achieve the boost set-point rapidly, while in Case C the eSC is used as dual stage charger also in steady state operation to reduce the pumping losses and improve the engine efficiency. This suggests that in a MHV, using the electric energy to provide torque assistance directly to the crankshaft by means of BSG, as in the MHV case, is more efficient than to provide higher boost pressure by means of an electrical boosting system. Nevertheless, an EEMS aimed to predict the electric power needed for eSC activation could improve the eSC utilization for minimum $CO_2$ emissions as reported by Accurso et al. [77]. Finally, the Case C calibration shows increased engine out and tailpipe nitrogen oxides emissions with respect to the base engine.

Table 4.17: Virtual calibration: emission results with eSC

| | Base | MHV | + eSC | C - Type II |
|---|---|---|---|---|
| $CO_2$ | 100% | 93.8% | 93.9% | 94.6% |
| EO NOx | 100% | 89.4% | 86.1% | 119.3% |
| TO NOx | 100% | 77.9% | 96.5% | 110.4% |

In Tab.4.18, the specific energy split by BSG operating mode and the electric energy consumed by the eSC are reported. Case C - Type II calibration maps activates the eSC by more than three times with respect to the MHV with eSC. This energy requirements comes from the load point moving, which increases in absolute value from 4.7 Wh km of the MHV with eSC to 10.7 Wh km. On the other side, the torque assist operation of the BSG slightly increases to 14.1 Wh km being equal to that of the MHV vehicle. It is to be noted that load point moving operation and the subsequent electric energy for torque assist operation is not efficient since it involves a chemical (from the fuel) to electric (and chemical in the battery) and an electric to mechanical conversion. For this reason, the increase in energy coming from load point moving to guarantee the charge

sustaining operation determines the increment of fuel consumption along the driving cycle.

Table 4.18: Specific energy of hybrid functionalities and eSC specific electric energy along the WLTC

| [Wh/km] | **MHV** | **+ eSC** | **C - Type II** |
|---|---|---|---|
| Regen. Braking | -20.8 | -20.9 | -21.2 |
| Torque Assist | 14.1 | 13.3 | 14.1 |
| Load Point Mov. | -4.5 | -4.7 | -10.7 |
| eSC El. Energy | 0.0 | 1.6 | 5.3 |

In this section a methodology for the virtual calibration has been proposed with the aim to exploit the advantages of the fully physical virtual test bench developed in this work. The possibility to operate directly on the engine calibration allows to tune and optimize the entire electrified powertrain. With this approach, the understanding of the full potential of any powertrain technology is possible. This virtual test rig may indeed be used for the comprehensive analysis of full hybrid vehicles in future development of this work.

# Chapter 5

# Conclusions

Demanding carbon dioxide emissions targets, which are proposed for the next years, will foster the adoption of more efficient powertrains. Diesel engines on the one hand and the electrification trend on the other hand, proved to be the enablers to achieve significantly lower carbon dioxide emissions. Nevertheless, some hybridization strategies aiming to reach lower fuel consumption may lead to penalties in terms of engine-out and tailpipe pollutant emissions. The electrification may, in fact, have a detrimental impact on the powertrain thermal management lengthening the cold start phase of the engine and the aftertreatment light-off. However, the electric power available on hybrid vehicles allows the introduction of electrified auxiliaries as electric catalysts, which may improve the aftertreatment conversion efficiency, or electric superchargers for the improvement of the vehicle transient performance at the expense of an increased powertrain complexity. In this context, numerical simulation can play a significant role in the development of models for the investigation of different hybrid architectures, of different control strategies, of the impact of electrified auxiliaries.

This work aimed to comprehensively address these conflicting targets proposing a novel 0-1D CFD integrated powertrain and vehicle model which was developed on the basis of a 48 V Mild-Hybrid Diesel passenger car. This comprehensive powertrain and vehicle model was targeted to bridge the gap between high fidelity models commonly used for the development of specific components and system level approaches for the evaluation of vehicle technologies and architectures. A 1D-CFD engine model of a 1.6 L 4-cylinder EU6 Diesel engine featuring a predictive combustion model was integrated in a vehicle model featuring a 1D cooling circuit and a 1D aftertreatment system in a commercially available software, GT-SUITE. These components were linked together in such a way that physical quantities were synchronously exchanged. The predictive combustion model developed by Gamma Technologies, DIPULSE, and the fast running engine model were calibrated and validated on a wide range of stationary operating points and different combustion modes showing a high accuracy in reproducing the engine behaviour in steady state and time to boost operations. The conventional vehicle model was able to precisely represent the powertrain and aftertreament thermal state

along the WLTC driving cycle. Indeed, the comprehensive vehicle model reproduced the carbon dioxide emissions with a deviation of only −0.4 % and the engine out nitrogen oxides emissions by −0.3 %. Also, tailpipe emissions were overestimated by 19.8 % caused by differences in the ammonia injection strategy between experimental vehicle and model. After the integration of a resistive battery model, a map based electric motor in lieu of the 12 V alternator and an EMS, the 48 V Mild-Hybrid Diesel passenger car behaviour was well reproduced in terms of engine warm-up, aftertratment light-off and 48 V battery SOC.

The validated powertrain and vehicle virtual test rig was used to investigate the potential of the electrification. The advantage of the virtual test rig to quantitatively assess tailpipe nitrogen oxides was exploited for a comprehensive sensitivity study on the calibration of the Energy and Emission Management Strategy (EEMS). The EEMS was operated to concurrently minimize carbon dioxide and nitrogen oxides emissions. Adopting different weights for carbon dioxide and nitrogen oxides emissions, a trade-off front was defined and the optimal calibration for the reduction of fuel consumption while maintaining the tailpipe emissions below those of the reference vehicle was chosen. This analysis showed that the 48 V hybridization with the EEMS reduces fuel consumption by 8.4 %, engine-out nitrogen oxides emissions by 21.8 % and tailpipe emissions by 7.3 % on the WLTC. Furthermore, a EHC placed upstream the DOC and powered by the energy coming from the battery electric, reduced the tailpipe emissions by up to 22.8 % with respect to the base engine on the same driving cycle. The same analysis was performed along RTS-95, FTP-75 and US06, showing promising results in terms of fuel consumption and tailpipe emission reduction.

Vehicle transient performance were assessed along different elasticity manoeuvres, taking into account the torque assist capabilities of the BSG and also the possibility to adopt an electrically assisted supercharger downstream the main turbocharger. The analysis showed that, after the calibration of the engine full load curve to account for the eSC operation in the LET region, the combined effect of BSG and eSC could reduce the time that the vehicle takes to accelerate from 60 to 80 $\mathrm{km\,h^{-1}}$ in sixth gear by more than 63 %. The impact of the eSC on fuel consumption and nitrogen oxides emissions was assessed along type approval and RDE driving cycles. The activation of the eSC proved to have a slight detrimental effect on fuel consumption by 0.1 % and to increase the tailpipe nitrogen oxides emissions by 18.6 % due to lower exhaust temperature on WLTC.

Finally, a methodology for the virtual calibration of the engine and the prompt assessment of different technologies and engine concepts, on the comprehensive powertrain and vehicle model, was proposed. After the selection of the powertrain KPs over different driving cycles, the engine calibration was optimized considering different technologies: a novel injection strategy (with an injection pattern with up to seven injections), a theoretical injector (with zero hydraulic delay and exploiting an injection pattern of seven injections), the usage of the eSC in steady state operation as additional boosting system and the VVA to take advantage of a Miller cycle (with the adoption

a LIVC strategy). To verify the new calibration maps, driving cycle simulations were performed using the vehicle virtual test rig which showed a potential fuel consumption reduction by 0.9 % and an improvement of the tailpipe nitrogen oxides emissions by a significant 8.2 % when the novel injection strategy applied to the theoretical injector with zero hydraulic delay was considered.

To conclude, the comprehensive 48 V mild hybrid powertrain and vehicle model, proved to be an effective methodological tool: the flexibility to perform different vehicle test and the possibility to integrate and evaluate several powertrain technologies makes this virtual test rig the cornerstone for the development of future electrified powertrains.

# Appendix A

# Additional Data

In this Appendix additional data and graphs are reported.

## Methodology

### Engine

In Fig.A.1, the controlled brake torque, the controlled air flow rate and the manifold volumetric efficiency of the FRM with respect to the experimental data are shown. During the validation phase, the air mass flow rate was imposed as target for the VGT controller and the brake torque as target for the injection controller. Air mass flow rate during motoring operation was not measured (this explains the dots at zero experimental air flow rate in Fig.A.1b) but they were anyway taken considered during the validation phase to evaluate the engine friction model. The evaluation of the accuracy of the model in terms of pressure losses along the air path may be illustrated by the manifold volumetric efficiency, which is shown in A.1c. The manifold volumetric efficiency of the model is slightly higher than the data coming from the experiment (about + 5 %) which is considered acceptable for this FRM engine.

In Fig.A.2 and A.3, the BSFC and the BSNOx of the FRM engine is compared with the experimental data of the Blended and Warm-up combustion mode in cold condition (i.e. the engine coolant temperature is kept at about 40 °C.

In Fig.A.4, main injection SOI, EGR rate and swirl actuation are reported for the Time To Boost at 1500 rpm in Normal combustion mode.

The extended comparison of the FRM engine performance in TTB operation is presented in Fig.A.5, where the load step is additionally performed at 1250 rpm and 1750 rpm. At 1250 rpm, the engine model overestimates the brake torque by 21 Nm. At 1750 rpm the torque gradient is accurately reproduced.

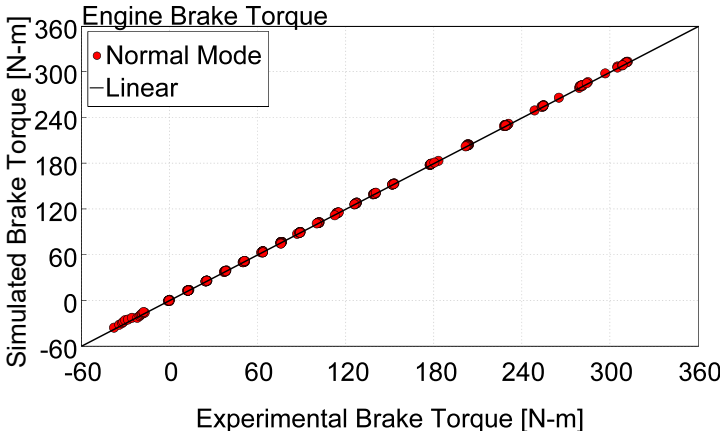


(a) Brake Torque

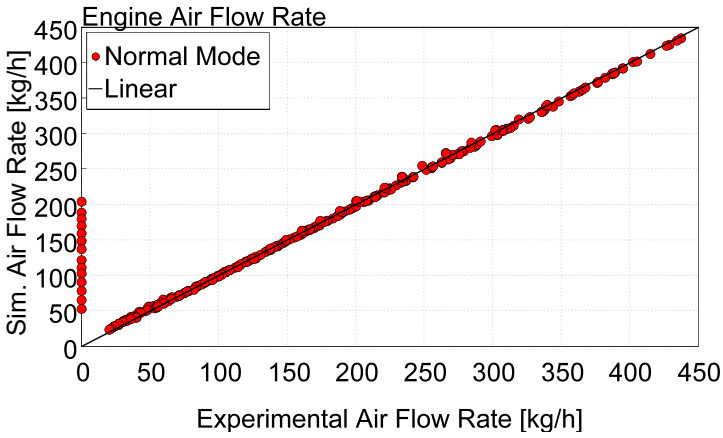


(b) Air Mass Flow Rate

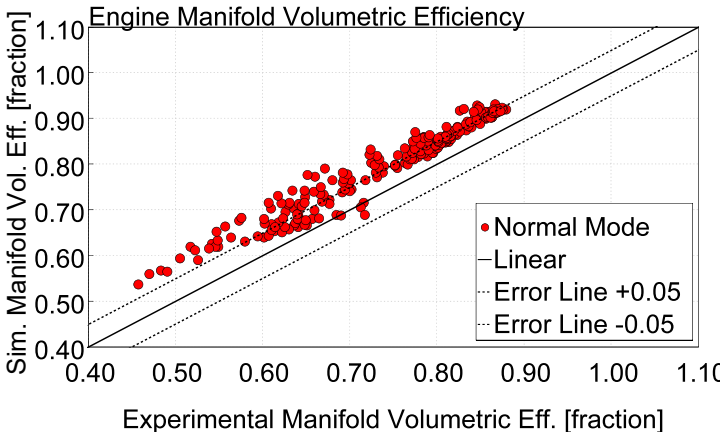


(c) Manifold Vol. Efficiency

Figure A.1: Brake Torque, Air Mass Flow Rate and Manifold Volumetric Efficiency - Normal Mode

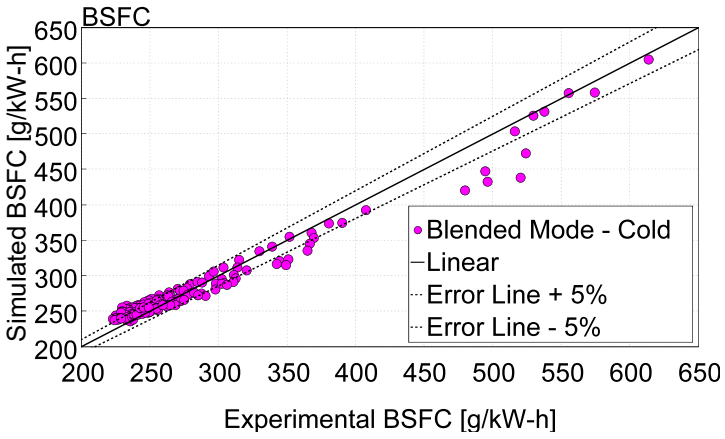


(a) Blended Mode - Cold

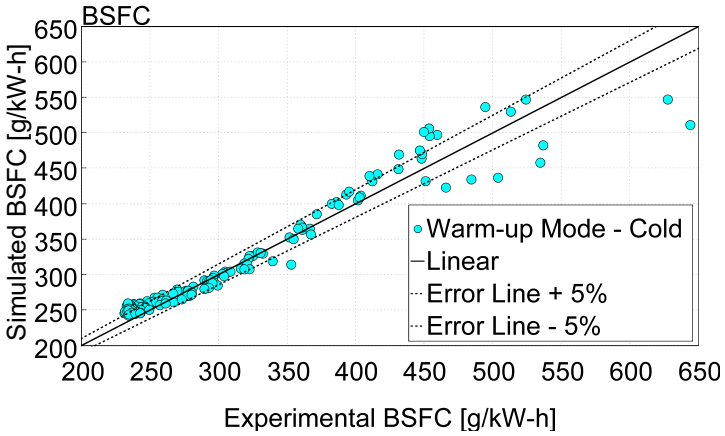


(b) Warm-up Mode - Cold

Figure A.2: Experimental and Simulated BSFC

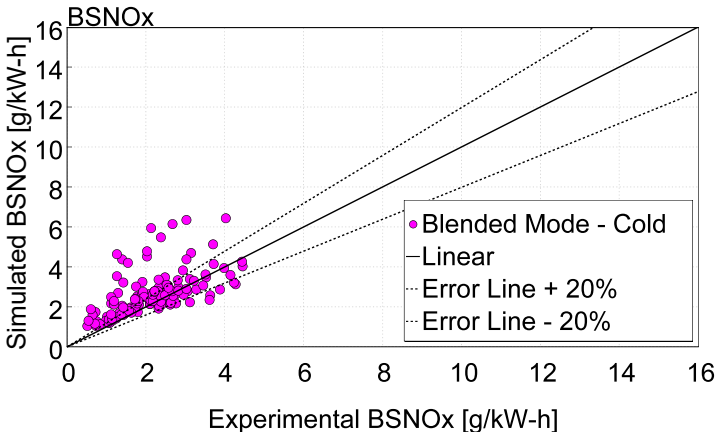


(a) Blended Mode - Cold

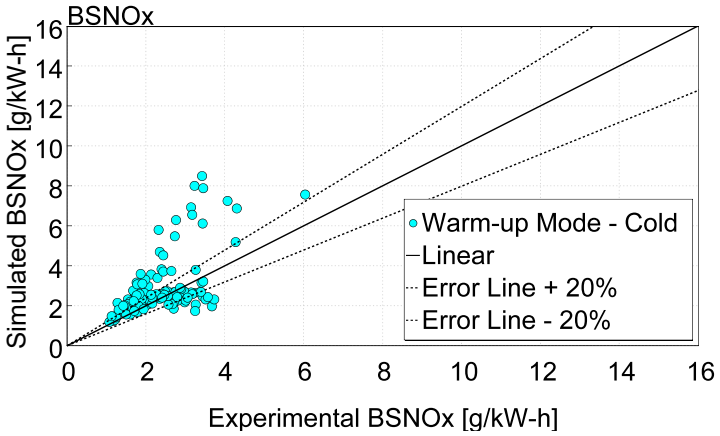


(b) Warm-up Mode - Cold

Figure A.3: Experimental and Simulated BSNOx

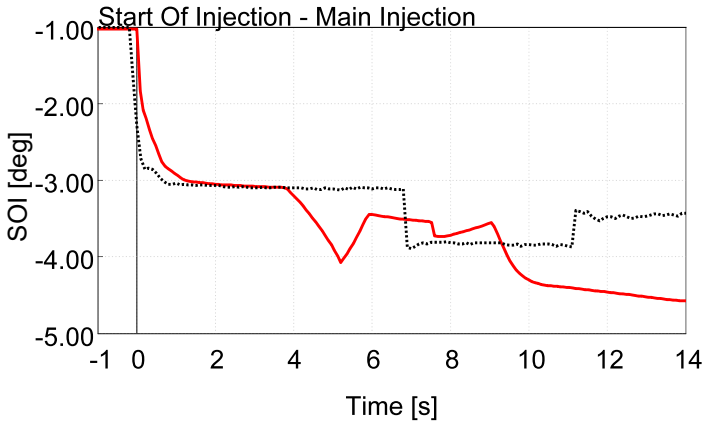


(a) Main Injection SOI

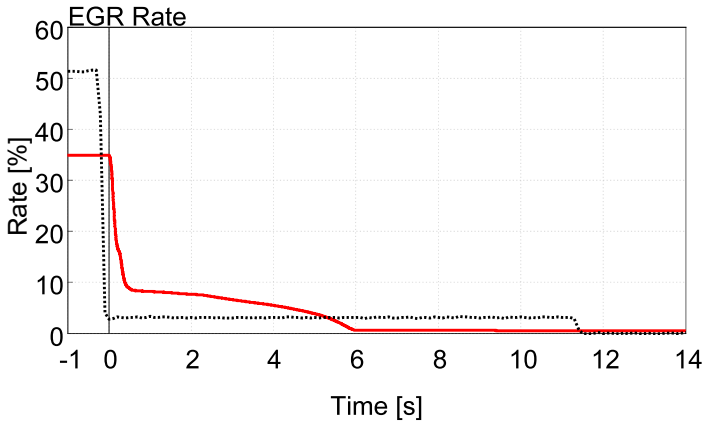


(b) EGR Rate

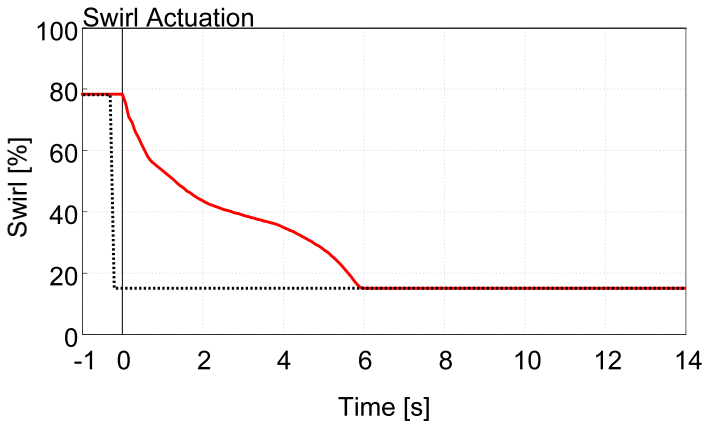


(c) Swirl Actuation

Figure A.4: Time to boost at 1500 rpm in Normal combustion mode - Engine parameters

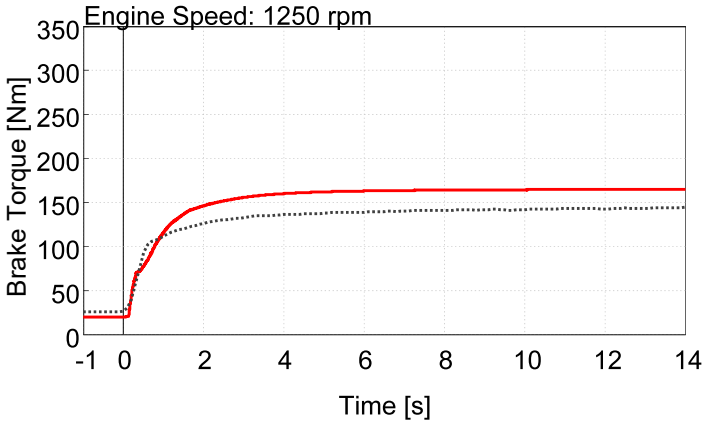


(a) 1250 rpm

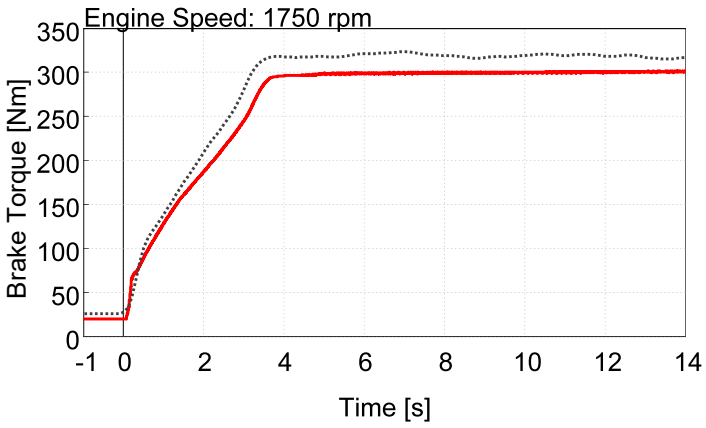


(b) 1750 rpm

Figure A.5: Time to boost at different engine speeds in Normal combustion mode - Torque

## Vehicle

In Fig.A.6, the model main powertrain subsystems (the engine, the electric network, the aftertreatment and the coolant circuit) are shown. Each subsystems is connected with the comprehensive model exchanging physical quantities.

In Fig.A.7, the vehicle speed during the last phase of the WLTC of Test A (see Fig.3.20 is reported with the upper and lower vehicle speed boundary required by WLTP regulation [37]. The vehicle speed remains between the minimum and maximum speed window along the cycle.

In order to better understand the deviation in terms of emissions along the driving cycle, in Fig.A.8 and A.9 the five most relevant energy weighted key-points for each of the three combustion mode are reported above the percentage difference between experimental and numerical results. The fact that the main key points of Warm-up and Blended mode lie in areas where the FRM model underestimates the fuel consumption, explains the slight underestimation (when the vehicle model follows the experimental speed, i.e. the experimental load) of the carbon dioxide emissions in the early stages of the driving cycle (before 600 s). In the Normal mode combustion, where the FRM engine overestimates up to 6 % the carbon dioxide emissions, the vehicle model regains the gap and achieves the same cumulated emissions of the experimental vehicle. As far as the nitrogen oxides are concerned, the most relevant key points of the Normal mode are located in a region where the difference between experimental and simulated is close to zero and this confirms the fact that the model well replicates the nitrogen oxides engine out emissions. In Tab.A.1, the five most relevant energy weighted key-points are reported.

Table A.1: First five key points along the WLTC driving cycle splitted by combustion mode and ordered in terms of energy impact in each combustion mode

| | **Normal Mode** | | | **Blended Mode** | | | **Warm-up Mode** | | |
|---|---|---|---|---|---|---|---|---|---|
| | rpm | Nm | % | rpm | Nm | % | rpm | Nm | % |
| 1 | 2250 | 152 | 5.2 | 1250 | 76 | 9.5 | 1750 | 51 | 4.8 |
| 2 | 2250 | 179 | 5.1 | 1250 | 64 | 5.7 | 1500 | 63 | 3.9 |
| 3 | 1750 | 102 | 4.6 | 1250 | 90 | 5.4 | 1250 | 64 | 3.5 |
| 4 | 2250 | 127 | 4.6 | 1750 | 153 | 5.2 | 1250 | 90 | 3.3 |
| 5 | 1500 | 127 | 3.7 | 1500 | 89 | 4.7 | 1750 | 63 | 3.3 |

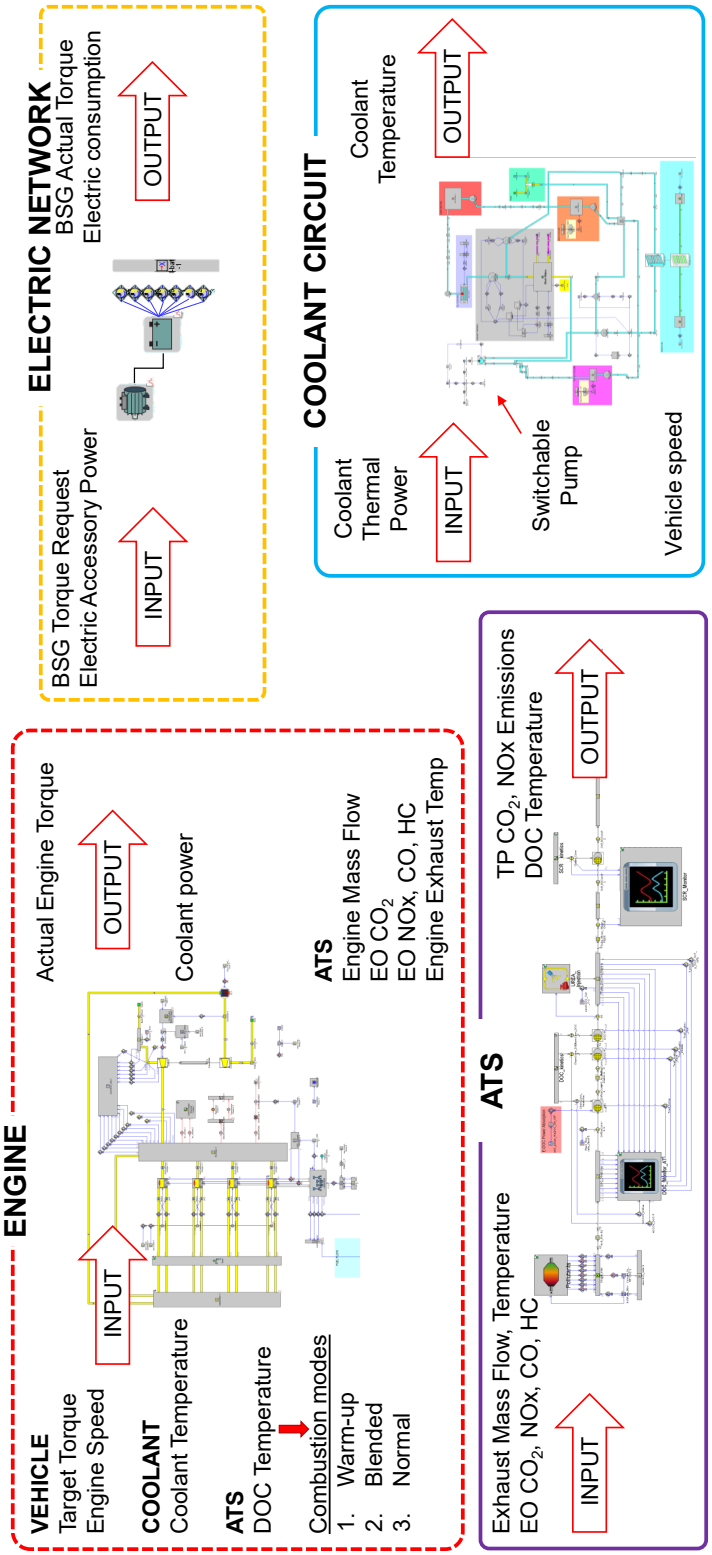


Figure A.6: Powetrain and vehicle integration: physical quantities and information flow

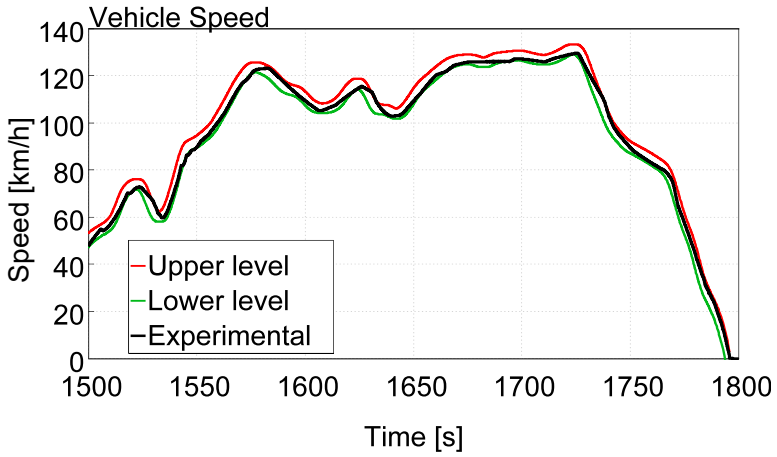


Figure A.7: Experimental speed compliance

# Results

## eSC Controller

The Rule Based controller for the activation and regulation of the electric Supercharger is reported in Fig.A.10. The eSC activates (and the bypass valve is closed) at engine speed below 3000 rpm and if the Demanded Boost Pressure (DBP) is higher than the Actual Boost Pressure (ABP) by 0.4 bar. When the DBP is close to the ABP the eSC switches off and the bypass valve opens.

## Vehicle Transient Performance

In Fig.A.11, vehicle speed, acceleration and eSC speed, along the elasticity manoeuvres from 80 to 120 km $h^{-1}$ in VI gear, are reported.

In Fig.A.12 and A.13 the transient manoeuvre from 80 to 120 km/h in sixth gear is shown. The activation of the eSC improves the engine brake torque that, in the vehicles featuring the eSC, achieves 300 Nm in less than 2 s thanks to the increase of the boost pressure. The improvement in terms of vehicle speed is clearer at the beginning of the transient: at around 8 s the acceleration of the different vehicle concepts is comparable. The BSG performance is bounded by the battery max available power on the vehicle featuring BSG and eSC, since the eSC power need has priority over the BSG power request.

In Fig.A.14 and A.15 the transient manoeuvre from 80 to 120 km/h in sixth gear is shown. In this manoeuvre the acceleration of the vehicles featuring the eSC or the BSG is similar. While the eSC contributes to the engine brake torque, exploiting the thermodynamic lever and with a lower electric energy expense, the BSG directly provides traction power to the crankshaft and the two vehicles performance are comparable.

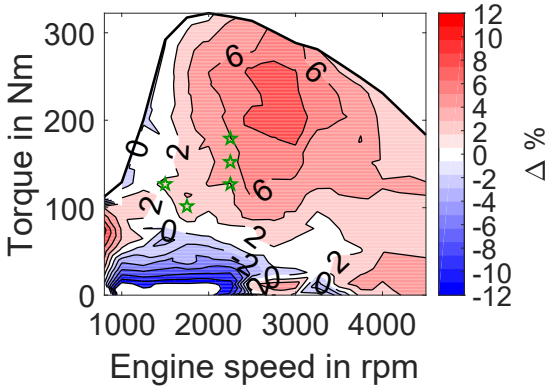


(a) Normal Mode

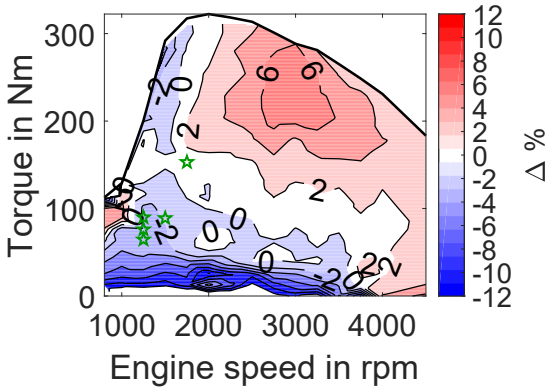


(b) Blended Mode

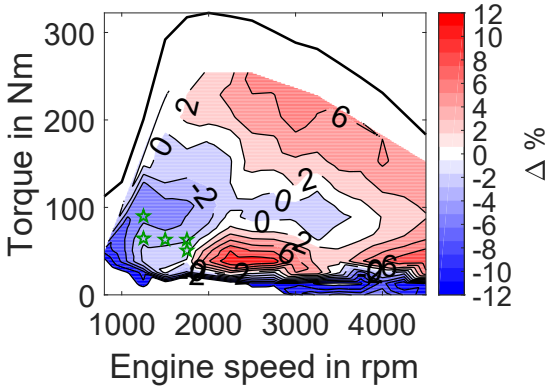


(c) Warm-up Mode

Figure A.8: BSFC numerical experimental percentage difference with WLTC key-points for each combustion mode (green star)

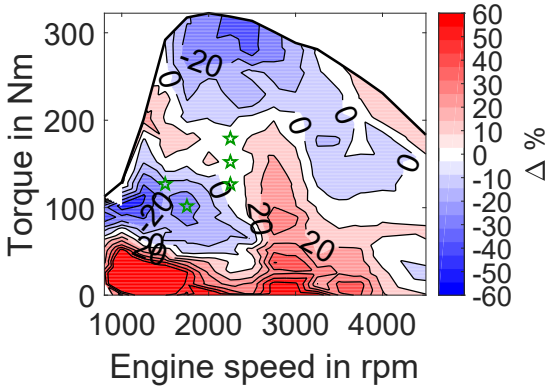


(a) Normal Mode

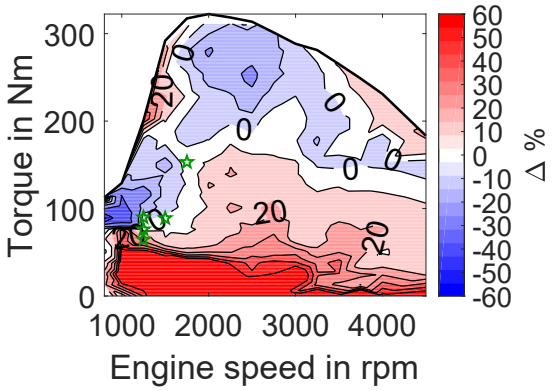


(b) Blended Mode

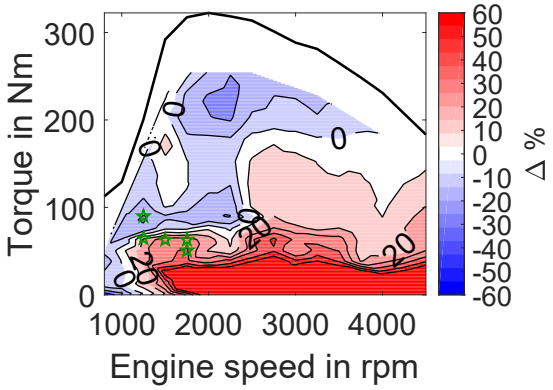


(c) Warm-up Mode

Figure A.9: BSNOx numerical experimental percentage difference with WLTC key-points for each combustion mode (green star)

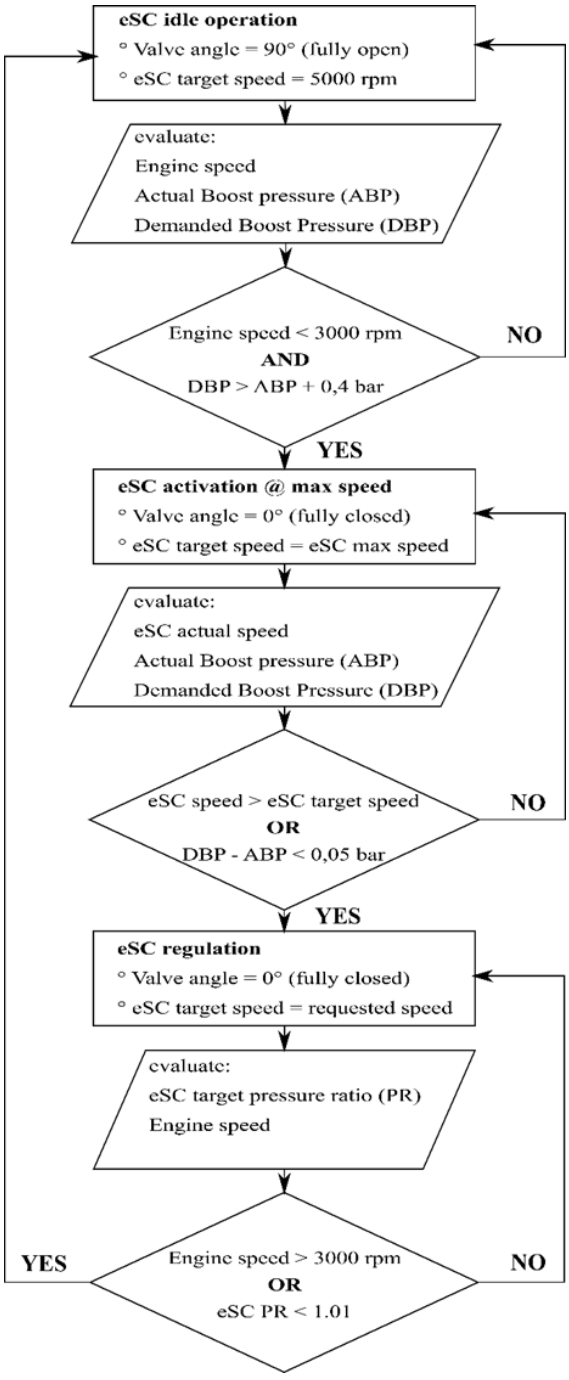


Figure A.10: eSC Rule Based Controller

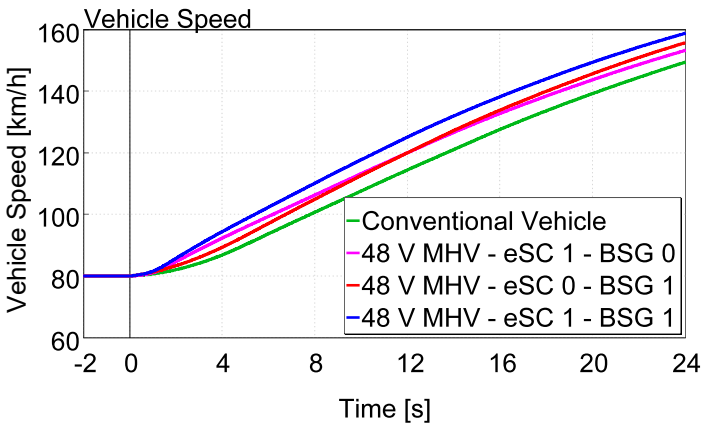


(a) Vehicle Speed

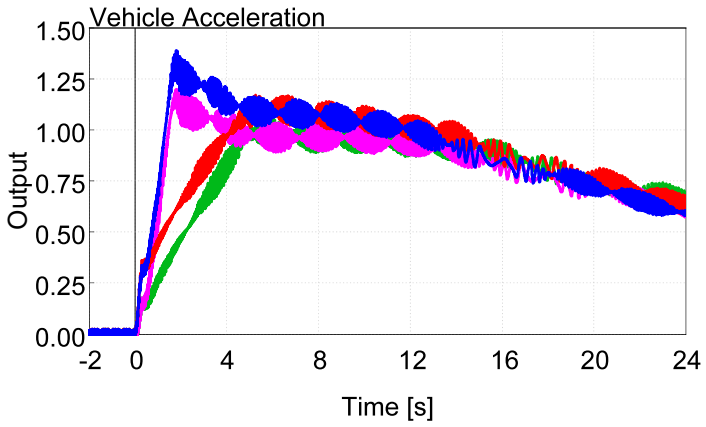


(b) Vehicle Acceleration

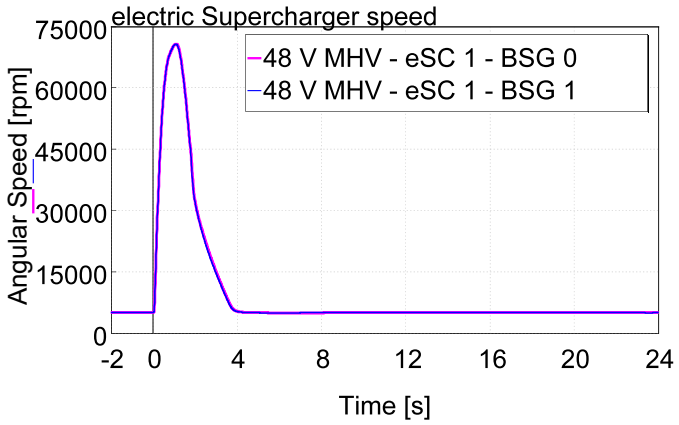


(c) eSC Speed

Figure A.11: Elasticity manoeuver 80-120 km/h in V gear - Vehicle speed and acceleration, eSC speed

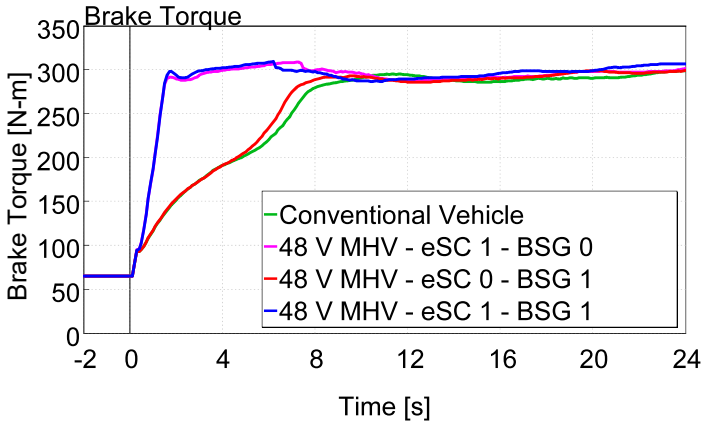


(a) Engine Brake torque

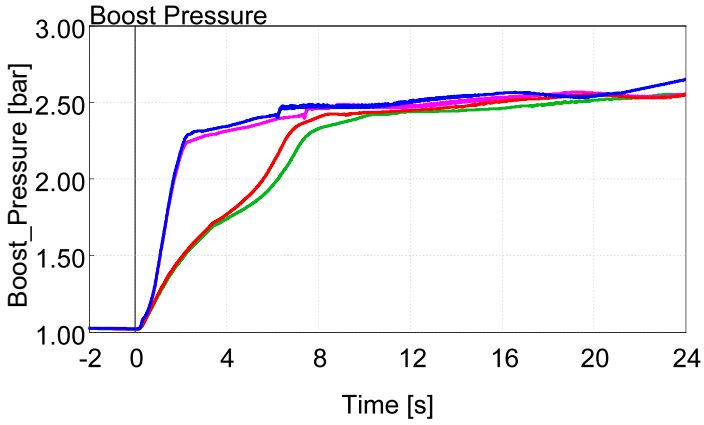


(b) Engine Boost pressure

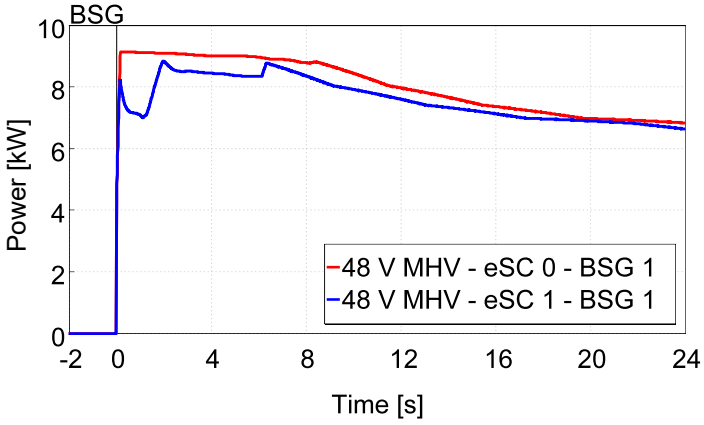


(c) BSG Mechanical Power

Figure A.12: Elasticity manoeuver 80-120 km/h in VI gear - Engine Brake Torque and Boost Pressure, BSG Mechanical Power

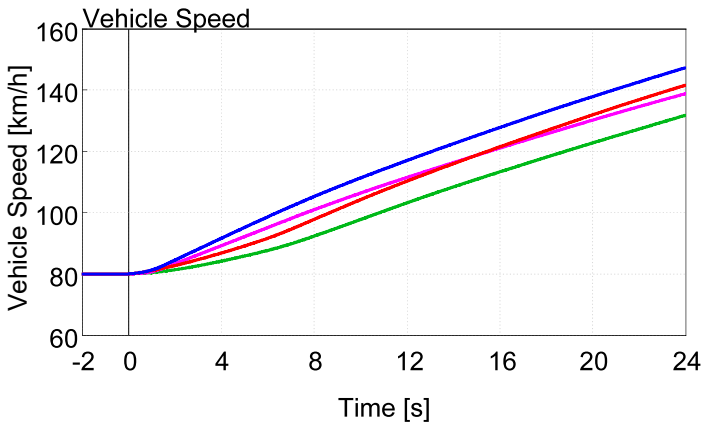


(a) Vehicle Speed

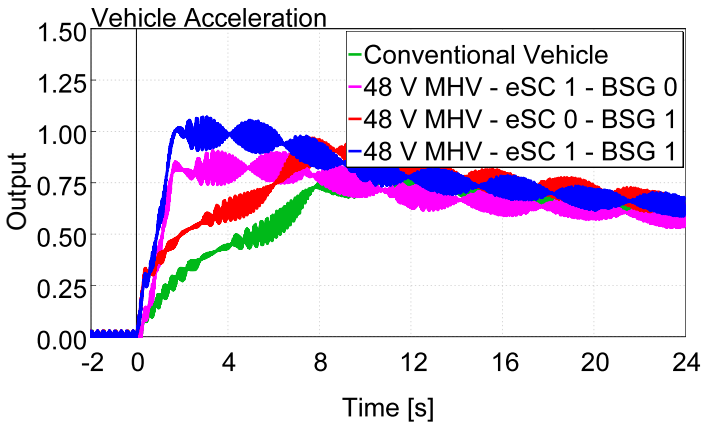


(b) Vehicle Acceleration

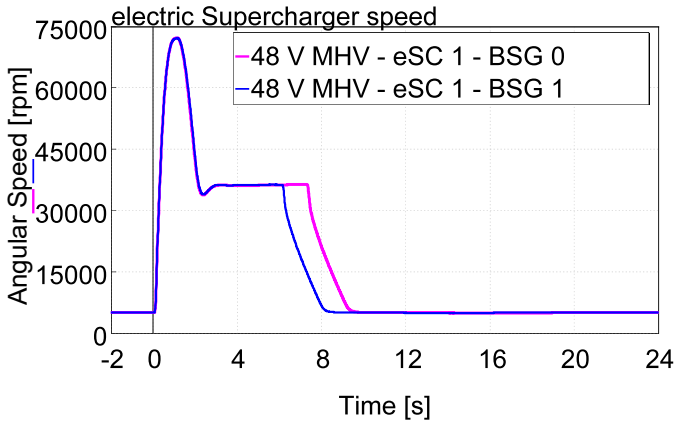


(c) eSC Speed

Figure A.13: Elasticity manoeuver 80-120 km/h in VI gear - Vehicle speed and acceleration, eSC speed

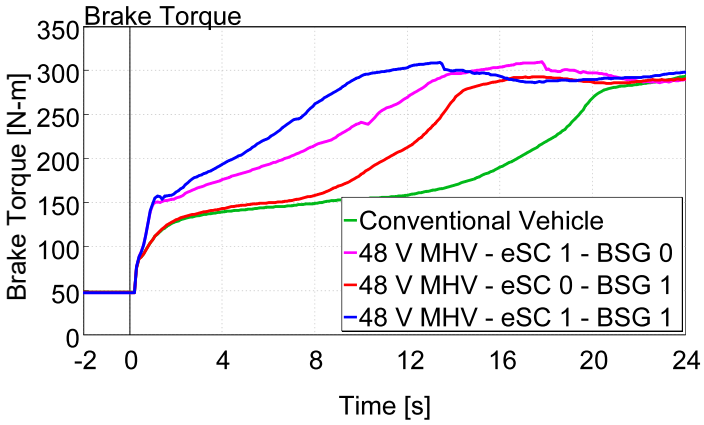


(a) Engine Brake torque

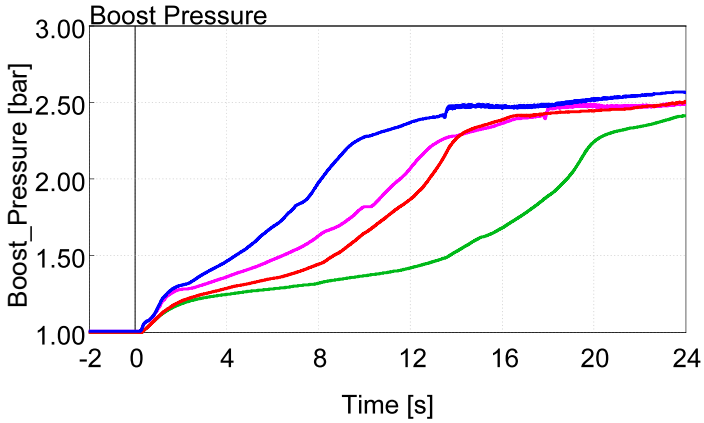


(b) Engine Boost pressure

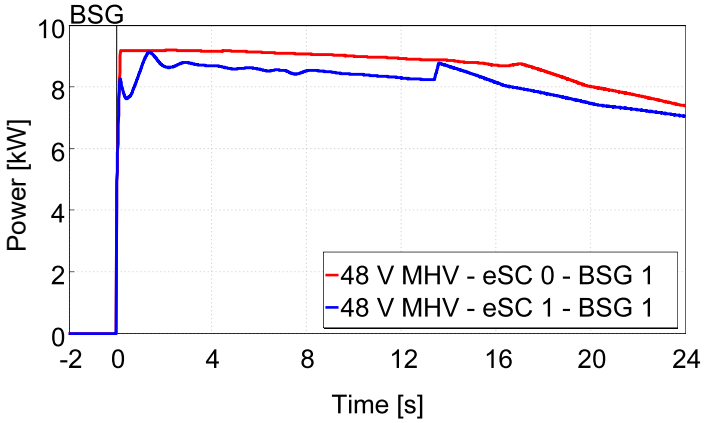


(c) BSG Mechanical Power

Figure A.14: Elasticity manoeuver 60-80 km/h in VI gear - Engine Brake Torque and Boost Pressure, BSG Mechanical Power

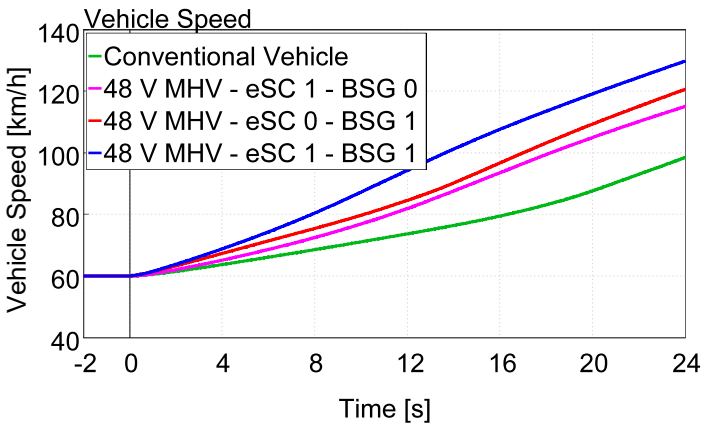


(a) Vehicle Speed

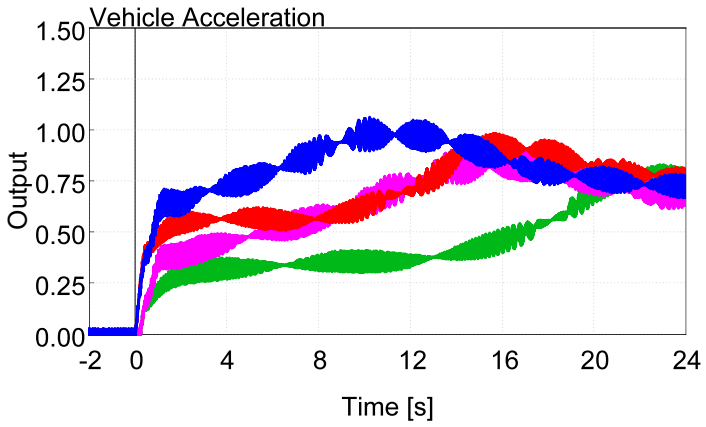


(b) Vehicle Acceleration

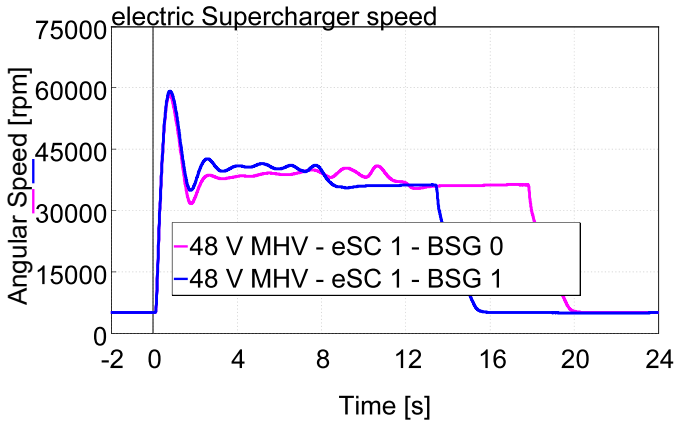


(c) eSC Speed

Figure A.15: Elasticity manoeuver 60-80 km/h in VI gear - Vehicle speed and acceleration, eSC speed

# Virtual Calibration

In Tab.A.2, the Key Points (KP) extracted from WLTC, RTS-95, FTP-75 and US06 and used for the virtual calibration of the engine are reported. The speeds of the Key Points ranges from an engine speed of 1250 to 2250 rpm and from a brake torque of 63 to 228 Nm, for the energy weighted KP, and just 25 and 38 Nm for the frequency weighted KP.

In Fig.A.16 the injection rate, the burn rate and the in-cylinder pressure of the most significant KP (i.e. 1500 rpm and 178 Nm) are reported for the Base engine, Case A with the Injection Rate Shaping and Case B with the engine featuring the theoretical injector without hydraulic delay. While the Base engine has two pilot injections and a main injection, Case A (i.e. the minimum BSFC calibration coming from the optimization of Case A), presents six injections (five pilot injections and a main injection). Although the injected quantity of the first three pilot injection is small, it contributes to the first rise of the burn rate before the Top Dead Center. The worsening in terms of efficiency due to the slightly delayed main injection with respect to the reference case is compensated by lower maximum in-cylinder pressure which contributes to lower friction. Case B shows the advantages of a zero hydraulic delay: the injection pattern is enclosed in 30 Crank Angle Degree (CAD) with six different injections, while the Base injection pattern lasted 37.5 CAD with only three injections. The advantage of a shorter overall injection duration is that the burn rate rises slowly at the beginning reducing the maximum in-cylinder pressure and especially the combustion noise.

Table A.2: Virtual calibration key points: ordered on the basis of the relative energy weight (first 17 points) and frequency (last 2 points)

| **Engine Speed [rpm]** | **Torque [Nm]** | **Relative weight** |
|---|---|---|
| 1500 | 178.0 | 3.4% |
| 1250 | 152.6 | 3.1% |
| 1750 | 102.3 | 2.3% |
| 2250 | 178.0 | 2.1% |
| 1250 | 180.2 | 2.1% |
| 1250 | 140.4 | 2.0% |
| 2250 | 152.2 | 1.9% |
| 2250 | 139.9 | 1.9% |
| 1500 | 202.6 | 1.8% |
| 1750 | 75.8 | 1.8% |
| 1500 | 139.5 | 1.8% |
| 1500 | 126.5 | 1.8% |
| 1250 | 63.6 | 1.6% |
| 1500 | 114.3 | 1.6% |
| 2250 | 228.4 | 1.6% |
| 2000 | 203.4 | 1.6% |
| 2000 | 178.2 | 1.6% |
| 1250 | 38.2 | 3.7% |
| 1250 | 24.9 | 3.4% |

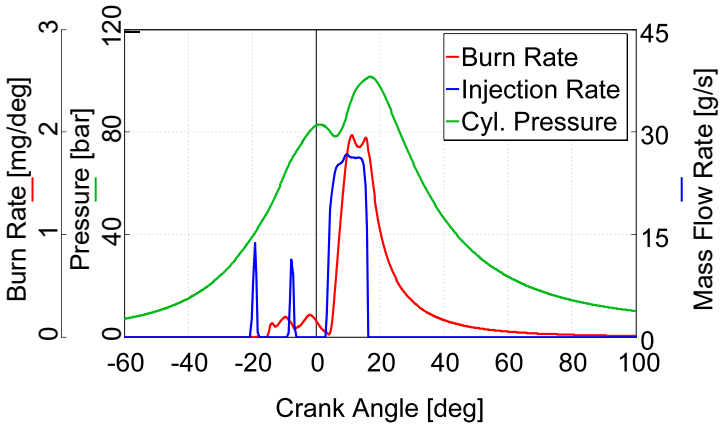


(a) Base

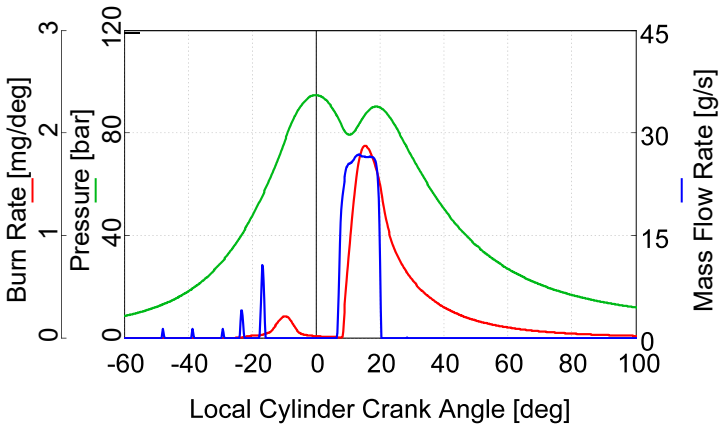


(b) Case A - IRS

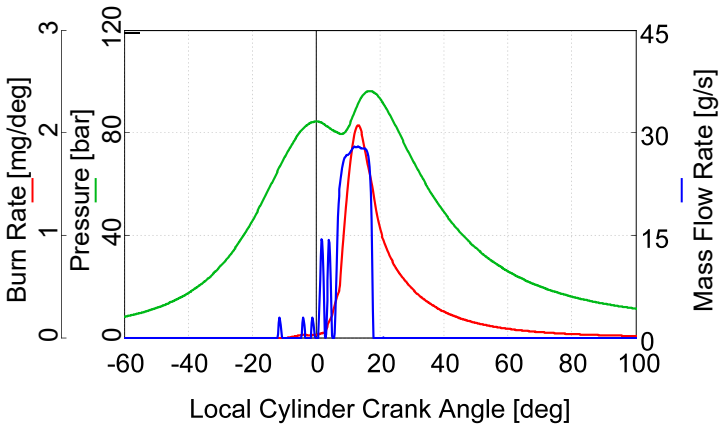


(c) Case B - Theoretical injector with zero hydraulic delay

Figure A.16: Injection Rate, Burn Rate and In-Cylinder Pressure - Operating point: 1500 rpm 179 Nm

# Nomenclature

### Roman Symbols

$\dot{m}_{amm}$ Ammonia mass flow rate

$\dot{m}_{exh}$ Exhaust gases mass flow rate

$\dot{m}_{fueleqv}$ Instantaneous equivalent fuel consumption

$\dot{m}_{fuelmax}$ Maximum fuel mass flow rate of the Normal combustion mode

$\dot{m}_{fuel}$ Instantaneous fuel flow rate

$\dot{m}_{NOxeqv}$ Equivalent nitrogen oxides mass flow rate

$\dot{m}_{NOxmax}$ Maximum nitrogen oxides mass flow rate of the Normal combustion mode

$\dot{m}_{NOx}$ Instantaneous nitrogen oxides flow rate

$\dot{m}_{rees}$ Battery power equivalent fuel consumption

$\rho$ Air density

$c_{pc}$ Ram air pressure coefficient

$EI$ Emission Index

$M_{amm}$ Ammonia molar mass

$M_{exh}$ Exhaust gas molar mass

$NEF$ NOx Flow Rate Equivalence factor

$P_{batt}$ Instantaneous battery power

$p_{SOC}$ Penalty function proportional term

$p_{static}$ Static pressure

$p_{total}$ Total pressure

$Q_{LHV}$ Fuel Lower Heating Value

$S$ Adapted Fuel Flow Rate Equivalence factor

$S_0$ Fuel Flow Rate Equivalence factor

$SOC(t)$ Istantaneous SOC

$SOC_{target}$ Target SOC

$W_{NOx}$ Weighting factor for the concurrent minimization of carbon dioxide and nitrogen oxides

F0 Road load constant term

F1 Road load linear term

F2 Road load quadratic term

R Vehicle resistance

V Vehicle speed

**Greek Symbols**

$\alpha_{amm}$ Ammonia dosing factor

**Acronyms / Abbreviations**

ABP Actual Boost Pressure

AFR Air to Fuel Ratio

BMEP Brake Mean Effective Pressure

BRE Burn Rate Error

BSFC Brake Specific Fuel Consumption

BSG Belt Starter Generator

BSNOx Brake Specific NOx Emissions

CAC Charge Air Cooler

CAD Crank Angle Degree

CAD Crank Angle Degree

CO Carbon Monoxide

CPOA Cylinder Pressure Only Analysis

DBP Demanded Boost Pressure

DMF Dual Mass Flywheel

DOC Diesel Oxidation Catalyst

DPF Diesel Particulate Filter

ECU Electronic Control Unit

EEMS Energy and Emission Management Strategy

EGR Exhaust Gas Recirculation

EHC Electrically Heated Catalyst

EMI Einspritzmengenindikator - injection quantity indicator

EMS Energy Management Strategy

EO Engine-Out

eSC electric Supercharger

ET Energizing Time

EVI Einspritzverlaufsindikator - injection rate indicator

FD Final Drive

FIS Fuel Injection System

FMEP Friction Mean Effective Pressure

FRM Fast Running Model

FTP-75 Federal Test Procedure

GA Genetic Algorithm

GM-GPS General Motors Global Propulsion System

HC Unburned Hydrocarbons

IRS Injection Rate Shaping

KP Key Points

LET Low End Torque

LIVC Late Intake Valve Closing

MFB50% 50% of Mass Fraction Burned

MGU Motor Generator Unit

MT Manual Transmission

NOx Nitrogen Oxides

OCV Open Circuit Voltage

OT Overtorque: recalibrated engine full load curve

PI Proportional Integrative

PM Particulate Matter

PWM Pulse-width modulation

RDE Real Driving Emissions

REES Rechargeable Energy Storage System

RTF Real Time Factor

RTS-95 Standardized Random Test For An AggressiveDriving Style

RTS-95 Standardized Random Test For An Aggressive Driving Style

SCR Selective Catalytic Reduction

SOC Start Of Injection

SOC State Of Charge

SWP Switchable Water Pump

T4 Temperature after the turbine

THC Total unburned Hydrocarbons

TMH Test Mass High

TML Test Mass Low

TO Tailpipe-Out

TTB Time To Boost

US06 Supplemental Federal Test Procedure US06

VGT Variable Geometry Turbine

WLTC Worldwide harmonized Light vehicles Test Cycle

WLTP Worldwide harmonized Light vehicles Test Procedure

# Bibliography


[1] *Volkswagen Light Duty Diesel Vehicle Violations for Model Years 2009-2016 | US EPA*. URL: https://www.epa.gov/vw (visited on 04/28/2020).

[2] *Audi A3 TDI is 2010 Green Car of the Year. Clean Diesel Reigns! | GreenCar.com*. URL: https://web.archive.org/web/20101124042249/http://www.greencar.com/articles/audi-a3-tdi-2010-green-car-year-clean-diesel-reigns.php (visited on 04/28/2020).

[3] *Audi 2010 Green Car Super Bowl Commercial - YouTube*. URL: https://www.youtube.com/watch?v=O%7B%5C_%7DMuqoSsuTQ (visited on 04/28/2020).

[4] *The death of diesel: has the one-time wonder fuel become the new asbestos? | Cities | The Guardian*. URL: https://www.theguardian.com/cities/2017/apr/13/death-of-diesel-wonder-fuel-new-asbestos (visited on 04/28/2020).

[5] *Volvo Cars to stop developing new diesel engines -CEO - Reuters*. URL: https://www.reuters.com/article/volvocars-diesel/volvo-cars-to-stop-developing-new-diesel-engines-ceo-idUSL8N1IJ1AI (visited on 04/28/2020).

[6] *Toyota To Halt Diesel Engine Development, C-HR Diesel Not Happening - autoevolution*. URL: https://www.autoevolution.com/news/toyota-to-halt-diesel-engine-development-c-hr-diesel-not-happening-121275.html (visited on 04/28/2020).

[7] *Nissan Stops Development Of Future Diesel Powerplants Globally - CarandBike*. URL: https://www.carandbike.com/news/nissan-stops-development-of-future-diesel-powerplants-globally-1862440 (visited on 04/28/2020).

[8] EU-Commission. "Commission Regulation (EU) 2017/1151". In: *Official Journal of the European Union* L175 (2017).

[9] *Touareg V8 TDI with extra-low NOx emissions tested by Emission Analytics: 75 per cent below Euro 6 limit | Volkswagen Newsroom*. URL: https://www.volkswagen-newsroom.com/en/press-releases/touareg-v8-tdi-with-extra-low-nox-emissions-tested-by-emission-analytics-75-per-cent-below-euro-6-limit-5941 (visited on 04/29/2020).

[10] *Emissioni: il confronto tra le Mercedes Classe A diesel, B turbobenzina e C plug-in hybrid - VIDEO*. URL: https://www.quattroruote.it/news/ecologia/2020/03/23/mercedes_confronto_test_emissioni_rde_diesel_a_200_d_b160_turbobenzina_c300_de_sw_ibrida_plug_in_a_gasolio.html (visited on 04/28/2020).

[11] P. Bielaczyc and J. Woodburn. "Trends in Automotive Emission Legislation: Impact on LD Engine Development, Fuels, Lubricants and Test Methods: a Global View, with a Focus on WLTP and RDE Regulations". In: *Emission Control Science and Technology* 5.1 (2019), pp. 86–98. DOI: 10.1007/s40825-019-0112-3.

[12] A. Joshi. "Review of Vehicle Engine Efficiency and Emissions". In: *SAE Technical Papers 2019-01-0314* (2019). DOI: 10.4271/2019-01-0314.

[13] *Paris clamps down on older diesel cars - France 24*. URL: https://www.france24.com/en/20190701-paris-clamps-down-older-diesel-cars (visited on 04/28/2020).

[14] *Rome to ban diesel cars from city centre by 2024 | Air pollution | The Guardian*. URL: https://www.theguardian.com/environment/2018/feb/28/rome-to-ban-diesel-cars-from-city-centre-by-2024-italy (visited on 04/28/2020).

[15] *Share of Diesel in New Passenger Cars | ACEA - European Automobile Manufacturers' Association*. URL: https://www.acea.be/statistics/tag/category/share-of-diesel-in-new-passenger-cars (visited on 04/28/2020).

[16] European Commission. "Commission Regulation (EU) 2019/631". In: *Official Journal of the European Union* L111 (2019). URL: https://eur-lex.europa.eu/legal-content/EN/TXT/?uri=CELEX%3A32019R0631.

[17] European Commission. "COMMISSION STAFF WORKING DOCUMENT IMPACT ASSESSMENT Accompanying the document Proposal for a Regulation of the European Parliament and of the Council setting emission performance standards for new passenger cars and for new light commercial vehicles as part of the Union's integrated approach to reduce CO2 emissions from light-duty vehicles and amending Regulation (EC) No 715/2007". In: (2017). URL: https://eur-lex.europa.eu/legal-content/EN/ALL/?uri=CELEX%3A52017SC0650.

[18] R. Bao, V. Avila, and J. Baxter. "Effect of 48 v Mild Hybrid System Layout on Powertrain System Efficiency and Its Potential of Fuel Economy Improvement". In: *SAE Technical Papers 2017-01-1175* (2017). DOI: 10.4271/2017-01-1175.

[19] *Hybrid vehicles: Trends in technology development and cost reduction | International Council on Clean Transportation*. URL: https://theicct.org/publications/hybrid-vehicles-trends-technology-development-and-cost-reduction (visited on 06/19/2020).

[20] R. Pothin and P. Dolcini. "Deployment of 48 V in Renault, current status and future outlook". In: *In: Liebl J., Beidl C. (eds) Internationaler Motorenkongress 2017. Proceedings*. Internationaler Motorenkongress 2017. Wiesbaden: Springer Vieweg, 2017.

[21] X. Mosquet, A. Arora, A. Xie, et al. *Who Will Drive Electric Cars to the Tipping Point? | BCG*. Tech. rep. Boston Consulting Group, 2020. URL: https://www.bcg.com/it-it/publications/2020/drive-electric-cars-to-the-tipping-point.aspx.

[22] A. Abdellahi, S. Khaleghi Rahimian, B. Blizanac, et al. "Exploring the Opportunity Space for High-Power Li-Ion Batteries in Next-Generation 48V Mild Hybrid Electric Vehicles". In: *SAE Technical Papers 2017-01-1197* (2017). DOI: 10.4271/2017-01-1197.

[23] G. Avolio, D. R. Brück, and D. J. Grimm. "Super Clean Electrified Diesel: Towards Real NOx Emissions below 35 mg/km". In: *27th Aachen Colloquium Automobile and Engine Technology* (2018).

[24] A. Zanelli, F. Millo, M. Barbolini, et al. "Assessment Through Numerical Simulation of the Impact of a 48 V Electric Supercharger on Performance and $CO_2$ Emissions of a Gasoline Passenger Car". In: *SAE Technical Papers 2019-01-1284* (2019). DOI: 10.4271/2019-01-1284.

[25] A. Zanelli, F. Millo, and M. Barbolini. "Driving Cycle and Elasticity Manoeuvres Simulation of a Small SUV Featuring an Electrically Boosted 1.0 L Gasoline Engine". In: *SAE Technical Paper 2019-24-0070* (2020). DOI: 10.4271/2019-24-0070.

[26] G. Di Pierro, F. Millo, M. Scassa, et al. "An Integrated Methodology for 0D Map-Based Powertrain Modelling Applied to a 48 v Mild-Hybrid Diesel Passenger Car". In: *SAE Technical Papers 2018-01-1659* (2018). DOI: 10.4271/2018-01-1659.

[27] E. Morra, E. Spessa, C. Ciaravino, et al. "Analysis of various operating strategies for a parallel-hybrid diesel powertrain with a belt alternator starter". In: *SAE Technical Papers 2012-01-1008* (2012). DOI: 10.4271/2012-01-1008.

[28] T. Nüesch, A. Cerofolini, G. Mancini, et al. "Equivalent Consumption Minimization Strategy for the Control of Real Driving NOx Emissions of a Diesel Hybrid Electric Vehicle". In: *Energies* 7 (2014), pp. 3148–3178. DOI: 10.3390/en7053148.

[29] J. M. Luján, A. García, J. Monsalve-Serrano, et al. "Effectiveness of hybrid powertrains to reduce the fuel consumption and NOx emissions of a Euro 6d-temp diesel engine under real-life driving conditions". In: *Energy Conversion and Management* 199 (2019). DOI: 10.1016/j.enconman.2019.111987.

[30] Z. Gao, J. C. Conklin, C. S. Daw, et al. "A proposed methodology for estimating transient engine-out temperature and emissions from steady-state maps". In: *International Journal of Engine Research* 11 (2010), pp. 137–151. DOI: 10.1243/14680874JER05609.

[31] F. Millo, G. Di Lorenzo, E. Servetto, et al. "Analysis of the Performance of a Turbocharged S.I. Engine under Transient Operating Conditions by means of Fast Running Models". In: *SAE International Journal of Engines* 6.2 (2013), pp. 968–978. DOI: 10.4271/2013-01-1115.

[32] M. Dorsch, J. Neumann, and C. Hasse. "Fully coupled control of a spark-ignited engine in driving cycle simulations". In: *Automotive and Engine Technology* 4.3-4 (2019), pp. 125–137. ISSN: 2365-5127. DOI: 10.1007/s41104-019-00050-0. URL: https://link.springer.com/article/10.1007/s41104-019-00050-0.

[33] P. Griefnow, J. Andert, F. Xia, et al. "Real-Time Modeling of a 48V P0 Mild Hybrid Vehicle with Electric Compressor for Model Predictive Control". In: *SAE Technical Papers 2019-01-0350* (2019). DOI: 10.4271/2019-01-0350.

[34] F. Millo, S. Caputo, C. Cubito, et al. "Numerical Simulation of the Warm-Up of a Passenger Car Diesel Engine Equipped with an Advanced Cooling System". In: *SAE Technical Papers 2016-01-0555* (2016). DOI: 10.4271/2016-01-0555.

[35] G. Liu, Z. Zhao, H. Guan, et al. "Benefit of Coolant Control Module for Thermal Management on SUV". In: *SAE Technical Papers 2017-01-0152* (2017). DOI: 10.4271/2017-01-0152.

[36] D. Karamitros, C. Avgerinos, S. Skarlis, et al. "Model-Based Comparison of Passive SCR Aftertreatment Systems for Electrified Diesel Applications". In: *SAE Technical Papers 2020-37-0023* (2020). DOI: 10.4271/2020-37-0023.

[37] UNECE. "Worldwide harmonized Light vehicles Test Procedure". In: *Global Technical Regulations No. 15 (Worldwide harmonized Light vehicles Test Procedure)* 15 (2014). URL: http://www.unece.org/fileadmin/DAM/trans/main/wp29/wp29r-1998agr-rules/ECE-TRANS-180a15e.pdf.

[38] Diesel Net. *Emission Test Cycles*. URL: https://www.dieselnet.com/standards/cycles/index.php (visited on 02/05/2020).

[39] Gamma Technologies LLC. *Engine Performance Application Manual*. 2018.

[40] F. Millo, G. Boccardo, A. Piano, et al. "Numerical Simulation of the Combustion Process of a High EGR, High Injection Pressure, Heavy Duty Diesel Engine". In: *SAE Technical Papers 2017-24-0009* (2017). DOI: 10.4271/2017-24-0009.

[41] J. B. Heywood. *Internal combustion engine fundamentals*. Vol. 1. McGraw-Hill Education, 1988. ISBN: 9781260116106.

[42] A. Piano. "Analysis of Advanced Air and Fuel Management Systems for Future Automotive Diesel Engine Generations". PhD thesis. Politecnico di Torino, 2018. DOI: 10.6092/polito/porto/2709586.

[43] Gamma Technologies LLC. *Acoustic Manual*. 2018.

[44] AVL. *Operative Instructions AVL 450 Combustion Noise Meter*. 1986.

[45] AVL. *Noise and Vibrations Training Program*. 1986.

[46] Gamma Technologies LLC. *Flow Theory Manual*. 2018.

[47] Gamma Technologies LLC. *Vehicle Driveline and HEV Application Manual*. 2018.

[48] *Urea Dosing Control*. URL: https://dieselnet.com/tech/cat_scr_diesel_control.php (visited on 04/29/2020).

[49] G. Randlshofer. "Integrated Diesel System Achieving Ultra-Low Urban and Motorway NOx Emissions on the Road". In: *Internationales Wiener Motorensymposium* (2019), pp. 198–217.

[50] F. Millo, L. Rolando, A. Zanelli, et al. "A Methodology for Modeling the Cat-Heating Transient Phase in a Turbocharged Direct Injection Spark Ignition Engine". In: *SAE Technical Papers 2017-24-0010* (2017). DOI: 10.4271/2017-24-0010.

[51] F. Maggio. "Numerical experimental investigation about vehicles fuel consumption and emissions over the NEDC driving cycle". (in italian). MA thesis. Politecnico di Torino.

[52] F. Atzler, M. Wegerer, F. Mehne, et al. "Fuel Consumption and Emissions Effects in Passenger Car Diesel Engines through the Use of a Belt Starter Generator". In: *SAE Technical Papers 2015-01-1162* (2015). DOI: 10.4271/2015-01-1162.

[53] A. Fotouhi, D. J. Auger, K. Propp, et al. "A review on electric vehicle battery modelling: From Lithium-ion toward Lithium–Sulphur". In: *Renewable and Sustainable Energy Reviews* 56 (2016), pp. 1008–1021. ISSN: 1364-0321. DOI: https://doi.org/10.1016/j.rser.2015.12.009.

[54] Y. Jun, B. C. Jeon, and W. Youn. "Equivalent Consumption Minimization Strategy for Mild Hybrid Electric Vehicles with a Belt Driven Motor". In: *SAE Technical Papers 2017-01-1177* (2017). DOI: 10.4271/2017-01-1177.

[55] S. Onori, L. Serrao, and G. Rizzoni. "Hybrid electric vehicles: Energy management strategies". In: *SpringerBriefs in Control, Automation and Robotics*. 9781447167792. Springer Publishing Company, 2016, pp. 1–112. DOI: 10.1007/978-1-4471-6781-5.

[56] F. Millo, C. V. Ferraro, and L. Rolando. "Analysis of Different Control Strategies for the Simultaneous Reduction of $CO_2$ and NOx Emissions of a Diesel Hybrid Passenger Car". In: *International Journal of Vehicle Design* 58.2-4 (2012), pp. 427–448. DOI: 10.1504/IJVD.2012.047393.

[57] F. Millo, F. Accurso, A. Zanelli, et al. "Numerical Investigation of 48 V Electrification Potential in terms of Fuel Economy and Vehicle Performance for a Lambda-1 Gasoline Passenger Car". In: *Energies* 12.2998 (2019). DOI: 10.3390/en12152998.

[58] G. Paganelli, T. M. Guerra, S. Delprat, et al. "Simulation and Assessment of Power Control Strategies for a Parallel Hybrid Car". In: *Proceedings of the Institution of Mechanical Engineers, Part D: Journal of Automobile Engineering* 214.7 (2000), pp. 705–717. DOI: 10.1243/0954407001527583.

[59] C. Musardo, B. Staccia, S. Midlam-Mohler, et al. "Supervisory control for NOx reduction of an HEV with a mixed-mode HCCI/CIDI engine". In: *Proceedings of the American Control Conference*. Vol. 6. 2005, pp. 3877–3881. DOI: 10.1109/acc.2005.1470579.

[60] H. Sagha, S. Farhangi, and B. Asaei. "Modeling and design of a NOx emission reduction strategy for lightweight hybrid electric vehicles". In: *IECON Proceedings (Industrial Electronics Conference)*. 2009, pp. 334–339. DOI: 10.1109/IECON.2009.5414944.

[61] U. Pfahl, A. Schatz, and R. Konieczny. "Advanced exhaust gas thermal management for lowest tailpipe emissions-combining low emission engine and electrically heated catalyst". In: *SAE Technical Papers 2012-01-1090* (2012). DOI: 10.4271/2012-01-1090.

[62] E. Pautasso, E. Servetto, D. Artukovic, et al. *Emissions and Fuel Consumption Trade-Offs of a Turbocharged Diesel Engine Equipped with Electrically Heated Catalyst*. SIA. 2012.

[63] R. Romanato, F. Acquaviva, F. Duma, et al. "48 v Hybrid System Technologies to Develop the Most Efficient and Cleanest Diesel". In: *SAE Technical Papers 2018-37-0011* 2018 (2018). DOI: 10.4271/2018-37-0011.

[64] J. Hofstetter, P. Boucharel, F. Atzler, et al. "Fuel Consumption and Emission Reduction for Hybrid Electric Vehicles with Electrically Heated Catalyst". In: *SAE Technical Papers 2020-37-0017* (2020). DOI: 10.4271/2020-37-0017.

[65] N. Lindenkamp, C. P. Stöber-Schmidt, and P. Eilts. "Strategies for reducing NOX- and particulate matter emissions in diesel hybrid electric vehicles". In: *SAE Technical Papers 2009-01-1305* (2009). DOI: 10.4271/2009-01-1305.

[66] M. Auerbach, M. Ruf, M. Bargende, et al. "Potentials of phlegmatization in diesel hybrid electric vehicles". In: *SAE Technical Papers 2011-37-0018* (2011). DOI: 10.4271/2011-37-0018.

[67] O. Maiwald, R. Brück, S. Rohrer, et al. "Optimised Diesel Combustion and SCR Exhaust Aftertreatment Combined with a 48 V System for Lowest Emissions and Fuel Consumption in RDE". In: *25th Aachen Colloquium Automobile and Engine Technology* (2016).

[68] S. Rothgang, M. Pachmann, S. Nigrin, et al. "The Electric Supercharger Challenge, Conception and Implementation". In: *MTZ worldwide* 76.9 (2015), pp. 4–9. DOI: 10.1007/s38313-015-0035-5.

[69] H. Breitbach, D. Metz, S. Weiske, et al. "Application, Design of the Electrically Driven Compressor". In: *Auto Tech Review* 5 (2016), pp. 38–42. DOI: 10.1365/s40112-016-1104-0.

[70] J. Schaub, C. Frenken, B. Holderbaum, et al. *FEV ECObrid - A 48V Mild Hybrid Concept for Passenger Car Diesel Engines*. Internationaler Motorenkongress. 2017. DOI: 10.1007/978-3-658-17109-4_15.

[71] Y. Liu, Y. Y. Wang, and M. Canova. "Distributed Model Predictive Control of an Electrically Boosted Diesel Engine Air Path System". In: *Proceedings of the American Control Conference* (2018). DOI: 10.23919/ACC.2018.8431413.

[72] R. Coltro. "Experimental Analysis of the Influence of the Propulsion System Characteristics on the Vehicle Manoeuvres Defining Performances and Drivability". in italian. MA thesis. Politecnico di Torino, 2005.

[73] T. Schnorbus, J. Schaub, M. Miccio, et al. *Mild Hybridisation and Electric Boosting Improving Diesel Emissions and Fuel Efficiency with Premium Performance*. $24^{th}$ Aachen Colloquium. 2015.

[74] *FEV HECS ECObrid with 48V hybridization - FEV*. URL: http://magazine.fev.com/en/fev-hecs-ecobrid-with-48v-hybridization/ (visited on 04/30/2020).

[75] P. Arya. "Development of Automated Calibration Methodology for Last Generation of Diesel Automotive Powertrains". PhD thesis. Politecnico di Torino, 2019.

[76] A. Piano, F. Millo, F. Sapio, et al. "Multi-Objective Optimization of Fuel Injection Pattern for a Light-Duty Diesel Engine through Numerical Simulation". In: *SAE International Journal of Engines* 11.6 (2018), pp. 1093–1107. DOI: 10.4271/2018-01-1124.

[77] F. Accurso, A. Zanelli, L. Rolando, et al. “Real Time Energy Management Control Strategies for an Electrically Supercharged Gasoline Hybrid Vehicle”. In: *SAE Technical Paper 2020-01-1009* (2020). DOI: 10.4271/2020-01-1009.

This Ph.D. thesis has been typeset by means of the TEX-system facilities. The typesetting engine was LuaLATEX. The document class was `toptesi`, by Claudio Beccari, with option `tipotesi=scudo`. This class is available in every up-to-date and complete TEX-system installation.